Universidade de São Paulo

Instituto de Física e Química de São Carlos

Departamento de Física e Ciência dos Materiais

GRADIÔMETROS SUPERCONDUTORES ACOPLADOS A SQUIDs E SUA APLICAÇÃO EM BIOMAGNETISMO

Antonio Carlos Oliveira Bruno

Tese apresentada ao Instituto de Física e Química de São Carlos da Universidade de São Paulo para obtenção do título de Doutor em Ciências - "Física Aplicada"

Orientador: Paulo Edmundo de Leers Costa Ribeiro

[redacted]

SERVIÇO DE BIBLIOTECA E INFORMAÇÃO - IFQSC
FÍSICA

UNIVERSIDADE DE SÃO PAULO

INSTITUTO DE FÍSICA E QUÍMICA DE SÃO CARLOS

MEMBROS DA COMISSAO JULGADORA DA TESE DE DOUTORADO DE ANTONIO CARLOS OLIVEIRA BRUNO APRESENTADA AO INSTITUTO DE FISICA E QUIMICA DE SAO CARLOS, DA UNIVERSIDADE DE SAO PAULO, EM 13 DE SETEMBRO DE 1990.

COMISSAO JULGADORA:

Prof.Dr.Paulo E.de L.Costa Ribeiro

Prof.Dr.Horacio Carlos Panepucci

Prof.Dr.Otaciro Rangel Nascimento

Prof.Dr.Lincoln de A.Moura Junior

Prof.Dr.Robert Lee Zimmerman

Cx. Postal, 369 - FONE (0162) 71-1016 - CEP 13.560 - São Carlos - SP - Telex 162374 - FQSC - BR - BRASIL

Aos meus pais.

AGRADECIMENTOS

Gostaria de agradecer em primeiro lugar ao Prof. Sergio Mascarenhas que desde a minha infância me estimulou e me incentivou com seu exemplo, a adentrar nas lides científicas. Como ele gosta de dizer, eu acabei tentando conjugar o verbo *ser*. Também foi ele que em meados de 1979 me apresentou ao Prof. Paulo Costa Ribeiro que me orientou neste trabalho.

Ao Paulo meu orientador e amigo, agradeço por estes mais de dez anos de convívio com um otimismo diário, com a crítica sempre construtiva e por ter acreditado em mim e neste projeto.

Desejo agradecer também a Profa. Yvonne Mascarenhas e ao Prof. Jan Slaets por todo empenho, interesse e hospitalidade sem o que esta tese não teria se concretizado.

A todos que contribuiram com idéias, sugestões e me ajudaram nas experiências, vão os meus agradecimentos: Prof. Bruno Maffeo, Eng. Iradj R. Eghrari, Prof. Jean Piere von der Weid, Dr. Carley C. Paulsen, Enga. Adriana V. Guida, Sergei D. Soarez e Clarissa Dolce da Silva. Agradecimentos especiais vão também para Don Antonio P. Picon e Edson (Cidadão) Joaquim da oficina mecânica do Departamento de Física da PUC-Rio.

Desejo também agradecer ao Prof. Orest G. Symko que sempre me incentivou e encorajou a transformar estas publicações em uma tese e especialmente ao Dr. James E. Zimmerman que me ensinou que a arte de fazer SQUIDs pode ser uma coisa simples e divertida.

Agradecimentos são devidos também a todos que especificamente contribuiram para tornar possível o meu estágio de pré-doutoramento na Italia, Prof. Sergio Mascarenhas, Prof. Paulo Costa Ribeiro, Prof. Sergio Costa Ribeiro, Sonia Nolesco e Prof. Carlos Alberto Aragão de Carvalho.

Um agradecimento especial vai também para todo o pessoal do Istituto di Elettronica dello Stato Solido - Consiglio Nazionale delle Ricerche (CNR), Roma, Italia, pela hospitalidade durante o ano que passei lá, aonde foram realizados os testes com os gradiômetros planares e a maior parte desta tese foi escrita; Prof. Gian Luca Romani, Dr. Guido Torrioli, Dr. Vittorio Pizzella, Dr. Roberto Leoni, Dr. Sandro Barbanera, Dr. Carlo Salustri, Prof. Ivo Modena e Prof. Pasqualino Carelli que gentilmente permitiu que eu usasse o seu HP-VECTRA aonde eu pude me iniciar nos mistérios do TEX *typesetting system* no qual esta tese foi escrita.

Finalmente desejo agradecer demais a minha esposa Cristiana e ao meu filho Eduardo pelo constante apoio, companheirismo e paciência durante todos estes anos.

Rio de Janeiro, 9 de julho de 1990.

SERVIÇO DE BIBLIOTECA E INFORMAÇÃO - IFQSC
FÍSICA

SUMÁRIO

PREFÁCIO 1

1 INTRODUÇÃO 3

1.1 - Biomagnetismo 3
1.2 - Campos Biomagnéticos e Ruído Ambiental 4
1.3 - SQUIDs e Discriminação Espacial 5

2 GRADIÔMETROS AXIAIS 8

2.1 - Caracterização Usando a Expanção de Taylor 8
2.2 - Aspectos Práticos na Construção de Gradiômetros 13
2.3 - Testes de Performance e Calibração 15

3 FILTROS ESPACIAIS 19

3.1 - Caracterização Usando a Transformada de Fourier 19
3.2 - Projeto de Filtros Espaciais 23
3.3 - Medida da Função de Transferência 25
3.4 - Calibração 28

4 GRADIÔMETROS PLANARES 31

4.1 - O Gradiômetro Planar como um Filtro Espacial 31
4.2 - Projeto de *Arrays* 32
4.3 - Recuperação do Sinal de Entrada 36

5 DISCUSSÃO 38

5.1 - Perspectivas 38
5.1 - Conclusão 39

6 PUBLICAÇÕES 40

6.1 - Lista de Publicações 40
6.2 - Resumo das Publicações 41

REFERÊNCIAS 44

ANEXOS 51

PREFÁCIO

A detecção de campos biomagnéticos está relacionada, à possibilidade de medida de um campo magnético muito fraco imerso em um ambiente magneticamente ruidoso. Uma das fontes responsáveis pela presença de campos magnéticos no corpo humano, são os deslocamentos iônicos dentro e fora da membrana de células excitáveis. O ruído magnético provém de varias fontes, como por exemplo, o campo magnético terrestre, com um valor aproximadamente um milhão de vezes mais intenso que o mais intenso dos campos biomagnéticos, o campo magnético cardíaco.

O único dispositivo com sensibilidade apropriada para detecção de campos biomagnéticos é o SQUID (Superconducting QUantum Interference Device). Devido a sua sensibilidade e característica, o SQUID é utilizado em conjunto com um transformador de fluxo de geometria gradiométrica, que é capaz de discriminar espacialmente fontes distantes (ruído) em favor de fontes próximas ao sensor (sinal biomagnético).

O objetivo principal deste trabalho, foi o estudo da discriminação espacial realizada através da utilização de gradiômetros, na detecção de campos biomagnéticos. Esta tese é o produto de um trabalho de pesquisa, que resultou em 12 publicações, que apresentam e discutem uma nova abordagem para a compreensão da atuação dos gradiômetros sobre os sinais detectados. Além disso, esta nova abordagem gerou outras técnicas relevantes para a área, como a calibração do sistema com uma precisão até então não alcançada, a possibilidade de recuperação do sinal original detectado e um procedimento para auxiliar o projeto de *arrays* de gradiômetros planares.

Esta tese foi escrita de tal forma que todas as técnicas desenvolvidas, resultados e as principais conclusões estão contidas em seu corpo. Portanto, não é necessária a leitura das publicações, a não ser que um maior aprofundamento em alguns dos assuntos abordados seja desejado. As contribuições específicas dadas por esta tese serão referenciadas sob forma de anexos. Na introdução, aspectos gerais de biomagnetismo são discutidos, como também o seu desenvolvimento a partir da invenção do SQUID. No capítulo 2, estão descritos o modelo convencional, a construção, a medida de performance, a calibração e aspectos práticos no projeto de um gradiômetro axial. Detalhes adicionais podem ser encontrados na

publicação [1]. No capítulo 3, um novo modelo para gradiômetros é introduzido baseado em conceitos de filtragem digital e o procedimento da calibração do sistema é rediscutido. Detalhes adicionais podem ser encontrados nas publicações [2], [3], [4], [5], [10] e [12]. No capítulo 4, este modelo é estendido para gradiômetros planares e é desenvolvido um algorítmo de desconvolução para recuperação do sinal originalmente medido. Este procedimento também pode ser aplicado no auxilio do projeto de *arrays*. Também neste capítulo é discutida a viabilidade da utilização destes novos gradiômetros. Nas publicações [6], [7], [8], [9] e [11] detalhes adicionais podem ser encontrados. No capítulo 5, perspectivas e a conclusão, e finalmente no capítulo 6 a lista e o resumo das publicações.

1 INTRODUÇÃO

1.1 - Biomagnetismo

O conceito de que campos magnéticos estão associados a atividade bioelétrica do corpo humano, embora previsíveis com base em simples considerações de eletromagnetismo, só obtiveram uma verificação experimental em 1963 quando Baule e McFee [1] mediram pela primeira vez sinais magnéticos associados com a atividade cardíaca. Do ponto de vista instrumental, o equipamento utilizado era muito primitivo, mesmo assim pode ser demonstrado que medidas de campos magnéticos um milhão de vezes menores que o campo magnético terrestre são possíveis em ambientes não blindados magneticamente.

Um progresso fundamental na detecção de campos biomagnéticos foi alcançado somente sete anos depois. Em 1970 Cohen, Edelsack e Zimmerman [2] usando um dispositivo supercondutor, mediram um magnetocardiograma dentro de uma câmara magneticamente blindada no MIT [3]. O circuito criogênico consistia de uma bobina supercondutora acoplada a um Superconducting QUantum Interference Device [4- 5]. O SQUID é atualmente o sensor mais sensível de fluxo magnético, consequentemente de campo magnético, e um dos dispositivos de medida mais sensíveis de qualquer quantidade física [6]. As medidas realizadas no MIT demonstraram que sinais magnéticos de alta qualidade podiam ser medidos simultaneamente com sinais elétricos, abrindo assim caminho para pesquisa sistemática de campos biomagnéticos, incluindo a detecção de campos magnéticos associados com a atividade cerebral [7].

Um outro importante passo do ponto de vista tecnológico foi dado quando pela primeira vez Zimmerman e Frederick [8], utilizaram uma bobina em configuração gradiométrica junto com o SQUID, para detecção de um magnetocardiograma fora da camara blindada. Mais adiante, Opfer e colaboradores [9] utilizando o mesmo princípio mediram sinais magnéticos cerebrais em um ambiente urbano. A demonstração de que um sistema muito mais viável, do que o utilizado por Baule e MacFee, poderia ser utilizado para se detectar campos magnéticos em volta do corpo humano, deu um grande impulso a esta investigação e um maior número de grupos de pesquisa envolveu-se neste campo durante a segunda metade dos anos setenta [10- 18].

SERVIÇO DE BIBLIOTECA E INFORMAÇÃO - IFQSC
FÍSICA

Simples analises teóricas sugeriam que a abordagem magnética era em princípio mais poderosa na identificação de fontes de atividade bioelétrica [19- 21], também mais instrumentos eram desenvolvidos permitindo sua operação até mesmo em ambientes clínicos [22- 25]. Resultados importantes foram obtidos na pesquisa de fisiologia cardíaca [26- 31] e cerebral [32- 37] e na validação clínica do método [38- 44]. A mais importante vantagem do método biomagnético é a possibilidade de localização em três dimensões, de fontes de atividades fisiológicas e patológicas com uma incerteza de possivelmente poucos milímetros. É a chamada localização funcional em oposição a localização anatômica ou metabólica fornecida por outros instrumentos de diagnóstico.

Os últimos anos proporcionaram mais progressos em investigação clínica [45- 48] e também em pesquisa básica [49- 54]. Contudo, os maiores avanços foram em relação a instrumentação, onde novas tecnologias levaram a uma geração de SQUIDs microfabricados, com performances excepcionais e perfeitamante apropriados para integração em sistemas multicanais. Desde a segunda metade dos anos oitenta, varios sistemas com 4, 5 e 7 canais [55- 58] foram introduzidos e mais recentemente, sistemas com 24, 30 e 37 canais foram construídos [59- 61] sendo que estes dois ultimos estão disponíveis comercialmente.

1.2 - Campos Biomagnéticos e Ruído Ambiental

A medida de campos biomagnéticos está relacionada a possibilidade de medida de um campo magnético extremamente fraco imerso em um ambiente magneticamente ruidoso. Várias fontes são responsaveis pela presença de campos magnéticos no corpo humano. Por exemplo, deslocamentos iônicos através da membrana de células excitáveis produzem correntes iônicas, que por sua vez geram ambos potenciais elétricos e campos magnéticos na superficie do corpo. O conteúdo espectral destes campos se encontra dentro de uma faixa de poucas centenas de Hertz. Algumas vêzes a medida precisa ser estendida a uma frequência muito baixa, chegando mesmo até DC no caso de alguns estudos no coração e no cérebro. Existem diferencas significativas na amplitude dos varios tipos de campos biomagnéticos pesquisados, como pode ser visto na Tabela 1.1. Deve ser enfatizado que o limite inferior da tabela é função somente da sensibilidade da instrumentação utilizada até hoje. Está claro que o fator limitante da sensibilidade do sistema supercondutor de medida, não está posto no SQUID, mas na capacidade de rejeição do ruído magnético ambiental existente onde as medidas são

realizadas. Em primeiro lugar, temos o campo magnético terrestre com uma amplitude de 50 μTesla. Este valor é 9 ordens de magnitude maior que o mais fraco dos campos biomagnéticos. Portanto, vibrações do sensor no campo terrestre, produzem grandes perturbações na medida. Em segundo, as micropulsações de campos geomagnéticos: os chamados campos magnetotelúricos, põem uma dependencia da forma $1/f$ na amplitude do ruído impondo sérios problemas na parte de baixa frequência no espectro da medida. Em último, os campos magnéticos associados com a presença de grandes massas metálicas, hélices, bombas, elevadores, etc., geralmente existentes na proximidade do local de realização das medidas. A amplitude deste último, chamado de ruído magnético urbano, está na faixa de 0.1 a 10 μTesla.

TABELA 1.1

CAMPOS BIOELÉTRICOS	μV	CAMPOS BIOMAGNÉTICOS	pT	BANDA Hz
Eletrocardiograma	1000	Magnetocardiograma	50	0.05 – 100
Eletrocard. Fetal	5 – 50	Magnetocard. Fetal	1 – 10	0.05 – 100
Eletroencefalograma	50	Magnetoencefalograma	1	0.5 – 30
Potenciais Evocados	10	Campos Evocados	0.1	DC – 50
Eletromiograma	1000	Magnetomiograma	10	DC – 2000
Eletro-oculograma	1000	Magneto-oculograma	10	DC

Tabela 1.1 - Intensidade de campos bioelétricos e biomagnéticos.

1.3 - SQUIDs e Discriminação Espacial

O detector de campo magnético mais simples é uma bobina. Um campo magnético variante no tempo passando através da bobina gera uma corrente que pode ser detectada e amplificada (Lei de Faraday). A limitação da utilização da bobina de indução é o ruído associado à resistência da própria bobina. Uma analise simples pode mostrar que o campo mínimo detectavel é inversamente proporcional a frequência do sinal [62]. Como em biomagnetismo o interesse está em medidas em baixa frequência (0-100 Hz), a aplicação de bobinas de indução à temperatura ambiente é limitada. A utilização de magnetômetros *fluxgate* ou de magnetômetros

baseados no efeito Hall também tem sua aplicação limitada devido a sua baixa sensibilidade para esta faixa de frequência.

A relativa baixa sensibilidade em baixas frequências dos magnetômetros convencionais, pode então ser melhorada através de utilização de circuitos supercondutores. A bobina de detecção neste caso fica intrinsecamente livre de ruído e um Superconducting QUantum Interference Device (SQUID) [63- 64] pode ser usado como amplificador. Este dispositivo é uma aplicação do efeito Josephson [65- 66] e requer a utilização de técnicas criogênicas. O possível aumento de problemas técnicos dada a utilização de hélio líquido, é largamente justificado pelo ganho de sensibilidade.

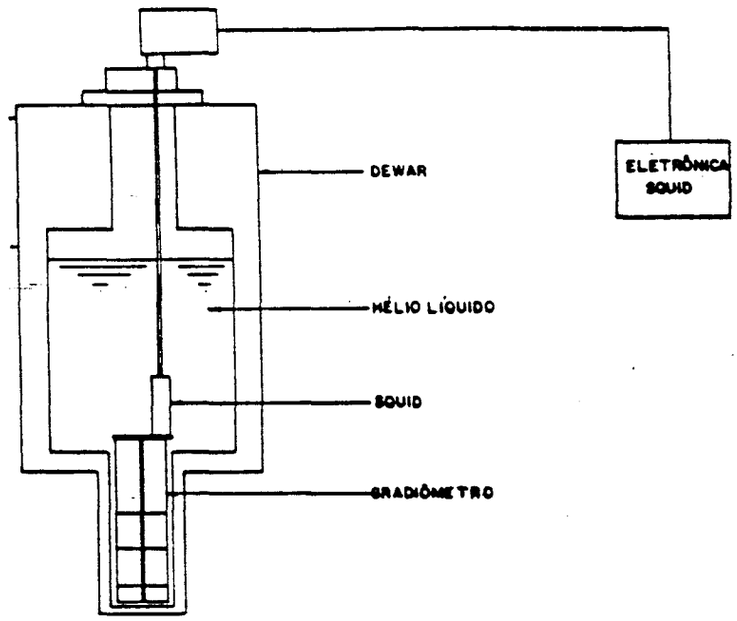

Fig. 1.1 - Desenho esquemático de um sistema para medidas biomagnéticas.

A figura 1.1 mostra esquematicamente o sistema criogênico contido em um *dewar* de fibra de vidro com superisolamento [67]. O reservatório de hélio líquido, necessário para manter o circuito supercondutor a uma temperatura de 4.2° Kelvin, usualmente mantém o sistema frio por alguns dias. O campo magnético que passa através da bobina de detecção é sentido pelo SQUID através da corrente supercondutora existente no circuito composto pela bobina de detecção e por uma bobina interna ao SQUID. Com a bobina interna fortemente acoplada, esta super-

corrente impõe um fluxo magnético ao SQUID, que com a ajuda de uma eletrônica, transforma este fluxo em tensão. A tensão de saida é linearmente proporcional ao fluxo de entrada por varias décadas de frequência. Os SQUIDs não são dispositivos passivos, eles precisam ser polarizados ou por rádio frequência (rf-SQUIDs) [68-69] ou por corrente contínua (dc-SQUIDs) [70- 71]. Os rf-SQUIDs são bastante confiáveis, relativamente simples de serem construídos e estão disponíveis comercialmente desde meados da década de setenta. Os dc-SQUIDs, embora disponíveis comercialmente há alguns anos, ainda são objetos de estudo [72- 73]. A princípio os dc-SQUIDs podem ser mais sensíveis que os rf-SQUIDs por várias ordens de magnitúde.

Como já foi dito, a medida de campos biomagnéticos só é possível através da redução do ruído magnético presente no ambiente onde as medidas são realizadas. Esta redução geralmente é feita de duas formas: 1- utilização de câmaras magneticamente blindadas [74- 76] de forma a isolar o paciente e o instrumento de medida do ruído ambiental e 2- utilização de sensores que acoplados ao SQUID sejam capazes de discriminar fontes distantes (ruído) em favor de fontes próximas ao sensor (sinal biomagnético). A primeira técnica, do ponto de vista de um laboratório urbano ou de um hospital, não é muito conveniente, devido ao seu alto custo de fabricação e ao desconforto para o paciente devido ao pouco espaço usualmente disponível em seu interior. A segunda técnica é conhecida como discriminação espacial e os sensores como gradiômetros já que medem diferenças ou derivadas do campo no espaço. Os gradiômetros podem ser axiais, confeccionados com fio supercondutor enrolado em volta de um mandril cilíndrico, ou podem ser planares, integrados junto com dc-SQUIDs em um substrato de silício. A discriminação espacial será estudada a partir do próximo capítulo.

2 GRADIÔMETROS AXIAIS

Neste capítulo será abordado o princípio básico de funcionamento dos gradiômetros axiais, seu projeto, sua construção, medidas de performance e calibração. Detalhes adicionais podem ser encontrados na publicação [1].

2.1 - Caracterização Usando a Expansão de Taylor

Considere que uma fonte pode ser modelada por um dipolo magnético $\mathbf{m}$ e produz um campo $\mathbf{B}$ $(\mathbf{r})$ dado por [77]:

$$\mathbf{B}(\mathbf{r}) = \frac{\mu_0}{4\pi}\left[\frac{3(\mathbf{r}.\mathbf{m})r}{r^5} - \frac{\mathbf{m}}{r^3}\right]. \tag{2.1}$$

O fluxo devido a este dipolo em uma espira de uma bobina sensora pode ser expresso como:

$$\int_{\mathbf{A}} \mathbf{B}(\mathbf{r})\, d\mathbf{A}\,, \tag{2.2}$$

onde $d\mathbf{A}$ é um elemento de área e a integral se estende sobre toda área da bobina. Substituindo Eq. (2.1) na Eq. (2.2) e efetuando a integração, temos que o fluxo devido ao dipolo localizado no eixo da espira e a uma distancia d é:

$$\phi_1 = \frac{\mu_0|\mathbf{m}|}{2R}\left[1 + (\frac{d}{R})^2\right]^{-\frac{3}{2}}, \tag{2.3}$$

onde R é o raio da bobina.

Suponha agora que exista uma outra espira sensora no mesmo eixo a uma distancia b da primeira, portanto a uma distancia $b + d$ do dipolo. O fluxo através dela será dado por:

$$\phi_2 = \frac{\mu_0|\mathbf{m}|}{2R}\left[1 + (\frac{d+b}{R})^2\right]^{-\frac{3}{2}}. \tag{2.4}$$

Se as espiras forem conectadas em série e enroladas em sentidos opostos, constituindo assim um gradiômetro de primeira ordem (Fig. 2.1), o fluxo resultante será dado por:

$$\phi_t = \phi_1 - \phi_2. \tag{2.5}$$

SERVIÇO DE BIBLIOTECA E INFORMAÇÃO - IFQSC
FÍSICA

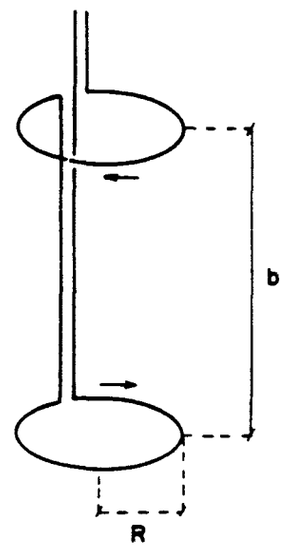

Fig. 2.1 - Desenho esquemático de um gradiômetro de primeira ordem.

Temos então que para fontes distantes ϕ_t tende a zero ($d \gg b$), ao passo que para fontes próximas existirá um ϕ_t não nulo. Este é o princípio básico de funcionamento dos gradiômetros: drástica atenuação de campos provenientes de fontes distantes em relação a campos provenientes de fontes próximas.

De uma forma mais geral, a equação que descreve o fluxo magnético induzido em um conjunto de $(N+1)$ bobinas conectadas em série, cada uma constituida por n_i espiras de mesma área A é (Fig. 2.2):

$$\phi(t) = A\left[\sum_{i=0}^{N} n_i B_z(z_i)\right] f(t), \tag{2.6}$$

onde z_i é a distância da bobina i à origem z_0, $B_z(z)$ é a componente vertical, perpendicular ao plano da bobinas, do campo magnético $B(z)$ e $f(t)$ a dependência temporal deste campo.

Expandindo $B_z(z)$ em série de Taylor em torno da origem z_0 temos:

$$B_z(z) = \sum_{\alpha=0}^{\infty} \frac{B_z^{(\alpha)}(z_0)}{\alpha!}(z - z_0)^{\alpha}\ , \tag{2.7}$$

onde $B_z^{(\alpha)}(z_0)$ é a derivada de ordem α de $B_z(z)$ no ponto z_0. Substituindo a equação acima na Eq. (2.6) teremos:

$$\phi(t) = A\left[\sum_{i=0}^{N}\sum_{\alpha=0}^{\infty} \frac{B_z^{(\alpha)}(z_0)}{\alpha!}(z_i - z_0)^{\alpha}\right] f(t). \tag{2.8}$$

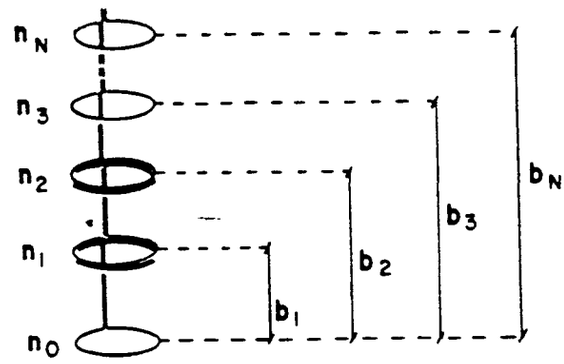

Fig. 2.2 - Desenho esquemático de um conjunto de (N+1) bobinas

Chamando de b_i (linha de base) as distâncias $z_i - z_0$ e explicitando a expansão em $z_0 = 0$ teremos:

$$\begin{aligned}\phi(t) = A\{n_0 B_z(0) + n_1[B_z(0) + B_z^{(1)}(0)b_1 + B_z^{(2)}(0)\frac{b_1^2}{2} + \cdots \\ + n_2[B_z(0) + B_z^{(1)}(0)b_2 + B_z^{(2)}(0)\frac{b_2^2}{2} + \cdots \\ + \cdots\} f(t),\end{aligned} \tag{2.9}$$

ou matricialmente:

$$\phi(t) = (A \quad \cdots \quad A)\begin{pmatrix} U_0 & 0 & \cdots & 0 \\ 0 & U_1 & \cdots & 0 \\ \vdots & \vdots & \ddots & \vdots \\ 0 & 0 & \cdots & U_{N-1} \end{pmatrix}\begin{pmatrix} B_z(0) \\ B_z^{(1)}(0) \\ \vdots \\ B_z^{(N-1)}(0) \end{pmatrix} f(t), \tag{2.10}$$

onde :

$$U_\alpha = \sum_{i=0}^{N} n_i \frac{b_i^\alpha}{\alpha!}, \qquad \alpha = 0, \ldots, N-1. \tag{2.11}$$

A matriz diagonal acima representa o efeito do conjunto de bobinas do gradiômetro sobre o campo e suas derivadas na origem.

A distinção fundamental entre a dependência espacial de uma fonte distante e de uma fonte próxima, é a importância relativa do campo e de suas derivadas num determinado ponto do espaço. No caso da fonte distante, os termos na Eq. (2.10) que envolvem o campo e as primeiras derivadas são predominantes diante do demais. No caso da fonte próxima isto não ocorre.

Para exemplificar, suponhamos que três fontes com uma dependência espacial dipolar $\frac{K}{r^3}$ e com constantes de proporcionalidade K_1, K_2 e K_3 estejam respectivamente a $100, 10$ e 1 unidades de comprimento do ponto de medida z_0. Mesmo

quando $K_1 \gg K_2 \gg K_3$ as derivadas de ordens mais elevadas da fontes distantes tendem a zero, ao passo que as derivadas da fonte próxima tendem a divergir. Isto pode ser observado na Tabela 2.1, para $K_1 = 10^8$, $K_2 = 10^4$ e $K_3 = 1$.

TABELA 2.1

(K,r)	campo	1a derivada	2a derivada	3a derivada
$(10^8, 100)$	100	3	0.12	0.006
$(10^4, 10)$	10	3	1.2	0.6
(1,1)	1	3	12	60

Tabela 2.1 - Derivadas espacias de uma fonte com dependência dipolar $\frac{K}{r^3}$ para vários valores de K e r.

Portanto, se conseguirmos anular os primeiros termos da matriz diagonal da Eq. (2.10), estaremos anulando a contribuição dos sinais provenientes de fontes distantes. Deve ser mencionado que o fato das derivadas de uma fonte próxima divergirem, significa que a expansão de Taylor não é válida para este caso.

Para projetar um gradiômetro de ordem N, assumindo a área A constante, as primeiras (N-1) equações de (2.11) devem ser zeradas de forma a rejeitar o ruído. Por exemplo, um gradiômetro de primeira ordem anula a componente espacialmente constante do campo, portanto $U_0 = 0$. Um gradiômetro de segunda ordem anula a componente constante e a primeira derivada, $U_0 = U_1 = 0$ e assim sucessivamente. Procedendo desta forma temos que o projeto do gradiômetro deve obedecer ao seguinte sistema de equações :

$$\sum_{i=0}^{N} n_i \frac{b_i^\alpha}{\alpha!} = 0, \qquad \alpha = 0, 1, \ldots, N-1. \tag{2.12}$$

O gradiômetro ficará definido ao se conhecer o número de voltas de cada bobina e a distância entre elas, ou seja, o conjunto $\{n_i, b_i \,;\, i = 0, \ldots, N\}$. Por inspeção visual, podemos notar que o sistema (2.12) tem N equações e $2N+1$ incógnitas. Portanto, $N+1$ incógnitas devem ser transformadas em parâmetros para tornar sua solução possível. Dependendo de quais variáveis forem escolhidas, serão gerados dois tipos de soluções. Por exemplo, suponha que os N b_i's $(b_1, b_2 =$

$2b_1, \ldots, b_N = Nb_1$) e um n_i (n_0) sejam escolhidos. Neste caso a solução para o sistema tem a forma da fórmula binomial de Newton [62] :

$$n_i = n_0(-1)^{i-1}\binom{N}{i-1}, \qquad i = 1, \ldots, N-1. \tag{2.13}$$

Esta solução leva ao projeto de gradiômetros convencionais. Por exemplo, um gradiômetro de primeira ordem, como já foi mencionado, será especificado por $n_0 = 1$, $n_1 = -1$ e $b_1 = b$. Um de segunda ordem por $n_0 = 1$, $n_1 = -2$, $n_2 = 1$, $b_1 = b$ e $b_2 = 2b$, e assim sucessivamente.

No entanto, um tratamento mais geral, nunca fora abordado na literatura. Se os $(N+1)\, n_i$'s, forem escolhidos de forma a resolver a primeira equação de (2.12), então mais um incógnita precisa ser escolhida. Suponha que o comprimento total do gradiômetro b_N seja a incógnita escolhida. Neste caso teremos a escolha mais geral possível, pois levará às soluções (2.13) e outras onde os b_i's não serão múltiplos uns dos outros (vide anexo 1). Como exemplo, pode ser citado um gradiômetro de terceira ordem com $n_0 = 2$, $n_1 = -3$, $n_2 = 2$, $n_3 = -1$, $b_1 = 0.15b$, $b_2 = 0.73b$ e $b_3 = b$.

Adotando-se esta última solucão ou a primeira, é necessário algum critério para a escolha de b_N e dos n_i's. O gradiômetro é o produto de um modelo de projeto (expansão de Taylor) que só é possível se a série representada pela Eq. (2.8) convergir. Isto é, se a expansão for válida para a dependência espacial do sinal em questão. Isto significa dizer que a dependência espacial do sinal próximo deve divergir, de forma que o conjunto de bobinas da Fig. (2.2) não funcione como um gradiômetro para este sinal. Vamos exemplificar projetando um gradiômetro de segunda ordem. O sistema a ser resolvido é o seguinte:

$$\begin{aligned} n_0 + n_1 + n_2 &= 0 \\ n_1 b_1 + n_2 b_2 &= 0. \end{aligned} \tag{2.14}$$

Escolhendo os n_i's de forma a satisfazer a primeira equação de (2.14) e de forma a não gerar uma linha de base negativa, (n_2 deve ter sinal contrário a n_1), temos:

$$b_1 = -\frac{n_2}{n_1} b_2. \tag{2.15}$$

Resta agora a escolha de b_2. Para um gradiômetro de segunda ordem, podemos exprimir matematicamente a divergência da Eq. (2.8) como:

$$\lim_{\alpha \to \infty} \left|\frac{T_{\alpha+1}}{T_\alpha}\right| > 1, \tag{2.16}$$

onde,

$$T_\alpha = \frac{B_z^{(\alpha)}(z_0)}{\alpha!}(n_1 b_1^\alpha + n_2 b_2^\alpha), \tag{2.17}$$

e $B_z(z_0)$ é o campo do sinal próximo na primeira bobina. A expressão geral para $B_z^{(\alpha)}$ para campos da forma K/z^m pode ser escrita como:

$$B_z^{(\alpha)}(z) = K\frac{\prod_{i=1}^{\alpha}(m-i+1)}{z^{m+\alpha}}, \tag{2.18}$$

onde z é a distância da fonte a origem, escolhida na primeira bobina. Substituindo as Eqs. (2.15) e (2.18) na Eq. (2.16) e efetuando o limite, temos que $|b_2| > |z|$. Portanto, o comprimento total do gradiômetro deve ser maior que a distância da fonte de sinal biomagnética a primeira bobina do gradiômetro. Com relação a escolha apropriada dos n_i's, outras limitações de natureza prática devem ser levadas em consideração.

2.2 - Aspectos Práticos na Construção de Gradiômetros

Como já foi mencionado, a utilização do gradiômetro se faz juntamente com o SQUID. Este acoplamento é realizado de forma indutiva, utilizando um transformador de fluxo onde o secundário é colocado no interior do SQUID e o gradiômetro funciona como primário deste transformador [78]. Como se trata de um circuito supercondutor, para um fluxo externo ϕ_e aplicado ao gradiômetro, temos:

$$\phi_e + (L_g + L_s)i_s = 0, \tag{2.19}$$

onde L_g e L_s são respectivamente as indutâncias do gradiômetro e do secundário no interior do SQUID, e i_s é a corrente supercondutora gerada. Como entre L_s e o SQUID existe uma indutância mútua dada por M_s, existirá portanto, um fluxo ϕ_s induzido no SQUID igual a :

$$\phi_s = \frac{M_s\phi_e}{L_g + L_s}. \tag{2.20}$$

Para rf-SQUIDs comerciais, M_s e L_s são parâmetros fixos, assim a transferência de fluxo ao SQUID é função da indutância do gradiômetro. Para maximizar a transferência de energia L_s e L_g devem ter aproximadamente o mesmo valor. Para

o caso particular dos rf-SQUIDs da Biomagnetic Technologies, Inc. L_s é igual a $2\,\mu H$. A indutância de uma bobina circular pode ser expressa como:

$$L = n^2\, 0.04\, \pi\, R\, (ln\frac{8R}{\rho} - 2)\ \mu H, \tag{2.21}$$

onde, n é o número de voltas da bobina, R é o raio da bobina e ρ o raio do fio que compõe a bobina. Portanto, L_g depende do número de bobinas, número de voltas de cada espira da bobina e da sua área. Assim, o valor de L_g deve ser tal que:

$$\sum_{i=0}^{N} n_i^2\, 0.04\, \pi\, R\, (ln\frac{8R}{\rho} - 2) \leq 2\,\mu H. \tag{2.22}$$

Os gradiômetros são construídos enrolando-se fio de nióbio puro ou nióbio-titânio, com aproximadamente 0.1 mm de diâmetro, sobre um mandril cilíndrico de CELERON ou MACOR™, após a confecção em locais apropriados de sulcos aonde será colocado o fio. O fio é fixado ao mandril com cola tipo *superbonder*. Note que a construção real do gradiômetro projetado, obviamente não vai atender as equações do sistema (2.12), já que é função do processo de contrução utilizado, e a precisão usualmente alcançada é de decímos de milímetro. Isto acarretará que, para um gradiômetro de segunda ordem, a rejeição ao campo não será igual a zero e a rejeição a derivada do campo também não será nula. O chamado desbalanceamento [79] de ordem zero corresponde a não rejeição total do campo e o desbalanceamento de primeira ordem corresponde a não rejeição da derivada do campo. Neste caso, devemos escrever o sistema (2.14) levando em consideração as diferentes áreas de cada bobina:

$$\begin{aligned} n_0 A_0 + n_1 A_1 + n_2 A_2 &\simeq 0 \\ n_1 A_1 b_1 + n_2 A_2 b_2 &\simeq 0. \end{aligned} \tag{2.23}$$

Podemos então, representar um gradiômetro real como um gradiômetro ideal mais o desbalanceamento, que é função da ordem do gradiômetro. Um gradiômetro de segunda ordem real pode ser representado como a soma de um gradiômetro ideal mais uma pequena espira que corresponde a detecção de parte do campo e um pequeno gradiômetro de primeira ordem que corresponde à detecção de parte do gradiente do campo. Note, que este desbalanceamento está relacionado a resposta axial, ou seja, na direcao z do gradiômetro. Além disso, existe também o

SERVIÇO DE BIBLIOTECA E INFORMAÇÃO - IFQSC
FÍSICA

desbalanceamento relacionado ao não perfeito alinhamento dos planos das bobinas isto é, nas direcões x e y.

Para compensação dos desbalanceamentos, várias técnicas podem ser utilizadas [9,22]. A mais simples e bastante confiável consiste no deslocamento dentro do gradiômetro de peças supecondutoras [80]. Como, devido ao efeito Meissner, no interior das pequenas peças o campo é nulo, sua aproximação às espiras terá o efeito de área negativa compensando assim os erros no processo de construção. Pode ser observado no sistema (2.23) que atuando nas áreas estaremos afetando tanto o desbalanceamento de ordem zero como o de primeira ordem. Para a precisão usualmente alcançada na confecção dos gradiômetros com diâmetros variando entre 1.5 e 3 cm, são utilizados discos de chumbo entre 0.4 e 1 cm de diâmetro, para o balanceamento axial. Para o balanceamento em relação aos planos das bobinas são utilisados 2 pequenos retângulos posicionados perpendicularmente um ao outro, com os lados variando entre 0.3 $\times$ 0.6 cm e 0.7 $\times$ 1 cm.

2.3 - Testes de Performance e Calibração

Foram contruídos, testados e comparados entre si, vários gradiômetros de primeira, segunda e terceira ordens. Estes testes consistiram na avaliação da relação sinal-ruído do campo magnético gerado pelo coração humano. Pode ser constatado que cada ambiente terá o seu gradiômetro ótimo, já que o seu projeto é sempre uma solução de compromisso entre sinal e ruído, e o ruído será sempre característico do ambiente de medida. Para o caso de gradiômetros não balanceados, um gradiômetro de terceira ordem foi, para o nosso caso, e a escolha mais conveniente, como pode ser constatado na Fig. 2.3.

Como a leitura na saida do SQUID é feita em $Volts$ devemos transformá-la para a unidade de campo magnético $Tesla$, já que a transferência de fluxo do gradiômetro ao SQUID depende da indutância do gradiômetro usado. Esta transformação pode ser feita através das seguintes calibrações: aplica-se ao gradiômetro um campo gerado por um dipolo magnético. O dipolo é realizado através de um pequena bobina circular com diâmetro bem menor do que o diâmetro D do gradiômetro, colocada axialmente à um distância z não inferior a 10 vezes o raio do gradiômetro. Mede-se a corrente aplicada a bobina e calcula-se o fluxo $\phi(z)$ que a bobina gera no gradiômetro:

$$\phi(z) = \frac{\mu_0 m}{D}(1 + \frac{4z^2}{D^2})^{-3/2}. \tag{2.24}$$

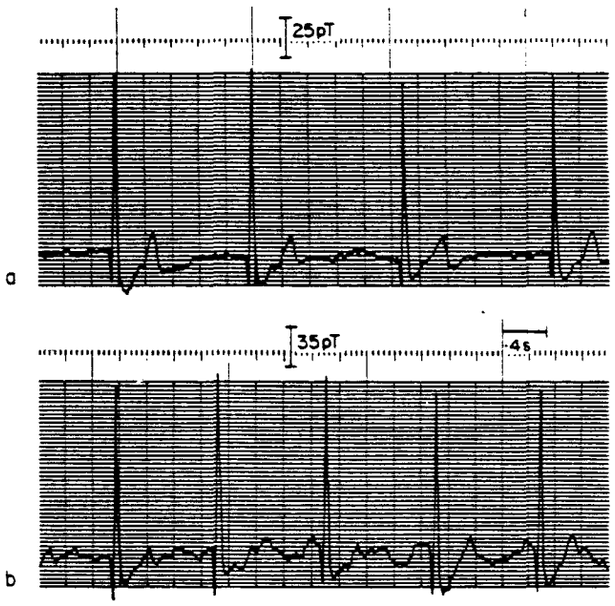

Fig. 2.3 - Comparação de um sinal magnetocardiográfico obtido por um gradiômetro de terceira ordem (a) e um gradiômetro de segunda ordem (b) sob as mesmas condições .

Observando a tensão na saída do SQUID e dividindo o fluxo no gradiômetro pela área efetiva da primeira bobina, obteremos a relação *tesla/volt*.

Um outro método que também pode ser utilizado, consiste na colocação de uma bobina em volta da cauda do *dewar* criogênico que contém o sistema. Move-se a bobina ao longo do gradiômetro, até a saida do SQUID apresentar uma tensão máxima. Da geometria do gradiômetro e da bobina, e das suas posições relativas, a indutância mútua entre os dois pode ser calculada [81]. Multiplicando-se a corrente na bobina pela indutância mútua, tem-se o fluxo aplicado ao gradiômetro. Dividindo o fluxo no gradiômetro pela área efetiva da primeira bobina, obteremos a relação *tesla/volt*. Na Tabela 2.2 podem ser observados as calibrações C *tesla/volt* medidas para diversos gradiômetros construídos no laboratório.

O método pelo qual se avalia a rejeição de um gradiômetro à componente espacialmente constante do ruído, consiste na geração de um campo constante no espaço, em uma frequência temporal conhecida, na região do gradiômetro. As peças supercondutoras são então deslocadas no seu interior, de forma a anular o campo aplicado. Foram contruídas no laboratório, dois tipos de bobinas para a geração deste campo uniforme. A primeira consiste em um par de Helmholtz com aproximadamente 1 m de diâmetro. A segunda consiste em um conjunto de quatro bobinas quadradas [82] formando aproximadamente um cubo de 1 m de lado.

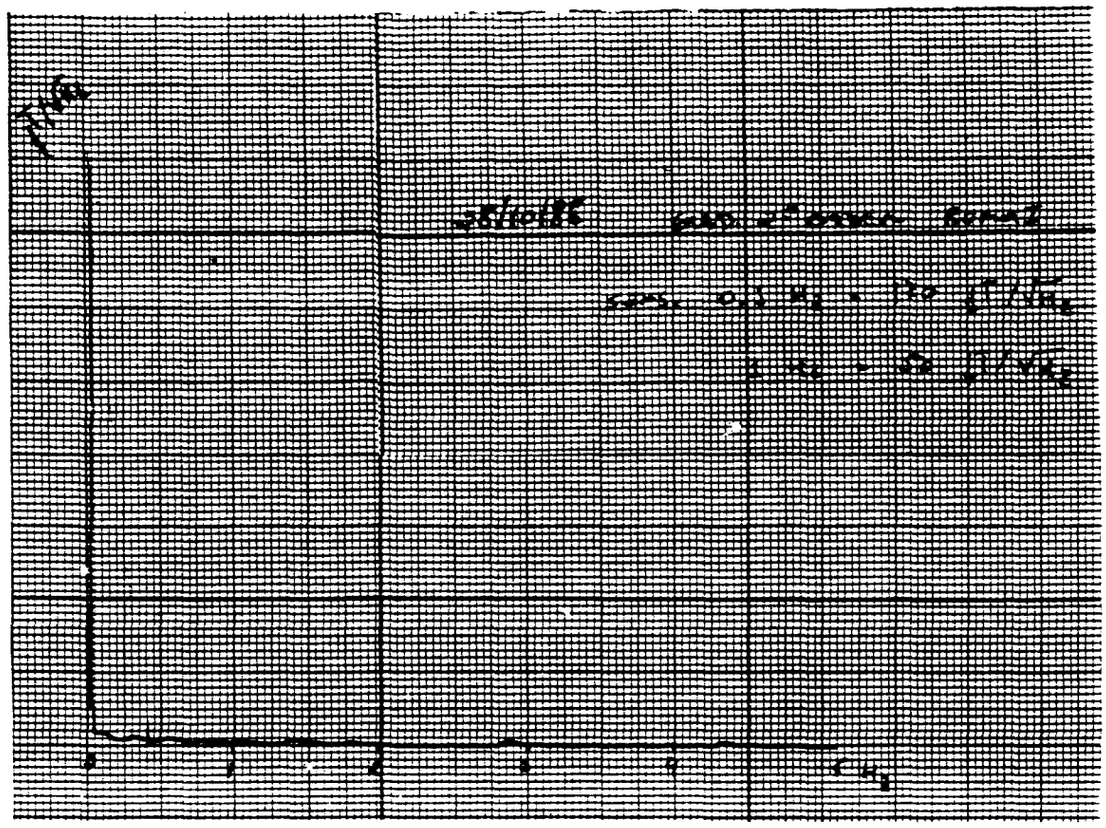

Fig. 2.4 - Espectro de frequência de um gradiômetro segunda ordem balanceado.

TABELA 2.2

Ordem	n_i's	b_i's	$D(cm)$	$L(\mu H)$	C
segunda	1,-2,1	0,5,10	1.5	0.4	6.5×10^{-8}
segunda	3,-6,3	0,5,10	1.5	1.5	2.9×10^{-8}
segunda	4,-8,4	0,4,8	1.5	2.0	2.5×10^{-8}
segunda	1,-2,1	0,5,10	3.0	0.8	2.3×10^{-8}
terceira	2,-3,2,-1	0,3.1,14.6,20	3.0	1.9	1.6×10^{-8}

Tabela 2.2 - Calibrações medidas de diversos gradiômetros construídos. As calibrações estão em ordem crescente de sensibilidade.

A uniformidade do campo gerado pelo segundo conjunto de bobinas é melhor que 10^{-4} dentro de um volume de $10 \times 10 \times 10$ cm no centro do cubo.

Na Fig. 2.4 pode ser observado o espectro de ruído de um gradiômetro de segunda ordem balanceado. A linha de base do spectro é $50\, fT/\sqrt{Hz}$.

Definindo o desbalanceamento como o fator de rejeição do gradiômetro ao campo aplicado, temos que aplicando um campo em três direções perpendiculares e sabendo sua intensidade, poderemos obter o valor da rejeição. O valor normalmente conseguido está na faixa de -60dB a -40dB, para gradiômetros sem balanceamento. Balanceando-se o gradiômetro este fator pode chegar a -100dB.

Um método prático de se certificar que o gradiômetro está bem balanceado é o seguinte: além da eliminação dos picos de frequência indesejáveis no seu espectro, deve ser comparado o valor da linha de base em frequências mais altas, por exemplo 400-500 Hz com o valor da linha de base em baixas frequências, por exemplo 0-10 Hz. Se estes valores forem semelhantes o gradiômetro está bem balanceado.

3 FILTROS ESPACIAIS

Neste capítulo um novo modelo para gradiômetros, baseado em conceitos de filtragem digital, é introduzido. Novos tipos de projeto são propostos, a função de transferência experimental é medida e também é rediscutida a calibração do sistema. Nas publicações [2], [3], [4], [5], [10] e [12] detalhes adicionais podem ser encontrados. Vale ressaltar que até então a descrição de um gradiômetro usado por determinado laboratório era feita com base em suas características geométricas (diâmetro, comprimento, número de bobinas etc.)

3.1 - Caracterização Usando a Transformada de Fourier

A relação entre um gradiômetro e um filtro espacial pode começar a ser entendida se utilizarmos o chamado princípio da reciprocidade [83- 85]. Note que o campo produzido por uma espira quando percorrida por um corrente I é:

$$B(d) = \frac{\mu_0 I}{2R}[1 + (\frac{d}{R})^2]^{-\frac{3}{2}}, \tag{3.1}$$

onde d é a distancia ao ponto de medida e R o raio da bobina. O chamado campo recíproco dado pela Eq. (3.1) tem a mesma dependência em R e em d que o fluxo dado pela Eq. (2.3). Isto significa que, o fluxo induzido em uma espira por um dipolo magnético colocado em seu eixo, cai com a distancia da mesma forma que o campo axial que ela produz quando percorrida por uma corrente I. Utilizando esta reciprocidade, está esquematizado na Fig. 3.1 o fluxo induzido por uma fonte dipolar, em uma única espira e em um gradiômetro de primeira ordem, em função da distância.

Como pode ser observado, a sensibilidade do gradiômetro à fontes mais distantes é muito menor do que a de uma bobina. Podemos então, associar o gradiômetro a um filtro *passa-perto*. Este princípio poderia ser bastante útil para se comparar o desempenho dos diversos tipos de gradiômetros. Contudo, o princípio da reciprocidade só é valido para fontes que possam ser modeladas através de dipolos magnéticos, que é o caso do ruído. No caso do sinal biomagnético, por razões físicas, as fontes são modeladas por dipolos de corrente [86- 87], que tem uma dependência espacial diferente. Portanto não podemos utilizar o princípio da reciprocidade para avaliar a discriminação espacial efetuada por determinado

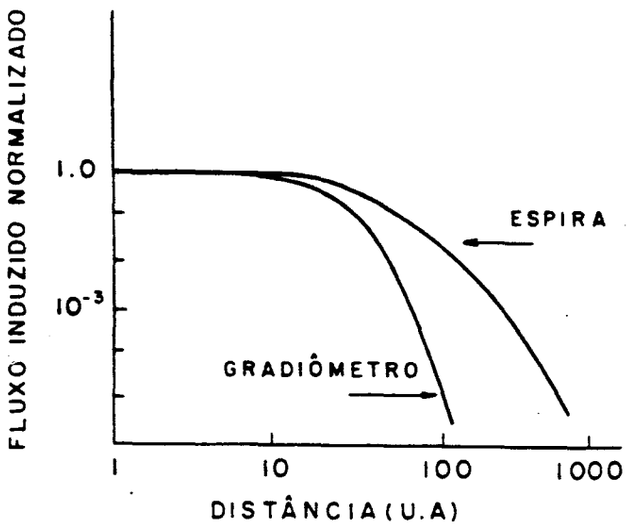

Fig. 3.1 - Sensibilidade de um bobina e de um gradiômetro de primeira ordem a uma fonte dipolar em função da distância.

gradiômetro. Este incoveniente pode ser superado se pensarmos no gradiômetro com um filtro não no domínio das distâncias mas no domínio das frequências espaciais (vide anexo 2). Além disso, o gradiômetro será visto como um dispositivo digital, que atua em pontos discretos no espaco (vide anexo 3)

O gradiômetro é um dispositivo que amostra sinal e ruído variantes no tempo, em pontos discretos no espaço, que correspondem às posições das bobinas. Portanto, trata-se de um amostrador espacial. O período de amostragem espacial é dado pela distância mínima entre as bobinas λ_s. Além disso, é feita a soma ponderada dos sinais amostrados em cada instante de tempo. Os fatores de ponderação dependem da área de cada bobina. Portanto, o gradiômetro é um filtro espacial não recursivo. Isto pode ser melhor compreendido através dos seguintes argumentos (vide anexo 5): os elementos básicos de um filtro digital são o *unit delay* o somador e o multiplicador. Portanto, filtros digitais são coleções de interconexões dos três elementos acima [88]. Podemos encontrar no gradiômetro todos os elementos corrrespondentes aos do filtro digital. O período de amostragem λ_s corresponde ao *unit delay* . O fato das bobinas estarem enroladas em série corresponde ao somador. Finalmente, o fato de medirmos o fluxo, que em primeira aproximação é o campo multiplicado pela área de cada bobina, corresponde ao multiplicador. Parece então apropriada, a utilização de um formalismo matemático digital para descrever o sensor gradiométrico.

Dentro deste formalismo, a saída de um filtro não recursivo também chamado *moving average filter* pode ser expressa como [89]:

$$y_m = \sum_{i=-\infty}^{\infty} h_i x_{m-i}. \tag{3.2}$$

Este procedimento define um novo conjunto de numeros y_m provenientes do conjunto x_m, que corresponde a entrada do filtro amostrada em intervalos constantes. Os fatores de ponderação h_i determinarão a característica do filtro. A grande vantagem da utilização deste formalismo está no fato de podermos caracterizar o gradiômetro e portanto a sua atuação, independente de qualquer suposição prévia sobre o comportamento espacial de sinal e ruído (vide anexo 3). Esta caracterização se dará através de uma função de transferência no domínio das frequências espaciais.

Para o caso do gradiômetro, assumimos que as linhas de base b_i podem ser expressas como múltiplos do período de amostragem λ_s, $b_i = \beta_i \lambda_s$, onde β_i são valores inteiros. O sinal detectado pelo gradiômetro na posição z_m, assumindo um numero infinito de bobinas é :

$$\phi(z_m) = A \sum_{i=-\infty}^{\infty} n_i B(z_m - b_i), \tag{3.3}$$

ou considerando a natureza digital do sistema,

$$\phi_m = A \sum_{i=-\infty}^{\infty} n_i B_{m-i}, \tag{3.4}$$

onde A é a área do gradiômetro, n_i é o número de voltas de cada bobina e B_{m-i} é o valor do campo magnético na i-ésima bobina em algum instante do tempo e numa dada posição m.

Se aplicarmos a transformada discreta de Fourier (DFT) na Eq. (3.4) teremos:

$$\mathcal{F}(\phi_m) = \mathcal{F}(A \sum_{i=-\infty}^{\infty} n_i B_{m-i}) \tag{3.5}$$

$$\sum_{m=-\infty}^{\infty} \phi_m e^{-jmk\lambda_s} = A \sum_{m=-\infty}^{\infty} \sum_{i=-\infty}^{\infty} n_i B_{m-i} e^{-jmk\lambda_s}. \tag{3.6}$$

Invertendo a ordem dos somatórios e após algumas manipulações na Eq. (3.6) obtemos:

$$\sum_{m=-\infty}^{\infty} \phi_m e^{-jmk\lambda_s} = A \sum_{i=-\infty}^{\infty} n_i e^{-jik\lambda_s} \sum_{m=-\infty}^{\infty} B_m e^{-jmk\lambda_s}, \tag{3.7}$$

$$\Phi(k) = A\,H(k)\,B(k), \tag{3.8}$$

onde $\Phi(k)$ e $B(k)$ são respectivamente a DFT da saída e da entrada do filtro (gradiômetro) e $H(k)$ é a sua função de transferência. Portanto a função de transferência espacial de um gradiômetro é a DFT do conjunto representado pelo número de voltas de cada bobina. Como no gradiômetro real temos somente $(N+1)$ espiras,

$$H(k) = A \sum_{i=0}^{N} n_i e^{-jik\lambda_s}. \tag{3.9}$$

O espectro de Fourier de um sinal distante só tem componentes de baixas frequências espaciais, enquanto que um sinal próximo tem componentes de baixas e altas frequências (vide anexo 3). Portanto, a discriminação espacial é realizada porque o gradiômetro atua como um filtro passa-alta frequência espacial (Fig. 3.2).

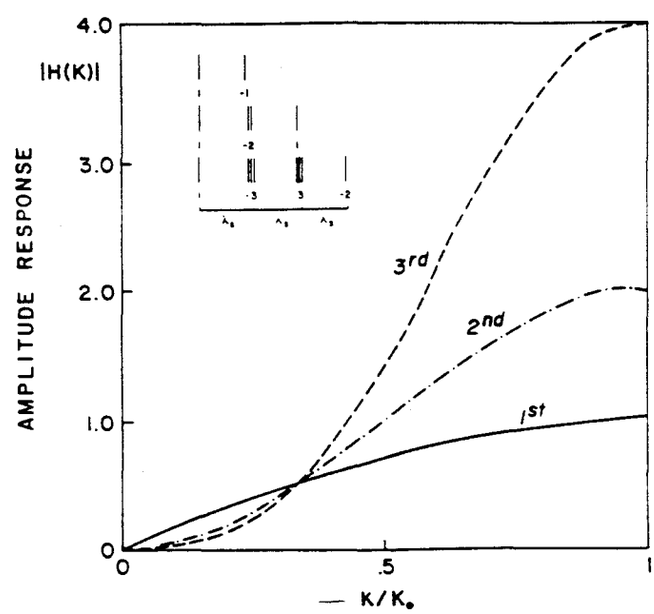

Fig. 3.2 - Funções de transferência de gradiômetros de primeira, segunda e terceira ordens.

3.2 - Projeto de Filtros Espaciais

Será visto como projetar novas e tradicionais configurações de gradiômetros utilizando técnicas de filtragem digital. As configurações tradicionais aparecem se for utilizado um procedimento que parte de projetos de filtros analógicos para se chegar às realizações digitais. Novas configurações aparecerão se forem utilizadas diretamente técnicas de projeto de filtros digitais.

As configurações tradicionais [79] são obtidas se a seguinte técnica de projeto for utilizada para projetar filtros passa-alta. A condição que garante a eficácia de um filtro passa-alta *smooth* é:

$$\frac{\partial^\alpha}{\partial k^\alpha} H(0) = 0, \qquad \alpha = 0, \ldots, N-1 \tag{3.10}$$

onde N é a ordem do filtro. A Eq. (3.10) mostra que se as sucessivas derivadas da função de transferência na origem ($k = 0$) são nulas, sua banda de rejeição se torna mais plana. Esta condição no formalismo de filtragem, é idêntica a condição (2.12) obtida no formalismo de Taylor (vide anexo 2).

Como já foi mencionado, um método de projetar um filtro digital é achar a função de transferência apropriada, $H(s)$, no domínio de Laplace usando a teoria clássica de filtragem. O projeto analógico é então transformado em uma realização digital [90]. Um possível projeto que tem a banda passante da função de transferência plana é conhecido como Butterworth. Contudo a condição expressa na Eq. (3.10) requer a banda de rejeição plana. Apesar disso, o polinômio de Butterworth, $H_b(s)$, ainda pode ser utilizado para projetar a função de transferência desejada, $H_g(s)$ da seguinte forma :

$$H_g(s) = 1 - \frac{1}{H_b(s)}. \tag{3.11}$$

Podemos escrever $H_b(s)$ como:

$$H_b(s) = \frac{1}{1 - s^N}, \tag{3.12}$$

substituindo a Eq. (3.11) em (3.10) temos,

$$H_g(s) = s^N. \tag{3.13}$$

Este $H_g(s)$ assegura uma função de transferência com a banda de rejeição plana, já que obedece a condição expressa na Eq. (3.10).

A realização (3.13) do gradiômetro pode ser feita utilizando alguma das transformações do domínio de Laplace para o domínio digital. Isto consiste em substituir a equação diferencial relacionada com $H_g(s)$ por uma equação *diferença*. Isto é feito realizando a seguinte substituição de variáveis (vide anexo 5):

$$s = 1 - z^{-1}, \tag{3.14}$$

onde z é a variável no domínio digital ($z = e^{jk\lambda_s}$). Portanto, $H(z)$ pode ser escrita como:

$$H(z) = (1 - z^{-1})^N. \tag{3.15}$$

Por exemplo para $N = 1$ teremos:

$$H(z) = 1 - z^{-1}, \tag{3.16}$$

para $N = 2$,

$$H(z) = 1 - 2z^{-1} + z^{-2}, \tag{3.17}$$

e assim sucessivamente. Estas expressões dos filtros não recursivos, tem embutidas todos os elementos necessários à construção do gradiômetro. O primeiro elemento da Eq. (3.17) representa a primeira bobina com 1 volta. O segundo, uma bobina com 2 voltas em sentido oposto à um distancia λ_s da primeira. Finalmente o terceiro, uma bobina com 1 volta no mesmo sentido da primeira e a $2\,\lambda_s$ da primeira. Assim, as mesmas configurações utilizando a Eq. (2.13) são obtidas com este novo formalismo, só que agora de uma forma mais geral e com uma justificativa lógica.

Se utilizarmos agora uma técnica de projeto que use diretamente conceitos de filtragem digital, obteremos novos tipos de filtros espaciais passa-alta que não chamaremos mais de gradiômetros, mas de diferenciadores. A diferença entre um gradiômetro e um diferenciador é que o gradiômetro somente funciona com um diferenciador para sinais de baixa frequência espacial (vide anexo 5).

Como já foi visto, a expressão geral para um filtro não recursivo é dada pela Eq. (3.2), onde os coeficientes h_i devem ser considerados como as áreas das bobinas do sensor. Estes coeficientes podem ser obtidos diretamente, calculando-se a transformada de Fourier inversa de $H(k)$:

$$h_i = \frac{\lambda_s}{2\pi} \int_{-\pi/\lambda_s}^{\pi/\lambda_s} H(k)\, e^{jki\lambda_s}\, dk. \tag{3.18}$$

SERVIÇO DE BIBLIOTECA E INFORMAÇÃO - IFQSC
FÍSICA

O diferenciador tem como função de transferência $H(k) = jk$. No domínio digital teremos:

$$H(k) = jk, \quad \text{para} - \pi/\lambda_s < k < \pi/\lambda_s. \tag{3.19}$$

Substituindo a Eq. (3.19) na Eq. (3.18), efetuando a integração , e truncando o resultado para um numero N finito de bobinas, teremos:

$$h_i = \frac{(-1)^i}{i\,\lambda_s}, \qquad \text{para}\, i = 1, \ldots, N \tag{3.20}$$

e para $i = 0$, $h_i = 0$. A truncagem desta sequência vai resultar em um função de transferência com uma característica oscilatória. Entretanto, os *ripples* podem ser virtualmente eliminados ao se utilizar uma técnica de janelamento diferente. Repare que ao trucarmos a sequência (3.20) estamos usando uma janela que tem o valor 1 no intervalo $i = 1, \ldots, N$ e zero no resto. Se ao invés do fator 1, usarmos um janela de Hamming dada pela expressão :

$$w_i = 0.54 + 0.56\, cos(\frac{i\pi}{N}), \qquad \text{para}\, i = 0 \ldots N, \tag{3.21}$$

e multiplicarmos cada termo de (3.20) pelos termos correspondentes em (3.21), obteremos a função de transferência (linha contínua) mostrada na Fig. 3.3. A linha pontilhada na mesma figura é a de um diferenciador ideal. Como pode ser observado, o resultado é bastante satisfatório. Também esta mostrada na Fig. 3.3 a característica (traço-ponto) de um gradiômetro de primeira ordem. Note que para baixas frequências a função de transferência de um gradiômetro é igual a de um diferenciador. No *inset* da Fig. 3.3 estão desenhados esquematicamente um gradiômetro de primeira ordem $n_0 = 1$, $n_1 = -1$, $b_1 = b$ e um diferenciador $n_0 = 0.25$, $n_1 = -0.5$, $n_2 = 1$, $n_3 = -1$, $n_4 = 0.5$, $n_5 = -0.25$, $b_1 = b$, $b_2 = 2b$, $b_3 = 3b$, $b_4 = 4b$ e $b_5 = 5b$.

Pelo menos teoricamente, os diferenciadores são filtros com desempenho superior aos gradiômetros. Isto porque, para baixas frequências, o desempenho é o mesmo, e para altas frequências o ganho é maior.

3.3 - Medida da Função de Transferência

Após estas considerações teóricas, onde se obteve a função de transferência de um gradiômetro, ou de forma mais geral, de um filtro espacial, parece interessante

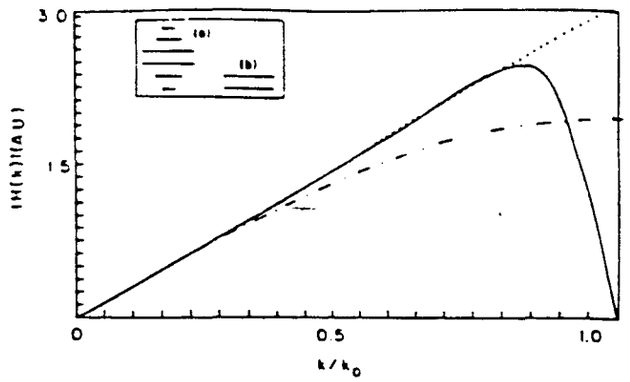

Fig. 3.3 - Funções de transferência de um diferenciador ideal, um diferenciador com um número de bobinas finito e um gradiômetro de primeira ordem.

que essa função de transferência, uma vez construído o filtro, possa ser medida. Isto pode ser realizado, aplicando-se um sinal conhecido ao filtro, e medindo-se a sua resposta como função de uma coordenada espacial (vide anexo 4). Como mostrado em (3.8), se dividirmos a transformada de Fourier do sinal de saída $\Phi_{exp}(k)$ medido, pela transformada de Fourier do sinal de entrada $\mathcal{B}(k)$, estaremos por definição , obtendo a função de transferência real $H_{exp}(k)$ do filtro:

$$H_{exp}(k) = \frac{\Phi_{exp}(k)}{\mathcal{B}(k)}. \tag{3.22}$$

A magnitude de $H_r(k)$ poderá ser então comparada com a magnitude da função de transferência teórica, obtida através da DFT dos coeficientes do filtro (gradiômetro).

A saída do gradiômetro é a soma dos sinais detectados por todas as bobinas. A entrada será considerada como o sinal detectado somente pela primeira bobina do gradiômetro. O sinal de entrada utilizado, será a distribuição espacial do campo magnético gerado por uma bobina. As dimensões desta bobina serão escolhidas conforme os seguintes critérios. O raio da bobina deve ser grande o suficiente, de forma a permitir o seu deslocamento através do *dewar* (Fig. 1.1). Este deslocamento é necessario para termos um valor para a saída em vários pontos no espaço. Contudo, o raio deve ser pequeno o suficiente para gerar um distribuição espacial apropriada para a transformada de Fourier, de forma a evitar o efeito conhecido como *aliasing*. Uma simulação em computador foi feita e um bom compromisso foi alcançado com um raio de cerca de 15 cm.

Uma estrutura foi construída de forma fixar a bobina em relação ao plano $x - y$, permitindo somente movimentos ao longo do eixo do gradiômetro z. O

dewar contendo o gradiômetro, é colocado em um suporte concêntrico em relacao a bobina. A bobina então é deslocada de uma posição 1 m abaixo do centro do gradiômetro à mesma posição acima do centro. A bobina é deslocada em passos de 2.5 cm quando longe, e 1 cm quando perto do gradiômetro. Uma corrente de baixa frequência é aplicada à bobina, e o resultado na saída do SQUID é lido com ajuda de um amplificador *lock-in* . Foram obtidas várias funções de transferências, como exemplo, pode ser visto na Fig. 3.4 as funções de transferências teórica e real de um gradiômetro de segunda ordem.

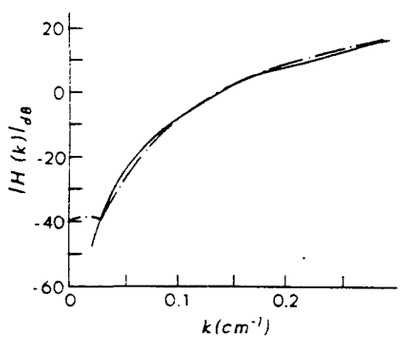

Fig. 3.4 - Funções de transferência teórica (linha contínua) e real (linha pontilhada) de um gradiômetro de terceira ordem.

Uma observação interessante pode ser feita através da Fig. 3.4. Em primeiro lugar, a parte de baixas frequencias $H_{exp}(k)$ é bem diferente da característica teórica devido ao desbalanceamento do gradiômetro. Além disso, o valor do desbalanceamento de ordem zero pode ser obtido diretamente da curva já que é igual a $|H(0)|$.

Foi proposto então (vide anexo 5), a mudança da terminologia tradicionalmente usada para descrição do gradiômetro. A magnitude da Eq. (3.15) pode ser expressa em decibéis como:

$$|H(e^{jk\lambda_s})| = 20\ log[2^N\ sen^N\ (k\lambda_s/2)]\ dB, \tag{3.23}$$

onde N é a ordem do gradiômetro. Em geral a magnitude é dividida em três partes: a banda de rejeição, a banda de transição e a banda de passagem. A banda de rejeição é especificada em termos da máxima rejeição conseguida pelo filtro. Isto no nosso caso é dado por $|H(0)|$. Por exemplo, o gradiômetro da Fig. 3.4 propicía

uma rejeição de 40dB. A ordem do gradiômetro está diretamente relacionada com a sua banda de transição que pode ser especificada pelo seu *rolloff:*

$$-20\ N\ dB/década.$$

A frequencia de corte k_c do filtro que é função da linha de base pode ser expressa como:

$$k_c = (2/\lambda_s)\ sen^{-1}[(0.707)^{1/N}]\ cm^{-1}.$$

Finalmente o ganho máximo será dado por:

$$H(k_m) = 20\ log(2^N)\ dB,$$

onde $k_m = \pi/\lambda_s$. Por exemplo um gradiômetro de segunda ordem com área unitária, com $n_1 = 1$, $n_2 = -2$, $n_3 = 1$, $b_1 = 5cm$ e $b_2 = 10cm$, seria especificado por um *rolloff* de -40 dB/decada, uma frequência de corte igual 0.4 cm^{-1} e um ganho máximo de 12.

3.4 - Calibração

Na seção anterior vimos como medir experimentalmente a função de transferência de um gradiômetro. Deve ser lembrado porém que a saída do SQUID é uma tensão, portanto precisamos convertê-la em campo antes de compararmos as duas curvas. Isto pode ser feito através dos métodos apresentados na seção 2.3. Contudo, foi observado que a medida da função de transferência poderia ser utilizada para determinar o próprio fator de calibração, omitindo a conversão tensão -campo e obtendo uma função de transferência com a dimensão $volt/tesla$. Ajustando a função de transferência experimental pela teórica, o fator de calibração C pode ser encontrado. Este procedimento consiste em achar C que minimiza o erro experimental-teórico para uma determinada faixa de frequências.

Como as medidas são feitas em pontos discretos do espaço, tomou-se o cuidado de tentar minimizar o número de pontos mantendo porém a precisão desejada. Para gradiômetros de segunda ordem comumente usados por diversos grupos de pesquisa (linha de base maior que 4 cm), contatou-se que uma amostragem de 5 cm é suficiente. Esta amostragem precisa se estender até que o sinal de saida do SQUID seja desprezível em relação ao máximo sinal detectado, normalmente 1% é considerado suficiente. Isto em geral acontece a cerca de 50 cm

do centro do gradiômetro, totalizando portanto, 20 pontos a serem medidos. Os métodos de calibração descritos na seção 2.3 tem no máximo uma precisão de 10%. Esta baixa precisão provém basicamente, da incerteza na posição do gradiômetro que está no interior do *dewar* criogênico. Contudo, esta precisão é suficiente para sistemas monocanais já que o erro será o mesmo em todos os pontos de medida. Para sistema multicanais, onde vários sensores medem o campo simultaneamente em diversos pontos do espaço, um método com esta precisão vai implicar em calibrações diferentes para posições diferentes, podendo alterar toda a medida [91]. O método proposto de calibrar através da função de transferência, é independente do exato posicionamento do gradiômetro dentro do *dewar*.Isto porque, qualquer deslocamento constante na posição do gradiômetro quando transformado para o espaço de Fourier, se traduzirá em uma defasagem. Como o ajuste é feito com os módulos das funções de transferências, o método se torna insensível a esta imprecisão. Uma outra vantagem da utilização deste método está no fato de podermos também calibrar gradiômetros planares com o mesmo procedimento. A precisão alcançada pode aumentar em mais de uma ordem de grandeza em relação aos métodos convencionais como ilustra a Fig. 3.5.

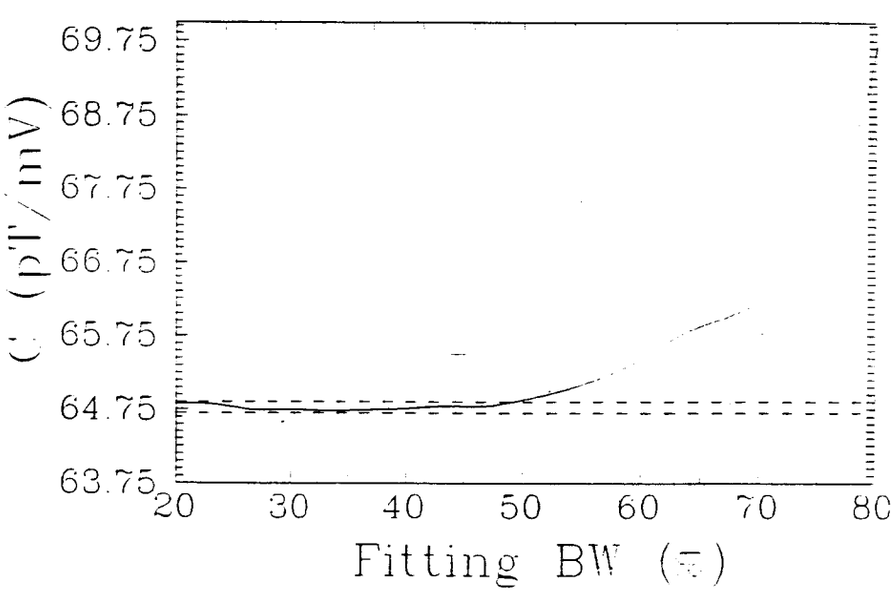

Fig. 3.5 - Calibração em função de banda de ajuste para um gradiômetro de segunda ordem balanceado.

Note que para cerca de 50% da banda de utilização do gradiômetro (0-30 m^{-1}) temos uma incerteza de 5 em 2700 o que corresponde a cerca de 0.2% . Na Tabela 3.1 estão recalibrados todos os gradiômetros apresentados na Tabela 2.2. Note que existem erros na primeira de até 10%.

TABELA 3.2

Ordem	n_i's	b_i's	$D(cm)$	$L(\mu H)$	C
segunda	1,-2,1	0,5,10	1.5	0.4	$6.475x10^{-8}$
segunda	4,-8,4	0,4,8	1.5	2.0	$2.710x10^{-8}$
segunda	1,-2,1	0,5,10	3.0	0.8	$2.304x10^{-8}$
terceira	2,-3,2,-1	0,3.1,14.6,20	3.0	1.9	$1.425x10^{-8}$

Tabela 3.1 - Calibrações medidas com o metodo da função de transferência de diversos gradiômetros construídos. As calibrações estão em ordem crescente de sensibilidade.

4 GRADIÔMETROS PLANARES

Neste capítulo o modelo de filtragem digital é estendido para gradiômetros planares, o projeto de *arrays* é discutido e um algoritmo de desconvolução é introduzido possibilitando a recuperação do sinal original. As publicações [6], [7], [8], [9] e [11] contém detalhes adicionais.

4.1 - O Gradiômetro Planar como um Filtro Espacial

Um grande avanço tecnológico está sendo obtido com o uso de técnicas de deposição de filmes finos para a fabricação de dc-SQUIDS e consequentemente de gradiômetros [92- 98]. Como em geral esta deposição se dá sobre uma placa de silício, a configuração destes gradiômetros é planar. Na Fig. 4.1 estão esquematizados dois projetos de gradiômetros planares de geometria linear. Para este caso, quando as espiras estão posicionadas em uma só direção, a aplicação do modelo de filtragem espacial desenvolvido para gradiômetros axiais é direto. A amostragem espacial ocorre agora em uma direção do plano, x por exemplo, portanto a mesma expressão (Eq. 3.9) usada para a função de transferência de gradiômetros axiais serve para gradiômetros lineares.

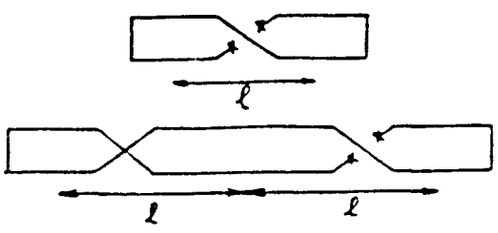

Fig. 4.1 - Projetos de gradiômetros planares.

Devido ao fato de todas as bobinas do gradiômetro estarem em um mesmo plano, não existe, como no caso axial, uma bobina mais sensível ao sinal do que as outras. Portanto, a saída do gradiômetro planar apresenta um sinal que é resultado de somas e subtrações de sinais não monotônicos. Uma análise pode ser feita comparando as sensibilidades de um gradiômetro planar de primeira ordem e um gradiômetro axial de primeira ordem (vide anexo 8). Esta análise

consiste no cálculo das energias de entrada e saída dos gradiômetros no domínio das frequências. A energia de entrada E_i e de saída E_o, podem ser calculadas integrando o quadrado do módulo da transformada de Fourier espacial dos sinais de entrada $\mathcal{B}(k)$ e saída $\Phi(k)$ (teorema de Parseval) [99]:

$$E_i \propto \int_{-\infty}^{\infty} |\mathcal{B}(k)|^2 \, dk, \tag{4.1}$$

e

$$E_o \propto \int_{-\infty}^{\infty} |\Phi(k)|^2 \, dk. \tag{4.2}$$

Assumindo que os dois gradiômetros tem a mesma linha de base, a rejeição ao ruído será a mesma, portanto podemos nos concentrar somente no sinal a ser detectado. Para uma fonte que pode ser modelada por um dipolo de corrente à uma distância igual a linha de base, a Fig. 4.2a mostra o espectro da entrada (linha contínua) e saída (linha pontilhada) do gradiômetro axial e a Fig. 4.2b mostra o espectro da entrada (linha contínua) e saída (linha pontilhada) do gradiômetro planar. Somente por inspeção visual das duas figuras pode ser constatado que o conteudo espectral da entrada e saída do gradiômetro planar é bastante semelhante.

Para uma linha de base igual a 3 cm e uma distância do dipolo também igual a 3 cm, o gradiômetro axial tem na sua saída 35% a menos de energia que a entrada, já o gradiômetro planar tem um ganho de 10% de energia. Se a distância for aumentada para 6 cm, o gradiometro axial tem uma perda de 85% e o planar de 65%.

Na Fig. 4.3 está um sinal, gerado pelo coração humano, obtido através de um gradiômetro planar, confeccionado com fio supercondutor, construído no IESS-CNR com bobinas de 1 *cm* de diâmetro e 2 *cm* de linha de base (vide anexo 7).

4.2 - Projeto de Arrays

Uma das grandes vantagens da fabricação de gradiômetros através da técnica de deposição de filmes fino está no alto grau de balanceamento intrínseco alcançado, tipicamente 10^{-4}. Isto permitirá a fabricação de *arrays* com um número elevado de gradiômetros, sem o uso de técnicas de balanceamento.

Para projetarmos *arrays* de gradiômetros planares (vide anexo 11), vamos supor que as áreas de cada bobina são infinitesimais, portanto estaremos somente

SERVIÇO DE BIBLIOTECA E INFORMAÇÃO - IFQSC
FÍSICA

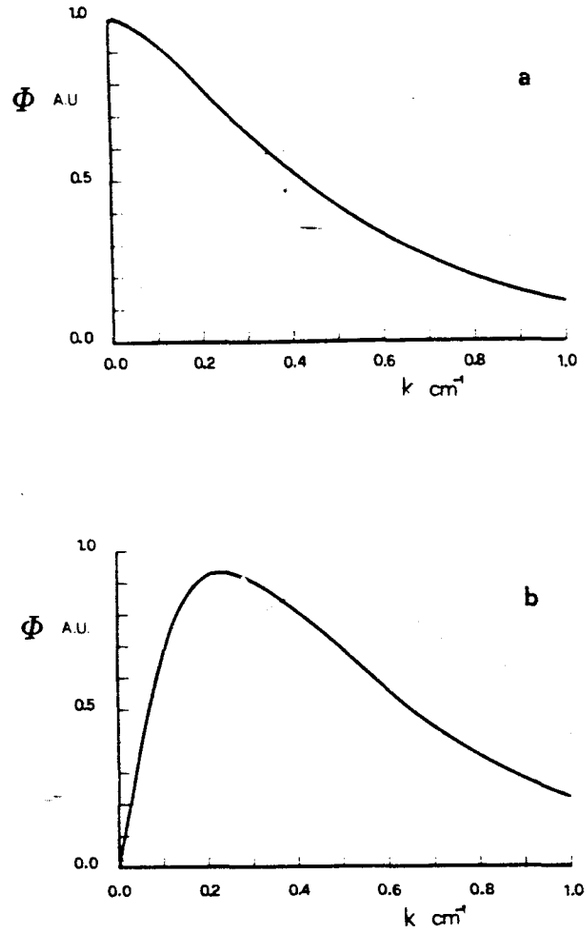

Fig. 4.2 - Espectro de entrada (linha contínua) e saída (linha pontilhada) de um dipolo de corrente detectado por um gradiômetro axial (a) e um gradiômetro planar (b) com linha de base igual a distância do dipolo

preocupados com a sua distribuição espacial. Pelo fato do gradiômetro ser linear, podemos nos concentrar somente no projeto de uma linha do *array*. O projeto será feito analisando a distribuição espacial de um dipolo de corrente, que é o modelo de fonte mais utilizado em biomagnetismo. Na Fig. 4.4 estão varias saídas de diferentes gradiômetros planares para um dipolo de corrente orientado perpendicularmente ao eixo do gradiômetro.

O comprimento L do *array* corresponde ao tamanho da linha de gradiômetros. Este valor pode ser obtido utilizando-se o teorema de Parseval e escolhendo L de forma que a linha de gradiômetros seja capaz de detectar 99% da energia total

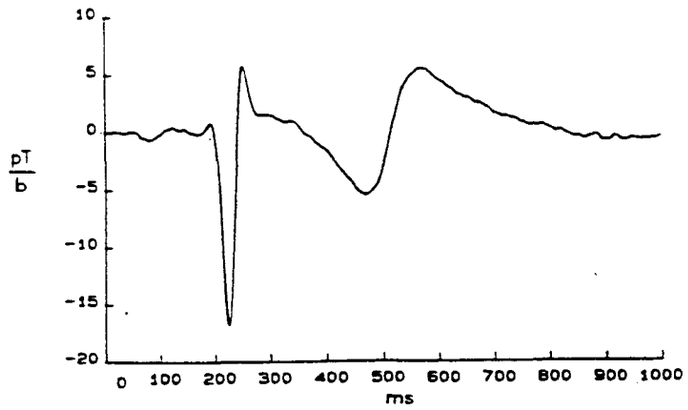

Fig. 4.3 - Sinal magnetocardiográfico obtido com gradiômetro planar no IESS-CNR.

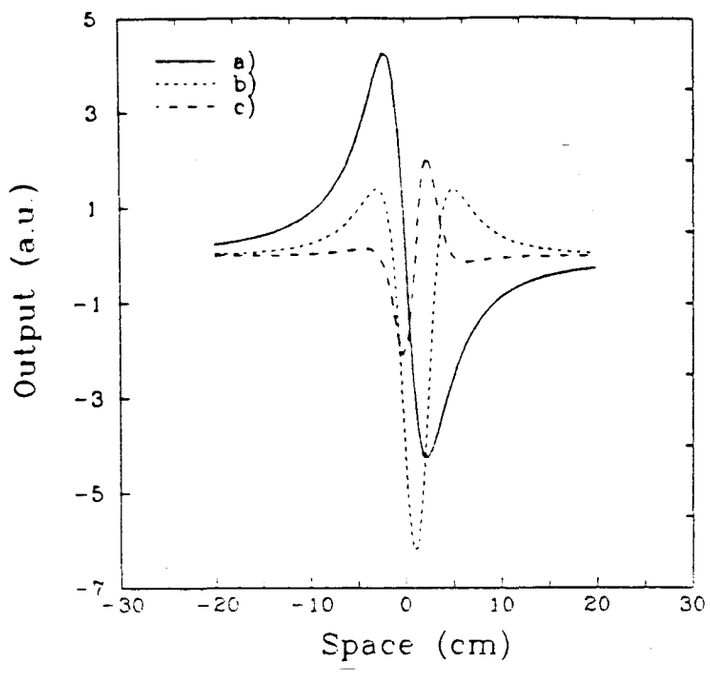

Fig. 4.4 - Campo versus posição para um magnetômetro a), gradiometro planar de primeira b) e segunda c) ordem. A fonte detectada é um dipolo de corrente.

do sinal:

$$99\% \int_{-\infty}^{\infty} \mid B_z(x) \mid^2 \, dx = \int_{-L/2}^{L/2} \mid B_z(x) \mid^2 \, dx. \tag{4.3}$$

Para gradiômetros planares com comprimento total de 2 cm, e para um dipolo a uma profundidade de 3 cm, os valores de L que satisfazem a Eq. 4.3 são 32 cm, 16 cm e 12 cm para respectivamente *arrays* de magnetômetros, gradiômetros

de primeira e segunda ordem. Para uma fonte a 7 cm de profundidade, os valores de L são respectivamente 52 cm, 30 cm e 20 cm. Como pode ser observado, um *array* de gradiômetros pode ser bem menor que um *array* de magnetômetros. Também pode ser notado que o tamanho diminui quando a ordem do gradiômetro aumenta.

Uma vez escolhido o comprimento da linha de gradiômetros, devemos determinar o número de gradiômetros e consequentemente a distância entre eles. Para isto usamos novamente o teorema de Parseval para o domínio das frequências:

$$99\% \int_{-\infty}^{\infty} \mid B(k) \mid^2 \, dk = \int_{-F}^{F} \mid B(k) \mid^2 \, dk, \tag{4.4}$$

Deseja-se determinar F de forma que 99% da energia do sinal esteja presente. Ao se determinar a componente de mais alta frequência espacial F presente no sinal, aplica-se o teorema de Nyquist, por exemplo $0.8P$, para determinar o período de amostragem da linha de gradiômetros, onde P é $1/F$. Os períodos de amostragem deverão ser respectivamente 2.5 cm, 1.7 cm e 1.2 cm para magnetômetros, gradiômetros de primeira e segunda ordem.

Note porem que existe uma sobreposição de gradiômetros já que a linha de base é maior que a distância de amostragem. Isto significa dizer que construir um *array* para detectar uma fonte dipolar com essa profundidade será muito difícil. A profundidade mínima para a não ocorrência de sobreposição em pelo memos *arrays* de primeira ordem é de 4.5 cm. Com esta profundidade temos os respectivos periodos de amostragem para *arrays* gradiômetros de primeira e segunda ordens: 2.5 cm e 1.7 cm. Contudo, devemos lembrar que quando a área de cada bobina for levada em consideração , a dependência espacial se tornará menos rápida e portanto fontes mais superficiais provavelmente poderão ser detectadas com o *array*.

TABELA 4.1

	magnetometro	grad. 1*a* ord.	grad. 2*a* ord.
L (3.0 *cm* prof.)	32 *cm*	16 *cm*	12 *cm*
L (7.0 *cm* prof.)	52 *cm*	30 *cm*	20 *cm*
P (3.0 *cm* prof.)	2.5 *cm*	1.7 *cm*	1.2 *cm*
P (4.5 *cm* prof.)		2.5 *cm*	1.7 *cm*

Tabela 4.1 - Parâmetros de projeto para arrays de magnetômetros, gradiômetros de primeira e segunda ordem.

A Tabela 4.1 resume os resultados encontrados. Para gradiômetros de primeira ordem, o *array* deve ter 30 cm de comprimento com 12 gradiômetros separados por 2.5 cm.

4.3 - Recuperação do Sinal de Entrada

Como já foi dito na seção anterior, no gradiômetro planar não existe uma bobina mais sensível ao sinal do que as outras. Como consequência, a inspeção visual do sinal obtido é de difícil interpretação, sendo neste caso difícil distinguir-se mesmo uma fonte simples, como o dipolo de corrente (Fig.4.5).

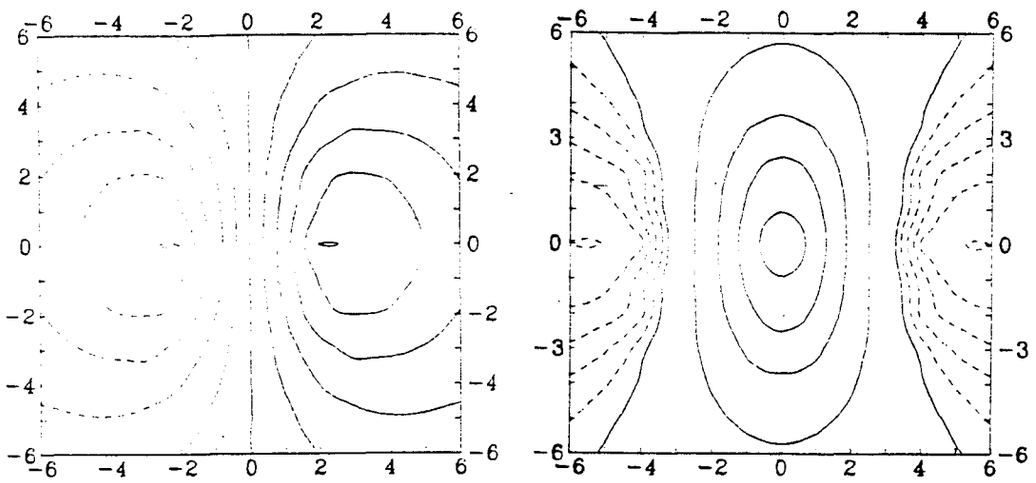

Fig. 4.5 - Isocampos da saída de um gradiômetro axial (a) e de um gradiômetro linear (b).

Como foi discutido na seção 3.1, a transformada de Fourier de saída do gradiômetro é igual ao produto da função de transferência pela transformada de Fourier da entrada. Portanto a seguinte relação também é válida (vide anexo 6):

$$B(k) = \Phi(k) / AH(k), \tag{4.3}$$

Portanto, dado que $H(k)$ seja diferente de zero, poderemos a partir do sinal de saída obter o sinal de entrada através de:

$$B_z(x) = \frac{1}{2\pi} \int_{-\infty}^{\infty} \frac{\Phi(k)}{A\,H(k)} e^{jkx}\, dk. \tag{4.4}$$

No caso de uma amostragem contínua, $B_z(x)$ pode ser recuperado com a precisão desejada, dependendo somente da precisão numérica utilizada.

SERVIÇO DE BIBLIOTECA E INFORMAÇÃO - IFQSC
FÍSICA

Para o caso discreto (vide anexo 9), simularemos a recuperação do campo magnético de um dipolo de corrente detectado por um *array* de 7×7 gradiômetros lineares de primeira ordem. O dipolo foi posicionado em uma direção perpendicular ao eixo do gradiômetro e a z_0 *cm* abaixo. A dependência espacial do campo é dada pela lei de Biot-Savart, que aplicada a este caso consiste na seguinte expressão :

$$B_z(x) = \frac{(x - x_0)}{[(x - x_0)^2 + {y_0}^2 + {z_0}^2]^{-3/2}}. \tag{4.5}$$

A saída será dada então por:

$$\phi(x) = A[B_z(x) - B_z(x - \lambda_s)], \tag{4.6}$$

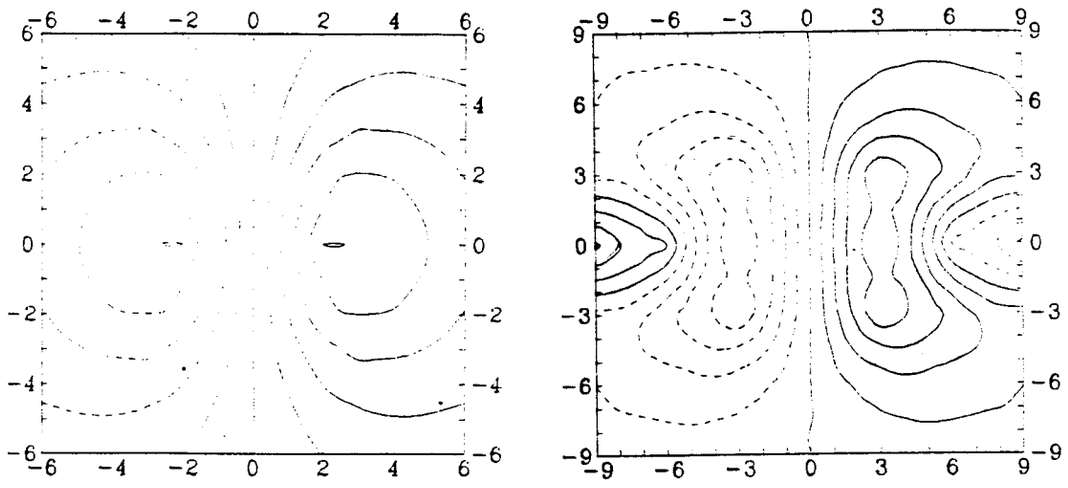

Fig. 4.6 - Campo recuperado depois de detectado por um array de gradiômetros planares de primeira ordem corretamente projetado (a) e com um período de amostragem maior que o correto (b).

Neste caso em que a saída só esta disponível em pontos discretos do espaço, deve se tomar o cuidado de projetar o *array* de forma a não causar o efeito de *aliasing*. Na Fig. 4.6a pode ser visto o campo recuperado depois de detectado por um array de 7×7 gradiômetros planares de primeira ordem. Na Fig. 4.6b note o efeito da utilização de um periodo de amostragem maior que o correto.

5 DISCUSSÃO

5.1 - Perspectivas

Com a recente descoberta de óxidos cerâmicos supercondutores em 1986-1987, materiais com temperaturas críticas acima de 100 K já estão bem estabelecidos. De todas as prováveis e fantásticas aplicações que esses novos materiais podem ter, as mais imediatas são precisamente o SQUID e os gradiômetros, devido a sua operação com baixas correntes críticas. Portanto, imediatamente após a descoberta, varios SQUIDs foram construídos por diversos grupos de pesquisa: IBM [100], Hitachi Corporation [101] , Tsukuba University [102], NBS/NIST [103] and University of Strathclyde [104]. Até então estes dispositivos só serviram para demonstrar os efeitos Josephson e de interferência quântica nestes novos supercondutores. Contudo, uma recente publicação [105] do grupo da IBM relata a utilização de um SQUID imerso em nitrogênio líquido com um nível de ruído similar ao do rf-SQUID para uma faixa de frequências acima de 10 Hz.

O grande progresso da medicina moderna se deve não tão somente ao desenvolvimento de novas tecnologias mas também ao desenvolvimento de uma série de técnicas de obtenção de imagens que dão informações *anatômicas* e *morfológicas* como a tomografia de raio-x computadorizada (CT scan), ressonância nuclear magnética (NMR), tomografia por emissão de pósitrons (PET), ultrasonografia colorida, etc... O eletrocardiograma e o eletroencefalograma, embora extremamente úteis para o estabelecimento de diagnóstico clínico por darem informações sobre a *função* do coração e do cérebro, utilizam até hoje os mesmos métodos de registro e tratamento de sinal de um século atrás, quando da sua invenção. Um dos grandes objetivos da Magnetocardiografia e da Magnetoencefalografia é permitir a obtenção da imagens dos processos funcionais de atividade elétrica cardíaca e cerebral, difíceis de se obter através de eletrodos, com precisão temporal de milésimos de segundo e espacial de poucos milímetros. Para isso atualmente está sendo feito um grande esforço no desenvolvimento de sistemas compostos de *arrays* de gradiômetros, possibilitando assim, medidas simultâneas em vários pontos do espaço [59-61].

5.1 - Conclusão

O objetivo desta tese foi o estudo da detecção de campos magnéticos fracos através da utilização de gradiômetros supercondutores acoplados à SQUIDs e sua aplicação ao biomagnetismo. Um novo modelo teórico para descrição do gradiômetro foi desenvolvido com a obtenção da sua função de transferência espacial. Através desta função de transferência a atuação do gradiômetro sobre os sinais detectados pode ser quantificada. Além disso, foi desenvolvido um procedimento para a medida experimental da função de transferência, onde as imperfeições no processo de construção do sensor podem ser medidas e avaliadas. Foi proposta uma nova terminologia para descrição do gradiômetro ao invés de sua descrição física. Nesta terminologia o gradiômetro ficará especificado pelo seu *rolloff*, frequência de corte espacial e ganho máximo. Também foi generalizado o método para projeto de gradiômetros onde novas configurações podem ser construídas e testadas. A partir da obtenção desta função de transferência um método para calibração *tesla/volt* do sistema foi desenvolvido, com uma precisão até então não alcançada por outros métodos e perfeitamente apropriado para utilização em sistemas multicanais. Finalmente foi desenvolvido um algorítmo de desconvolução para, a partir de sinais detectados com gradiômetros planares, recuperar o sinal original como ele tivesse sido detectado somente por uma bobina. Este algorítmo também pode ser utilizado para auxílio no projeto de *arrays* destes gradiômetros.

6 PUBLICAÇÕES

6.1 Lista de Publicações

1. A Symmetric Third Order Gradiometer Without External Balancing for Magnetocardiography, A.C. Bruno and P. Costa Ribeiro *Cryogenics* **23**, 346 (1983).

2. Spatial Discrimination: An Alternative Approach, A.C. Bruno, P. Costa Ribeiro, J.P. von der Weid and I.R. Eghrari, *Biomagnetism: Application and Theory* H. Weinberg, G. Stroink, and T. Katila (Eds.), Pergamon Press, (1985) p. 60

3. Discrete Spatial Filtering with SQUID Gradiometers in Biomagnetism, A.C. Bruno, P. Costa Ribeiro, J.P. von der Weid and O.G. Symko, *J. Appl. Phys.* **59**, 2584 (1986).

4. Spatial Fourier Transform Method for Evaluating SQUID Gradiometers, P. Costa Ribeiro, A.C. Bruno, C.C. Paulsen and O.G. Symko, *Rev. Sci. Instrum.* **58**, 1510 (1987).

5. Digital Filter Design Approach for Squid Gradiometers, A.C. Bruno and P. Costa Ribeiro, *J. Appl. Phys.* **63**, 2820 (1988).

6. Planar Gradiometer Input Signal Recovery Using a Fourier Technique, A.C. Bruno, A.V. Guida, and P. Costa Ribeiro, *Biomagnetism'87* K. Atsumi et al. (Eds.), Tokyo Denki University Press (1988) p.454

7. Experimental Localization Ability of Planar Gradiometer Systems for Biomagnetic Measurements, A.C. Bruno, V.Pizzella, G. Torrioli and G.L. Romani, *IEEE Trans. Magn.* **MAG-25** (2), 1170 (1989).

8. Neuromagnetic Localization Performed by Using Planar Gradiometer Configurations, A.C. Bruno and G.L. Romani, *J. Appl. Phys.* **65**, 2098 (1989).

9. Spatial Deconvolution Algorithm for Superconducting Planar Gradiometer Arrays, A.C. Bruno and P. Costa Ribeiro, *IEEE Trans. Magn.* **MAG-25** (2), 1216 (1989).

10. Spatial Fourier Technique for calibrating Gradiometers, A.C. Bruno, C.S. Dolce, S.D. Soarez and P. Costa Ribeiro, *Advances on Biomagnetism* S.J. Williamson (Ed.), Pergamon Press (in press)

11. Designing Planar Gradiometer Arrays : Preliminary Considerations, A.C. Bruno and P. Costa Ribeiro, *Advances on Biomagnetism* S.J. Williamson (Ed.), Pergamon Press (in press)

12. Spatial Fourier Method for Calibrating Multichannel SQUID Magnetometers, A.C. Bruno and P. Costa Ribeiro, (submetido ao Rev. Sci. Instrum.)

Estas publicações foram resultado de um trabalho de equipe, executado pelo Grupo de Biomagnetismo no Laboratório da Matéria Condensada do Departamento de Física da Pontifícia Universidade Católica do Rio de Janeiro [1], [2], [3], [4], [5], [6], [9], [10], [11] e [12] e pelo Grupo de Biomagnetismo do Istituto di Elettronica dello Stato Solido, Consiglio Nazionale delle Ricerche, Roma, Italia [7] e [8]. Todas estas publicações foram preparadas e escritas por mim.

6.2 - Resumo das Publicações

1. **A Symmetric Third Order Gradiometer Without External Balancing for Magnetocardiography.**
   Um estudo de viabilidade foi feito para a operação de um gradiômetro não balanceado e utilizado com o SQUID num ambiente não blindado magneticamente. Este artigo compara empiricamente as performances de gradiômetros de segunda e terceira ordens e também apresenta um procedimento geral para projeto de gradiômetros de terceira ordem.

2. Spatial Discrimination: An Alternative Approach.
   O tratamento de gradiômetros como filtros discretos espacias não recursivos é proposto. Esta abordagem torna possível uma descrição analítica da função de transferência do gradiômetro, que é a melhor caracterização de qualquer instrumento de medida.

3. **Discrete Spatial Filtering with SQUID Gradiometers in Biomagnetism.**
   Gradiômetros de primeira, segunda e terceira ordens utilizados em biomagnetismo são analisados como filtros espaciais. As suas funções de transferência independentes do sinal a ser medido são apresentadas e suas amplitude e fase são analisadas. Desta forma, a distorção introduzida no sinal

medido pode ser estimada. De forma a tratar o sinal sob mesmo formalismo, a transformada de Fourier espacial de um sinal produzido por um dipolo de corrente é discutida.

4. **Spatial Fourier Transform Method for Evaluating SQUID Gradiometers.**
   Um método simples para se medir a função de transferência espacial de um gradiômetro é apresentado e o resultado comparado com o modelo teórico. Baseado nesta abordagem, uma nova forma de se apresentar a performance de gradiômetros é proposta; o fator de rejeição é expresso em dB e obtido diretamemte da função de transferência medida.

5. **Digital Filter Design Approach for Squid Gradiometers.**
   Uma revisão do método tradicional de projeto de gradiômetros é feita. Um modelo não recursivo digital para gradiômetros é apresentado, fornecendo uma novo conjunto de parâmetros para a identificação do gradiômetro. Alguns exemplos de gradiômetros são analisados usando o conjunto proposto. Um diferenciador é projetado para ser usado em conjunto com o SQUID. É mostrado que o diferenciador tem a mesma rejeição para ruídos que um gradiômetro convencional mas tem uma maior sensibilidade ao sinal.

6. **Planar Gradiometer Input Signal Recovery Using a Fourier Technique.**
   O objetivo deste artigo é adaptar para gradiômetros planares o modelo de filtragem espacial previamente desenvolvido para gradiômetros axiais. Este modelo possibilitará a interpretação do sinal na saída do gradiômetro sem ser necessário fazer qualquer suposição a respeito da fonte a ser medida.

7. **Experimental Localisation Ability of Planar Gradiometer Systems for Biomagnetic Measurements.**
   A possibilidade de localização de fontes biomagnéticas por gradiômetros planares foi investigada. Um gradiômetro linear de fio supercondutor foi construído e testado. A localização foi feita em um modelo e em humanos. A precisão da localização não foi afetada pelo uso da configuração planar.

8. **Neuromagnetic Localization Performed by Using Planar Gradiometer Configurations.**
   A discriminação espacial de gradiômetros axiais e planares foi comparada utilizando um modelo de filtragem espacial. Medindo campos somatosensoriais evocados, dipolos equivalentes de corrente foram localizados utilizando as configurações planares. As configurações foram obtidas combinando as

saídas de um sistema com quatro canais. Foi observado que com uma relação sinal-ruído apropriada, o uso das configurações planares não afetou significativamente a precisão dos resultados.

9. **Spatial Deconvolution Algorithm for Superconducting Planar Gradiometer Arrays.**
   Um modelo de filtragem espacial usado previamente para analisar gradiômetros é aqui usado para estudar *arrays* de gradiômetros planares de primeira ordem. Como uma aplicação desta técnica um algoritmo de desconvolução do sinal de saída com a função de transferência do gradiômetro foi desenvolvido, possibilitando assim a recuperação do sinal na entrada do *array*. A influência de parâmetros como profundidade da fonte e a densidade de gradiômetros no *array* é discutida.

10. **Spatial Fourier Technique for Calibrating Gradiometers.**
    Neste artigo é proposto um método geral de calibração de gradiômetros axiais e planares. O método é baseado numa técnica de Fourier espacial e no fato do gradiômetro poder ser modelado como um filtro espacial.

11. **Designing Planar Gradiometer Arrays : Preliminary Considerations.**
    Neste artigo é iniciado um estudo sobre o projeto de *arrays* de gradiômetros planares. Parâmetros como tamanho do *array*, e espaçamento entre os gradiômetros são discutidos.

12. **Spatial Fourier Method for Calibrating Multichannel SQUID Systems.**
    Quando se utilizam sistemas multicanais para aplicações biomagnéticas, é de extrema importância a estimação correta da calibração a *tesla/volt* de cada canal, para se evitar erros quando da análise dos resultados. Neste trabalho é proposto um método geral para calibração de sistemas multicanais que fornece uma precisão melhor que 1%.

REFERÊNCIAS

[1] G.M. Baule and R. McFee, *Am. Heart J.* **66**, 95 (1963).

[2] D. Cohen, E.A. Edelsack and J.E. Zimmerman, *Appl. Phys. Lett.* **16**, 278 (1970).

[3] D. Cohen, *J. Appl. Phys.* **38**, 1295 (1967).

[4] J.E. Zimmerman and A.H. Silver, *Phys. Rev.* **141**, 367 (1966).

[5] A.H. Silver and J.E. Zimmerman, *Phys. Rev.* **157**, 317 (1967).

[6] R.L. Fagaly, *Superconductor Industry* **2** (4), 24 (1989).

[7] D. Cohen, *Science* **175**, 664 (1972).

[8] J.E. Zimmerman and N.V. Frederick, *Appl. Phys. Lett.* **19**, 16 (1971).

[9] J.E. Opfer, Y.K.Yeo, J.M. Pierce and L.H. Rorden, *IEEE Trans. Magn.* **MAG-9**, 536 (1974).

[10] M. Saarinen, P.J. Karp, T.E. Katila and P. Siltanen, *Cardiovasc. Res.* **8**, 820 (1974).

[11] D. Brenner, S.J. Williamson and L. Kaufman, *Science* **190**, 480 (1975).

[12] D. Duret, P. Bernard and D. Zenatti, *Rev. Sci. Instrum.* **46**, 474 (1975).

[13] B.N. Cuffin and D.B. Geselowitz, *IEEE Trans. Biomed. Eng.* **BME-24**, 242 (1977).

[14] J.P. Wikswo, Jr., *AIP Conf. Proc.* **44**, 145 (1978).

[15] S. Barbanera, P. Carelli, I. Modena and G.L. Romani, *J. Phys. E: Sci. Instrum.* **11**, 297 (1978).

[16] M. Reite, J. Eldrich, J.T. Zimmerman and J.E. Zimmerman, *Electroencephalog. Clin. Neurophysiol.* **45**, 114 (1978).

[17] D.E. Farrel, J.H. Tripp and R. Norgren, *IEEE Trans. Biomed. Eng.* **BME-26**, 82 (1979).

[18] I.R. Eghrari and P. Costa Ribeiro, *Rev. Bras. Fis.* **10** 115 (1980).

[19] D.B. Geselowitz, *IEEE Trans. Magns* **MAG-6**, 346 (1970).

[20] F. Grynzpan and D.B. Geselowitz, *Biophys. J.* **13**, 911 (1973).

[21] S.J. Williamson and L. Kaufman, *Biomagnetism* S.N. Erné et al. (Eds.), Walter de Gruyter, Berlin-New York, p.353 (1981).

[22] S. Barbanera, P. Carelli, R. Fenici, R. Leoni, I. Modeena and G.L. Romani, *IEEE Trans. Magn.* **MAG-17**, 849 (1981).

[23] P. Nicolas, D. Duret, D. Teszner and T. Tuomisto, *Il Nuovo Cimento* **2D** **(2)**, 184 (1983).

[24] D.F. Farrel, J.H. Tripp, G.M. Brittenham, E.H. Danish, J.W. Harris and A.E. Tracht *Il Nuovo Cimento* **2D** **(2)**, 582 (1983).

[25] P. Costa Ribeiro, I.R. Eghrari, A.C. Bruno, C.A. Bastos, J.P. von der Weid, A.P. Picon e E. Joaquim, *Anais do VIII Cong. Bras. Eng. Biomed.* p.294 (1983).

[26] D. Cohen and L. Kaufman, *Circulation Res.* **36**, 414 (1975).

[27] D. Cohen, E. Lepeschkin, H. Hosaka, B.F. Massel and G. Myers, *Electrocardiology J.* **9**, 398 (1976).

[28] M. Saarinen, P. Siltanen, P.J. Karp and T.E. Katila, *Ann. Clin. Res.* **10** **(21)**, 1 (1978).

[29] D.E. Farrel, J.H. Tripp and R. Norgren, *IEEE Trans. Biomed. Eng.* **BME-27**, 345 (1980).

[30] R. Fenici, G.L. Romani and R. Leoni, *Il Nuovo Cimento* **2D** **(2)**, 280 (1983).

[31] I.R. Eghrari, E. Costa Monteiro, P. Costa Ribeiro, J. P. von der Weid, P.M. Oliveira and A. Paes de Carvalho, *Il Nuovo Cimento* **2D** **(2)**, 346 (1983).

[32] M. Reite, J.E. Zimmerman, J. Eldrich and J.T. Zimmerman *Electroencephalog. Clin. Neurophysiol* **40**, 59 (1976).

[33] J.R. Hughes, J. Cohen, C.I. Mayman, M.L.Scholl and D.E. Hendrix, *J. Neurol.* **217**, 79 (1977).

[34] D.E. Farrel, J.H. Tripp, R. Norgren and T.J. Teyler, *Electroencephalog. Clin. Neurophysiol.* **49**, 31 (1980).

[35] L. Kaufman, Y.C. Okada, D. Brenner and S.J. Williamson *Int. J. Neurosci.* **15**, 223 (1981).

[36] G.L.Romani, S.J. Williamson and L. Kaufman, *Science* **212**, 1339 (1982).

SERVIÇO DE BIBLIOTECA E INFORMAÇÃO - IFQSC
FÍSICA

[37] R.M. Chapman, R. Ilmoniemi, S. Barbanera and G.L. Romani, *Electroencephalog. Clin. Neurophysiol.* **58**, 569 (1984).

[38] H. Hukkinen, V. Kariniemi, T.E. Katila, H. Laine, R. Lukander and P. Makipaa, *Am. J. Obstet.. Gynecol.* **125**, 1115 (1976).

[39] W.H. Barry, W.M. Fairbank, D.C. Harrison, K.L. Lehrman, J.A.V. Malmivuo and J.P. Wikswo,Jr., *Science* **198**, 1159 (1977)

[40] D.E. Farrel, J.H. Tripp, R. Norgren, *Proc. SPIE* **167**, 173 (1978).

[41] P. Siltanen, T. Poutanen, T. Katila, M. Seppanen and T. Varpula, *Il Nuovo Cimento 2D (2),* 301 (1983).

[42] D.S. Barth, W.H. Sutherling, J. Engel and J. Beatty, *Science* **218**, 891 (1982).

[43] I. Modena, G.B. Ricci, S. Barbanera, R. Leoni, G.L. Romani and P. Carelli, *Electroencephalog. Clin. Neurophysiol.* **54**, 622 (1982).

[44] G.M. Brittenham, D.E. Farrel, J.W. Harris, E.S. Feldman, E.H. Danish, W.A. Muir, J.H. Tripp, J.N. Brennan and E.M. Bellon, *Il Nuovo Cimento* **2d**, 567 (1983).

[45] D.F. Rose, S. Sato, P.D. Smith, R.J. Porter, W.H. Theodore, W. Friauf, R. Bonner and B. Jabbari, *Ann. Neurol.* **22**, 348 (1987).

[46] W.W. Sutherling, P. Crandall, L.D. Cahan and D.S. Barth, *Neurology* **38**, 778 (1988)

[47] P. Costa Ribeiro, A.C. Bruno, E. Parenet Ribeiro, J.S. do Carmo, E. Costa Monteiro and A. Fonseca Costa, *Advances in Biomagnetism,* S. J. Willianson (Ed.) in press (1990).

[48] N. Tepley, G.L. Barkley, J. Moran, R.T. Simkins and K.M.A. Welch, *Advances in Biomagnetism,* S. J. Willianson (Ed.) in press (1990).

[49] J.P. Wikswo,Jr., J.P. Barach and J.A. Freeman, *Science* **208**, 53 (1980).

[50] M. Leifer, N. Capos J. Griffin and J. Wikswo,Jr., *Il Nuovo Cimento* **2D (2)**, 266 (1983).

[51] E. Costa Monteiro, A.C. Bruno, S.R.W. Louro, P. Costa Ribeiro and A. Fonseca Costa, *Phys. Med. Biol.* **32**, 65 (1987).

[52] Y.C. Okada, M. Lauritzen and C. Nicholson, *Brain Res.* **442**, 185 (1988).

[53] Y.C. Okada and C. Nicholson, *Biophys. J.* **53**, 723 (1988).

[54] E. Costa Monteiro, S.R.W. Louro, A.C. Bruno and P. Costa Ribeiro, *Biomagnetism'87* K. Atsumi et al. (Eds.), Tokyo Denky University Press, Tokyo, p.310 (1988).

[55] R. Ilmoniemi, R. Hari, K. Reinikainen, *Eletroencephalogr. Clin. Neurophysiol.*, **58**, 467 (1984).

[56] S.J. Williamson, M. Pelizzone, Y. Okada, L. Kaufman, D.B. Crum and J.R. Madsen, *Biomagnetism: Theory and Applications,* H. Wienberg et al. (Eds.), New York, Pergammon Press, p.46 (1984).

[57] G.L. Romani, R. Leoni and C. Salustri, *SQUID 85: Superconducting Quantum Interference Devices and their Applications,* H.D. Hahlbohn et al. (Eds.) Berlin-New York, Walter De Gruyter, p.918 (1985).

[58] J. Knuutila, S. Ahlfors, A. Ahonen, J. Hallstron, M. Kajola, O.V. Lounasmaa, V. Vilkman, and C. Tesche, *Rev. Sci. Instrum.* **58**, 2145 (1987).

[59] H.E. Hoenig, G. Daalmans, W. Folberth, H. Reichenberger, S. Schneider, and H. Seifert, Cryogenics **29**, 809 (1989).

[60] M. Kajola, S. Ahlfors, G.J. Ehnholm, J. Hallstrom, M.S. Hamalainen, R.J. Ilmoniemi, M. Kiviranta, J. Knuutila, O.V. Lounasmaa, C.D. Tesche, and V. Vilkman, *Advances on Biomagnetism,* S.J. Williamson (Ed.), Pergamon, New York, (1989). in press

[61] Biomagnetic Technologies, Inc., 4174 Sorrento Valley Blvd., San Diego, CA 92121, USA.

[62] G.L. Romani, S.J. Williamson, and L. Kaufman, *Rev. Sci. Instrum.* **53**, 1815 (1982).

[63] *SQUID'80, Superconducting Quantum Interferrence Devices and Their Applications,* H.D. Hahlbohm and H. Lübbig (Eds.), Walter de Gruyter, Berlin, (1980).

[64] *SQUID'85, Superconducting Quantum Interferrence Devices and Their Applications,* H.D. Hahlbohm and H. Lübbig (Eds.), Walter de Gruyter, Berlin, (1985).

[65] B.D. Josephson, *Phys. Lett.* **1**, 251 (1962).

[66] A. Barone and G. Paterno, *Physics and Applications of the Josephson Effect,* Willey, New York, (1982).

[67] A.P. Picon, I.R. Eghrari e P. Costa Ribeiro, *Rev. Bras. Fis.* **11**, 863 (1981).

[68] J.E. Zimmerman, P. Thiene and J.T. Harding, *J. Appl. Phys.* **41**, 1572 (1970).

[69] J.E. Zimmerman *Cryogenics* **12**, 19 (1972).

[70] J. Clarke, W.M. Goubau and M. B. Ketchen, *J. Low Temp. Phys.* **25**, 99 (1976).

[71] C.D. Tesche and J. Clarke, *J. Low Temp. Phys.* **29**, 301 (1977).

[72] M. B. Ketchen, *IEEE Trans. Magn.* **MAG-17**, 387 (1981).

[73] V. Foglieti, W.J. Gallagher, M.B. Ketchen, A.W. Kleinsassen, R.H. Koch and R.L. Sandstrom *Appl. Phys. Lett.* **55**, 1451 (1989).

[74] V. Kelhã, J. Pukki, R. Peltonen, A. Penttinen, R. Ilmoniemi and J. Heino, *IEEE Trans. Magn.* **MAG-18**, 260 (1982).

[75] G. Stroink, C. Purcell, F. Brauer and B. Blackford, *Il Nuovo Cimento* **2D** (**2**), 195 (1983).

[76] G.W. Sullivan and E.R. Flynn, *Biomagnetism'87* K. Atsumi et al. (Eds.), Tokyo Denky University Press, Tokyo, p.486 (1988).

[77] John R. Reitz and Frederick J. Milford, *Foundations of Electromagnetic Theory,* Addison-Wesley, Reading MA, (1967).

[78] J.H. Claassen, *J. Appl. Phys.* **46**, 2268 (1975).

[79] J. Vrba, A.A. Fife, M.B. Burbank, H. Weinberg and P.A. Brickett, *Can. J. Phys.* **60**, 1 (1982).

[80] J.A. Overweg and M.J. Walter-Peters, *Cryogenics,* **18**, 529 (1978).

[81] F.W. Grover, *Inductance Calculations,* Dover, New York (1962).

[82] R. Merritt, C. Purcell, and G. Stroink, *Rev. Sci. Instrum.* **54**, 879 (1983).

[83] J. Mallinson, *J. Appl. Phys.* **37**, 2514 (1966).

[84] D.G. Smith, *Am. J. Phys.* **48**, 739 (1980).

[85] J. Storey, *Il Nuovo Cimento* **2D** (**2**), 153 (1983).

[86] J. Sarvas, *Phys. Med. Biol.* **32**, 11 (1987).

[87] B.N. Cuffin, *Phys. Med. Biol.* **32**, 33 (1987).

[88] A. Antoniou, *Digital Filters Analysis and Design,* McGraw-Hill, New York, (1979).

[89] M. Schwartz and L. Shaw, *Signal Processing,* McGraw-Hill, Tokyo, (1975).

[90] A.V. Oppenheim and R.W. Schafer, *Digital Signal Processing,* Prentice Hall, New Jersey, (1975).

[91] P. Costa Ribeiro, S.J. Williamson, and L. Kaufman, IEEE Trans. Biomed. Eng. **BME-35**, 551 (1988).

[92] M.B. Ketchen, W.M. Goubau, J. Clarke and G.B. Donaldson, *J. Appl. Phys.* **49**, 4111 (1978).

[93] V.J. de Wall and T.M. Klapwijk, *Appl. Phys. Lett.* **41**, 669 (1982).

[94] P. Carelli and V. Foglieti, *J. Appl. Phys., bf 54,* 6065 (1983).

[95] F. Wellstood, C. Heiden and J. Clarke, *Rev. Sci. Instrum.* **55**, 952 (1984).

[96] G.J. van Nieuwenhuyzen and V.J. de Waal, *Appl. Phys. Lett.* **46**, 439 (1985).

[97] M.B. Ketchen, *IEEE Trans. Magn.* **MAG-23**, 1650 (1987).

[98] M. Koyanagi, N. Kasai, K. Chinone, M. Nakanishi, S. Kosaka, M. Higuchi and H. Kado, *IEEE Trans. Magn.* **MAG-25** (2), 1166 (1989).

[99] C.T. Chen, *One Dimensional Digital Signal Processing* Dekker, New York (1979).

[100] R.H. Koch, C.P. Umbach, G.L. Clark, P. Chaudhari and R.B. Laibowitz, *Appl. Phys. Lett.* **51**, 200 (1987).

[101] H. Nakane, T. Nishino, M. Hirano, K. Takagi and U. Kawabe, *Extended Abstracts of the 1987 International Superconductivity Electronics Conference ISEC'87,* Japan Society of Applied Physics, Tokyo, p. 411 (1987).

[102] I. Iguchi, A. Sugishita and M. Yanagisawa, *Japan. J. Appl. Phys.* **26**, L1021 (1987).

[103] J.E. Zimmerman, J.A. Beall, M.W. Cromar, R.H. Ono, *Appl. Phys. Lett.* **51**, 617 (1987)

[104] G.B. Donaldson, *Extended Abstracts of the 1987 International Superconductivity Electronics Conference ISEC'87,* Japan Society of Applied Physics, Tokyo, p. 10 (1987).

[105] R.H. Koch, W.J. Gallagher, B. Bumble and W.Y. Lee, *Appl. Phys. Lett.* **54**, 951 (1989).

ANEXO 1

A feasibility study is being carried out on the operation of a SQUID gradiometer without any balancing techniques in a non-shielded environment. This paper compares empirically the performances of second and third order gradiometers; it also presents a general procedure for the design of third order gradiometers, taking into account the measured spatial dependence of the magnetic field of the human heart.

The performance of a third order gradiometer is very promising for a noisy environment; it has a better low frequency noise rejection than the second order gradiometers tested, and needs no external balancing.

A symmetric third order gradiometer without external balancing for magnetocardiography

A.C. Bruno and P. Costa Ribeiro

Key words: superconducting devices, SQUID gradiometer, magnetocardiography

Since the late sixties when SQUID magnetometers became available, various types of biomagnetic fields can be measured. Due to the weakness of these fields in the presence of environmental noise, various techniques have been developed to increase the signal-to-noise ratio especially in clinical applications. Basically there are two ways of rejecting heavy urban magnetic noise: taking measurements in magnetically shielded rooms,[1,2] or by using gradiometers which will perform spatial discrimination against stray magnetic fields from distant sources.[3]

The latter approach has been extensively reported in recent papers.[4,5,6] However, to attain a good performance in the low frequency region, complicated balancing techniques[7,8] have to be used to compensate against imperfections in the construction of the gradiometer.

Our approach does not rely on such balancing techniques hence the overall system is easier to construct and is free from trims, tabs, helmholtz coils, etc. Also our system does not require balancing after each new helium transfer.

The noise problem

The magnetic noise generated by distant sources can be spatially approximated by the first two terms of a Taylor's series expansion:

$$B_z(z-z_0) = B_z(z_0) + \frac{\partial B_z(z_0)}{\partial z}(z-z_0) \qquad (1)$$

where z_0 is the origin of the expansion.

A generation of first and second order gradiometers has been designed based on this assumption. However, unshielded environments often have noise sources which cannot be modelled only by the first two terms of the expansion above. This is the case when noise sources get closer to the gradiometer. So, terms like the second order derivative component ought to be added to this expansion:

$$B_z(z) = B_z(z_0) + \frac{\partial B_z(z_0)}{\partial z}(z-z_0) + \frac{\partial^2 B_z(z_0)}{\partial z^2}\frac{(z-z_0)^2}{2} \qquad (2)$$

If a second order gradiometer is used to measure the heart's magnetic field in such an environment, the noise present in the magnetocardiogram is a function of the field, gradient imbalance and second order components of magnetic noise, which are not rejected by this type of gradiometer. So, it was decided to increase the order of the gradiometer without using balancing techniques, to discover to what extent second order components of magnetic noise are present in the magnetocardiogram.

Spatial dependence of the magnetic field of the human heart

The next step in the design is to find the spatial dependence of the heart's magnetic field in the direction of the gradiometer axis which is usually placed perpendicular to the chest plane. The decrease in the heart's magnetic field (QRS peak-to-peak amplitude falloff) in the direction normal to the chest wall is actually much slower than the decay of a dipolar source, which is commonly used as an approximation for design purposes. This can be checked by using the results reported by Cohen et al[1], where measurements with a single coil magnetometer were performed at six different distances from the chest in two different positions. Plotting their measured QRS peak-to-peak amplitudes versus the distance, Z, from the chest, it was found that the amplitude falloff can be approximately described by an empirical $K/Z^{1/2}$ dependence, where K is a constant. Such a dependence has no physical meaning since the origin of the Z coordinate has been taken at the chest wall, which is far from the heart sources, however it is a good field description for design purposes.

With a slow falloff, it is not possible to neglect the magnetic signal present at the more remote coils of the gradiometer, which disproves the usual assumption that most of the flux coupled to the gradiometer is the induced flux at the lowest coil, the sensing coil. For instance, using the $K/Z^{1/2}$ field dependence, for a conventional second order gradiometer[7] with an overall length of 20 cm and its sensing coil at a distance of 1.1 cm from the chest wall, a net magnetic flux of only 60% of the induced flux at the sensing coil is produced.

0011-2275/83/060324-03 $03.00 © 1983 Butterworth & Co (Publishers) Ltd.

Absolute field measurements cannot be performed without a shielded room, nevertheless, it is possible to check the validity of this $K/Z^{1/2}$ approximation by comparing the calculated and measured net magnetic fluxes detected by gradiometers with different base lines. The difference between calculations using this approximation and measured values, for two distinct gradiometers using the same subject, was approximately 10%.

Designing procedures for a third order gradiometer

The minimum number of coils for a gradiometer of nth order, is[10] $n + 1$. So, a third order gradiometer has a minimum number of four coils with the following turns of the proper polarity: N_1, N_2, N_3, N_4. It also has three base lines, named a_1, b and a_2 which are the distances between the coils.

The flux Φ through a gradiometer of this kind can be expressed as:

$$\Phi = A\,[N_1 B_z(0) + N_2 B_z(a_1) + N_3 B_z(a_1 + b) + N_4 B_z(a_1 + b + a_2)] \tag{3}$$

where A is the area of the loop and the origin is taken in the lowest coil.

Substitution of (2) in the above expression yields:

$$\Phi = A\left\{B_z(0)\,[N_1 + N_2 + N_3 + N_4] + \frac{\partial B_z(0)}{\partial z}\,[N_2 a_1 + N_3(a_1 + b) + N_4(a_1 + b + a_2)] + \frac{\partial^2 B_z(0)}{\partial z^2}\left[N_2\,\frac{a_1^2}{2} + N_3\,\frac{(a_1+b)^2}{2} + N_4\,\frac{(a_1+b+a_2)^2}{2}\right]\right\} = 0 \tag{4}$$

Therefore, the design parameters of the third order gradiometer must satisfy the three following conditions:

$$N_1 + N_2 + N_3 + N_4 = 0 \tag{5}$$

$$N_2 a_1 + N_3(a_1 + b) + N_4(a_1 + b + a_2) = 0 \tag{6}$$

$$N_2\,\frac{a_1^2}{2} + N_3\,\frac{(a_1+b)^2}{2} + N_4\,\frac{(a_1+b+a_2)^2}{2} = 0 \tag{7}$$

Assuming the first condition is satisfied and,

$$a_1 + b + a_2 = l$$

where l is the overall length of the gradiometer, we have the following system with two unknowns (a_1, b) to be solved:

$$N_2 a_1 + N_3(a_1 + b) + N_4 l = 0 \tag{8}$$

$$N_2\,\frac{a_1^2}{2} + N_3\,\frac{(a_1+b)^2}{2} + N_4\,\frac{l^2}{2} = 0 \tag{9}$$

In the particular case of a third order gradiometer with $N_1 = -N_4$ and $N_2 = -N_3$, as it has been reported by Vrba et al,[6] we will have

$$a_1 = a_2 = \frac{1}{2} - \frac{N_4}{2N_2}\,l \tag{10}$$

$$b = \frac{N_4}{N_2}\,l \tag{11}$$

In which case the base line b will be a multiple of the base line a.

For a more general case when such symmetry is not present, the base lines are:

$$a_1 = \left\{\frac{-N_2 N_4 l}{2} + \left[\left(\frac{N_2 N_4 l}{N_3}\right)^2 - \frac{(N_2^2 + N_2 N_3)(N_3 N_4 l^2 + N_4^2 l^2)}{N_3^2}\right]^{-1/2}\right\}\frac{N_3}{N_2^2 + N_2 N_3} \tag{12}$$

$$b = -\frac{(N_2 + N_3)\,a_1 + N_4 l}{N_3} \tag{13}$$

$$a_2 = l - a_1 - b \tag{14}$$

Construction of the gradiometers and performances

Since the magnetic field at any of the gradiometer coils cannot be neglected, there is no reason to make it assymmetric.[2] It was then decided to make the gradiometer symmetric with a coil diameter of 2.3 cm, which is the limit for our construction process.[9]

With a $K/Z^{1/2}$ spatial dependence, a total gradiometer length of 20 cm was arbitrarily chosen so as not to reduce the overall net flux very much. This constraint together with a maximum input matching requirement to the 2 μH inductance at the SQUID, led to a discrete number of only four different configurations for a third order gradiometer (see Table 1). A computer program, given the overall length chosen, tries all the possible number of turns of each coil in order to find solutions in which the sum of the base lines are equal to the overall length and the total inductance is less than 2 μH.

Among the four possible configurations the net fluxes of which vary from 44% to 76%, the gradiometer with the latter net flux was chosen.

Fig. 1 shows two magnetocardiograms taken under the same environmental conditions, with the same subject and position over the chest. The upper, a, was performed with the third order gradiometer and the lower, b, with a second order gradiometer. The bandwidth of, a, was .1-50 Hz of b was 2-50 Hz and a 60 Hz notch filter with $Q = 1$ was used. Both gradiometers have a field imbalance of the order of 1%.

As can be seen after normalizing the QRS peak-to-peak amplitude, there was a significant reduction in the low frequency noise. The second order gradiometer[10] produces the best signal-to-noise ratio among three different second order gradiometers tested (see Table 2). All the second order gradiometers tested are symmetric with the same coil diameter and overall length of the third order gradiometer.

It seems pointless to compare at this point, our sensitivity in femtotesla per Root Hertz with those obtained by other research groups, since no standardization has been made relative to the design parameters of a gradiometer. For instance, a gradiometer with a short overall length, large coil area and a multi-turn sensing coil can produce an outstanding figure in femtotesla per Root Hertz. However, if such a gradiometer is used to measure the human heart, the signal-to-noise ratio will be worse

Table 1. A 3rd order gradiometer configurations

a_1	Base lines, b	a_2	N_1	No of turns of each coil, N_2	N_3	N_4	3rd order gradiometer, Net flux	Inductance, μH
5.00	10.00	5.00	1	−2	2	−1	44%	0.9
5.36	11.55	3.09	1	−2	3	−2	45%	1.5
6.67	6.67	6.67	1	−3	3	−1	47%	1.7
3.09	11.55	5.36	2	−3	2	−1	76%	1.5

Table 2. 2nd order gradiometer configurations tested

a_1	Base lines b	a_2	N_1	No of turns of each coil N_2	N_3	N_4	2nd order gradiometer, Net flux	Inductance, μH
3.00	14.00	3.00	1	−1	−1	1	46%	0.4
10.00	0.0	10.00	1	−1	−1	1	60%	0.6
4.67	12.33	3.00	2	−3	2	−1	96%	1.5

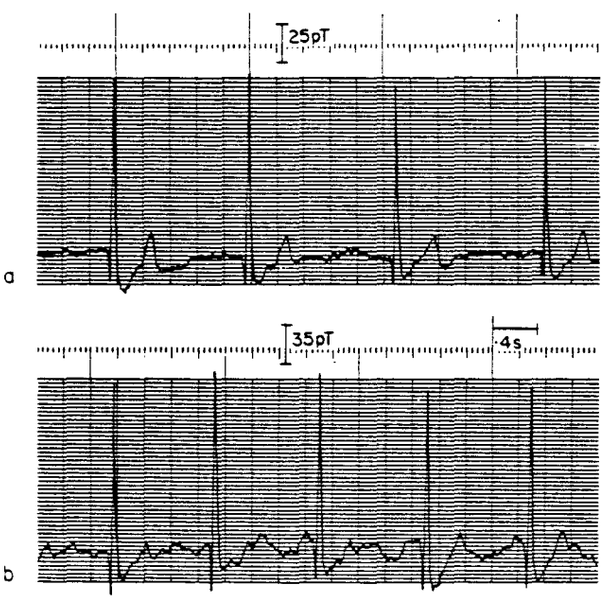

Fig. 1 Comparison between a — third and b — second order gradiometer performances under the same conditions

than that obtained by a gradiometer optimized for that kind of measurement.

The performance of the third order gradiometer proves that second order components of magnetic noise are indeed present in our environment. Regarding the reduction of the low frequency noise and sensitivity to the heart's magnetic field, it seems worthwhile to carry on with our studies, optimizing the overall length of the gradiometer and the coil area.

We would like to thank I.R. Eghrari and Dr. O. Symko for helpful suggestions.

Authors

The authors are at the Dept de Fisica, Pontificia Universidade Catolica de Rio de Janeiro, CP 38071, Rio de Janeiro, Brazil. Paper received 2 March 1983.

References

1 **Cohen, D.** Report of the Low Field Group: The Magnetocardiogram MIT December (1975)
2 **Zimmerman, J.E.** *Journ Appl Phys* 48 (1977) 702
3 **Zimmerman, J.E., Frederick, N.V.** *Appl Phys Letters* 19 (1971) 16
4 **Barbanera, S., et al.** Biomag Measurements Etc, Biomagnetism, S.N. Erné, H.D. Hahlbohm, H. Lübbig (Eds), Berlin, New York (1981) 139
5 **Barbanera, S., Carelli, P., Fenici, R., Leoni, R., Modena, I., Romani, G.L.** *IEEE Trans Magnetics* MAG-17 (1981) 849
6 **Vrba, J., Fife, A.A., Burbank, M.B., Weinberg, H., Brichett, P.A.** *Can Journ Phys* 60 (1982)
7 **Opfer, J.E., Yeo, Y.K., Pierce, J.M., Rorden, L.H.** *IEEE Trans Magnetics* MAG-9 (1974) 536
8 **Overweg, J.A., Walters-Peters, M.J.** *Cryogenics* 18 (1978) 529
9 **Eghrari, I.R., von der Weid, J.P., Costa Ribeiro, P., Symko, O** • On the recording etc., Biomagnetism, S.N. Erné, H.D. Haulbomn, H. Lübbig, (Eds) Berlin-New York (1981) 304
10 **Karp, P., Duret, D.** *Journ Appl Phys* 51 (1980) 1267

ANEXO 2

SERVIÇO DE BIBLIOTECA E INFORMAÇÃO - IFQSC
FÍSICA

SPATIAL DISCRIMINATION: AN ALTERNATIVE APPROACH

A.C. Bruno, P. Costa Ribeiro, J.P. von der Weid and I.R. Eghrari

Departamento de Fisica, Pontificia Universidade Catolica
Cx.Postal 38071, Rio de Janeiro - RJ, BRASIL

ABSTRACT

The treatment of gradiometers as nonrecursive discrete spatial filters in a high-pass configuration is proposed. This approach makes possible an analytical description of the gradiometer's transfer function which is the major characterization of any instrument of measurement.

KEYWORDS

SQUID, Gradiometer, Digital Filtering.

INTRODUCTION

After the introduction of the SQUID, it was the use of gradiometers as sensing coils (Zimmerman, 1971), thereby avoiding the expensive shielded rooms (Cohen, 1975), that led to an increasing number of laboratories studying Biomagnetism. Different types of gradiometers (symmetric, assymmetric, with different orders, sizes and areas) have been built in many laboratories. The main goal in designing a gradiometer has always been to achieve the largest signal-to-noise ratio, and the fact that each group uses a particular type of gradiometer has not been a source of trouble. Nevertheless, with the need to compare data between groups, this lack of standardization must be overcome. In cardiomagnetism, where the magnetic field of the extended source falls off less rapidly than the field of a single current dipole, this problem is especially important. In fact, with such a slow fall off of the field, not only the lowest coil, but the upper coils in the gradiometer contribute to the signal. It would therefore, be interesting to have an analytical description of this device in order to characterize it, enabling one to be conscious of the amount of disturbance introduced in the signal.

GRADIOMETERS SENSING COILS

Traditionally, the equations that define a Nth order gradiometer can be found by considering the total flux, $\phi(t)$, induced in N+1 coils connected in series,

$$\phi(t) = A \left[\sum_{i=0}^{N} n_i \, B_z(z_i) \right] f(t) \qquad (1)$$

where z_i is the distance from the ith-coil to the origin, $B_z(z)$ is the component of the magnetic field perpendicular to the coil's plane, and f(t) incorporates the time dependence of the flux. Each coil consists of n_i turns (positive or negative) taken by simplicity with the same area A. Expanding B_z in Taylor series about z_0 and calling $b_i = z_i - z_0$ the distance between each coil and the lowest one, expression (1) can be given in matrix form:

$$\phi(t) = A\,[111\ldots] \begin{bmatrix} n_0+n_1+n_2+\ldots & & & 0 \\ & n_1b_1+n_2b_2+\ldots & & \\ & & \frac{n_1b_1^2}{2}+\frac{n_2b_2^2}{2}\ldots & \\ 0 & & & \ddots \end{bmatrix} \begin{bmatrix} B_z(z_0) \\ B_z^{(1)}(z_0) \\ B_z^{(2)}(z_0) \\ \vdots \end{bmatrix} f(t) \qquad (2)$$

The diagonal matrix represents the effect on the field, (B_z), and its derivatives, $(B_z^{(i)})$, at the lowest coil, (z_0), due to the gradiometer. If the gradiometer is designed so that the first diagonal terms in the square matrix are cancelled, then the contribution of a far source is diminished but the near source signal is also effected.

Such approach is similar to the classical electronic filtering of a time dependent signal. For instance, the matrix representation of an ideal high-pass filter acting on a function F(t) expanded in Fourier series,

$$F(t) = \sum_{n=0}^{\infty} C_n\, e^{j\omega_n t} \qquad (3)$$

would be:

$$\begin{bmatrix} 0 & & & & & & 0 \\ & 0 & & & & & \\ & & 1 & & & & \\ & & & 1 & & & \\ & & & & 1 & & \\ & & & & & \ddots & \\ 0 & & & & & & \end{bmatrix} \begin{bmatrix} c_0 \\ c_1 \\ c_2 \\ \vdots \end{bmatrix} = \begin{bmatrix} 0 \\ 0 \\ c_2 \\ \vdots \end{bmatrix} \qquad (4)$$

This expression is similar to that of e.g. a second order gradiometer,

$$\begin{bmatrix} 0 & & & 0 \\ & 0 & & \\ & & \frac{n_1b_1^2}{2}+\frac{n_2b_2^2}{2}+\ldots & \\ 0 & & & \ddots \end{bmatrix} \begin{bmatrix} B_z(z_0) \\ B_z^{(1)}(z_0) \\ B_z^{(2)}(z_0) \\ \vdots \end{bmatrix} = \begin{bmatrix} 0 \\ 0 \\ \gamma B_z^{(2)}(z_0) \\ \vdots \end{bmatrix} \qquad (5)$$

where the γ's are the non zero diagonal terms of the square matrix. The similarity between a gradiometer and an electronic filter is stressed by the usual procedure to check gradiometer's unbalance. To measure the cancellation of the first two terms of the gradiometer matrix in a second order gradiometer, a constant field and a constant gradient field are usually applied to the system. That routine is

equivalent to determining the transfer function of an electronic filter by connecting to it a sine wave generator and measuring the output intensity for each frequency. Nevertheless, up to this point, the analogy between a gradiometer and a filter is confined only to the matrix representation. Since the Taylor polynomials do not constitute an orthonormal basis, the gradiometer's transfer function cannot be derived by using the Taylor approach.

GRADIOMETER, A NONRECURSIVE DISCRETE FILTER

A gradiometer detects a signal that is a continuous function of time. The sampling takes place at discrete points in space corresponding to the position of the coils. The net signal measured is a weighted sum of these sampled values. Thus, it is simple to apply digital signal processing techniques (Lehmann, 1983) (Schwartz, 1975) to handle this problem. The output of a nonrecursive or moving-average filter can be defined by the well known expression

$$y_m = \sum_{i=-\infty}^{\infty} h_i \; x_{m-i} \tag{6}$$

This operation defines a new set of discrete numbers y_m from a set of numbers x_m corresponding to values of a variable sampled at constant intervals. Different filters correspond to different coeficients h_i. Although it is common to fit a monotonic function like the $1/r^3$ or $1/r^2$ magnetic field from a magnetic or electric current dipole by a polynomyal expansion, it is possible to describe the field by a Fourier expansion. The discrete Fourier transform of the signal at some instant of time will be

$$X(k) = \sum_{m=-\infty}^{\infty} x_m \; e^{-jmk\lambda_s} \tag{7}$$

where k is the wave number and λ_s is the distance between two successive sampling points.
Assuming that the distances bi can all be expressed as multiples of λ_s, that is

$$b_i = \lambda_s \beta_i \tag{8}$$

β_i being integers and λ_s being therefore just the maximum common divisor of all the b_i, the signal detected by the gradiometer will be given by:

$$Y = \sum_{i=0}^{N} n_i \; x_i \tag{9}$$

where N+1 is the number of coils, n_i is the number of turns of each coil and x_i is the magnetic flux at a given instant of time at the ith coil. The transfer function, defined by $Y(k) = H(k)\,X(k)$, is obtained by taking the Fourier transform of the sequence of filter coefficients:

$$H(k) = \sum_{i=0}^{N} n_i \; e^{-jb_i k}$$

A far source of field (background noise) will mainly have low frequency components, (X(k) will be large near k=0) while a near source (signal) will have high frequency components.

The spatial discrimination will be achieved by making the moving average filter (gradiometer) into a high-pass filter. It is interesting to note that the design conditions for a Nth order gradiometer, obtained by the traditional Taylor approach (Karp, 1980),

$$\sum_{i=0}^{N} n_i \frac{b_i^{\alpha}}{\alpha!} = 0 \qquad \alpha=0,\ldots,N \tag{11}$$

are obtained in the Fourier approach by imposing:

$$\left.\frac{\partial^{\alpha}}{\partial k^{\alpha}} H(k)\right|_{k=0} = 0 \qquad \alpha=0,\ldots,N \tag{12}$$

CHOOSING GRADIOMETERS' DESIGNS

This alternative approach to the study of gradiometers provides a new tool for optimizing the choice of gradiometer parameters for each specific situation, as is illustrated by figures 1 and 2 and the brief outline presented below. Figure 1 shows the transfer function magnitude H(k) as defined by (10) for first, second and third order symmetric gradiometers. The gradiometers' total length are the same (10cm) and therefore the sampling period λ_s are respectively 10, 5 and 2.5 cm. As is the case for the discrete Fourier transform, the highest meaningful frequency is π/λ_s or 0.31, 0.62 and 1.26cm^{-1} respectively.

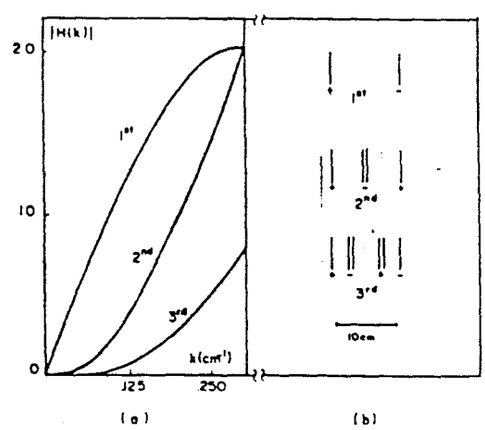

Figure 1(a). Magnitude of the gradiometers' transfer function and (b) their schematic geometries.

All the transfer functions are high-pass filters with the gradiometers of higher order more effectively attenuating low frequency background noise.
For frequencies larger than 0.3 cm^{-1}, the Fourier components of the signal are very small, representing only a few percent of the total power spectrum. This is particularly true for the cardiac magnetic signal. (Bruno, 1984).
The choice between gradiometers of different order will then be determined by the behaviour of the transfer functions for frequencies below 0.3 cm^{-1}. For a severe background noise environment due to not too distant sources, figure 1 indicates

the use of a third order gradiometer even if the signal is also drastically reduced.

The magnitude of the transfer function $|X(k)|$ for different gradiometers described in literature are shown in figure 2. Their areas have been normalized to unity for simplicity. The use of a first order gradiometer with a large base line (curve 1) is perfectly justified in a suburban area where the background noise is very low. The cardiac signal amplitude will therefore, be large since for intermediate frequencies the transfer function amplitude is large. The best choice of the gradiometer lengths can be suggested by comparing two second order gradiometers (curves 2a and 2b). For short lengths (large π/λ_g) (curve 2a) the filter more efficiently attenuates low frequency components, having a large background noise rejection, but also reduces the signal amplitude by attenuating the intermediate frequencies. This short gradiometer is indeed a good choice for studies of brain evoked fields when the gradiometer is near a $1/r^2$ source whose signal contains high frequency components in the signal.

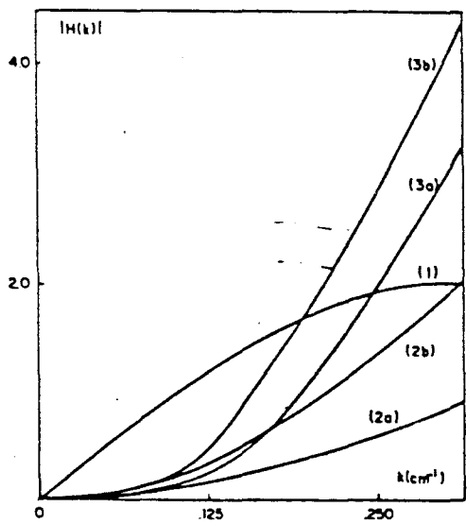

Figure 2. SQUID Gradiometers' Transfer Functions: (1) First Order Gradiometer (total length 10cm) (Saarinen, 1978); (2a) Second Order Gradiometer (total length 6.4cm) (Williamson, 1978); (2b) Second Order Gradiometer (total length 10cm) (Barbanera, 1981); (3a) Third Order Gradiometer (total length 16.5cm)(Vrba, 1982); (3b) Third Order Gradiometer (total length 20cm) (Bruno, 1983).

When measuring cardiac signals in a large background noise environment the choice of a third order gradiometer seems more reasonable to obtain a larger signal to noise ratio (curve 3a and 3b). A second order gradiometer with a larger baseline curve 2b, seems to be a good compromise to handle either cardiac and brain signals. The choice among different gradiometers designs will be imposed by the observation of their transfer functions and the Fourier power spectrum of the signal and the noise.

Finally, the usual measurement of the gradiometer's unbalance to check how far is the real gradiometer from its design, would be replaced by measuring its actual transfer function obtained by detecting the signal due to a magnet, displacing it along the axis of the gradiometer and comparing the Fourier transform of this

signal with the Fourier transform of the dipolar source (Bruno, 1984).

REFERENCES

Barbanera, S., P. Carelli, R. Fenici, R. Leoni, I., Modena, and G.L. Romani, IEEE Trans. Magn. MAG-17 (1981), p. 849.

Bruno, A.C., P. Costa Ribeiro, J.P. von der Weid and O. Symko, (1984) (to be published).

Bruno, A.C. and P. Costa Ribeiro, Cryogenics, vol.23 (1983), pp. 324-326.

Cohen, D., Report of the Low Field Group: The Magnetocardiogram MIT Dec. (1975).

Karp, P., D. Duret, Journ. Appl. Phys. 51 (1980) pp. 1267-1272.

Lehmann, H.P., Signal Processing, Biomagnetism An Interdisciplinary Approach, S.J. G.L. Romani, L. Kaufman and I. Modena (Eds), New York, NATO ASI Series vol.66 (1983), pp. 591-624.

Saarinen, M., P. Siltanen, P.J. Karp and T.E. Katila, Ann. Clin. Res., vol 10, Suppl.21 (1978), pp. 1-42.

Schwartz, M. and S. Leonard, Signal Processing, McGraw-Hill, Tokyo (1975)

Vrba, J., A.A. Fife, M.B. Burbank, H. Weinberg and P.A. Brickett, Can. Journ. Phys., vol.60 (1982), pp. 1060-1071.

Williamson, S.I., D. Brenner and L. Kaufman, AIP Conf. Proc. 44 (1978), p.106.

Zimmerman, J.E. and N.V. Frederick, Appl. Phys. Letters, vol.19 (1971), pp.16-18.

ANEXO 3

time and at a given discrete position in space, labeled by the index m.

The transfer function of the filter (gradiometer) in k space defined as

$$H(k) = F(k)/\Phi(k),$$

where $F(k)$ and $\Phi(k)$ are, respectively, the DFT of f_m and ϕ_m, can be obtained by taking the Fourier transform of the sequence of filter coefficients

$$H(k) = \sum_{i=0}^{N} n_i e^{-jb_i k}. \tag{9}$$

Spatial discrimination is accomplished by making the moving average filter (gradiometer) into a nigh-pass filter. The correctness of such an approach is shown by the fact that the design conditions for the successive higher-order gradiometers obtained by canceling the successive elements of the square matrix in Eq. (3) are obtained, as well, by imposing increasing flatness in the stop-band region of the high-pass filter transfer function. For instance, the design condition for a first-order high-pass filter is obtained by making Eq. (9) equal to zero for $k = 0$. This yields

$$\sum_{i=0}^{N} n_i = 0, \tag{10}$$

which is the same condition as for a first-order gradiometer in the Taylor series approach. For a more efficient high-pass filter the design conditions are obtained by making $H(0) = 0$ and also $|\partial H(k)\partial k| = 0$ at $k = 0$, i.e., the extra condition of

$$\sum_{i=0}^{N} n_i b_i = 0, \tag{11}$$

which is a second-order gradiometer in the Taylor series approach. Generalizing, the gradiometer condition given by Eq. (4) in the Taylor series approach corresponds to imposing

$$\left| \frac{\partial^\alpha}{\partial k^\alpha} H(k) \right|_{k=0} = 0 \tag{12}$$

in the spatial Fourier technique.

The equivalence of both approaches is illustrated by considering the Fourier transform for a spatially constant field and a linearly varying field in space.

For a spatially uniform field, normalized so as to have unit value over all space,

$$\phi_m = 1, \quad -\infty < m < \infty, \tag{13}$$

its Fourier transform becomes[18]

$$\Phi(k) = (2\pi/\lambda_s)\delta(k), \tag{14}$$

$\delta(k)$ being a delta function.

Each discrete measurement of the filter at a given position $m\lambda_s$ will be

$$f_m = \frac{\lambda_s}{2\pi} \int_{-\pi/\lambda_s}^{\pi/\lambda_s} F(k) e^{jm\lambda_s k}\, dk, \tag{15}$$

which becomes

$$f_m = H(0). \tag{16}$$

Thus the condition $H(0) = 0$ eliminates the detection of a spatially constant field.

For a linearly varying field in space,

$$\phi_m = \alpha m \lambda_s, \quad -\infty < m < \infty, \tag{17}$$

its Fourier transform will be

$$\Phi(k) = \sum_{m=-\infty}^{\infty} \alpha m \lambda_s e^{-jm\lambda_s k}. \tag{18}$$

It can be written as

$$\Phi(k) = j\alpha \frac{\partial}{\partial k} \sum_{m=-\infty}^{\infty} e^{-jm\lambda_s k}, \tag{19}$$

i.e., the Fourier transform is the derivative of the delta function. Hence the output of the filter will be

$$f_M = -j\alpha \left. \frac{\partial H(k)}{\partial k} \right|_{k=0} + \alpha m \lambda_s H(0). \tag{20}$$

Thus to discriminate against a spatially linear field we should impose the condition of the transfer function and its first derivative at $k = 0$ to be equal to zero. A similar procedure would be used for higher orders.

Figure 2 shows the magnitude of the transfer functions for conventional first-, second-, and third-order geometries. All the gradiometers have the same λ_s and K_0 is π/λ_s. The behavior in the DFT approach is the inverse of the Fourier series: the space domain is discrete and the frequency domain is periodic with a period of $2\pi/\lambda_s$. Since it is an even function, it is only necessary to represent the half-period dependence, from 0 to π/λ_s.

PHASE CHARACTERISTICS

So far we have dealt with the amplitude response $|H(k)|$ of the gradiometer. There is also a phase response $\theta(k)$, although at first glance it is not as easy to interpret. Figure 3

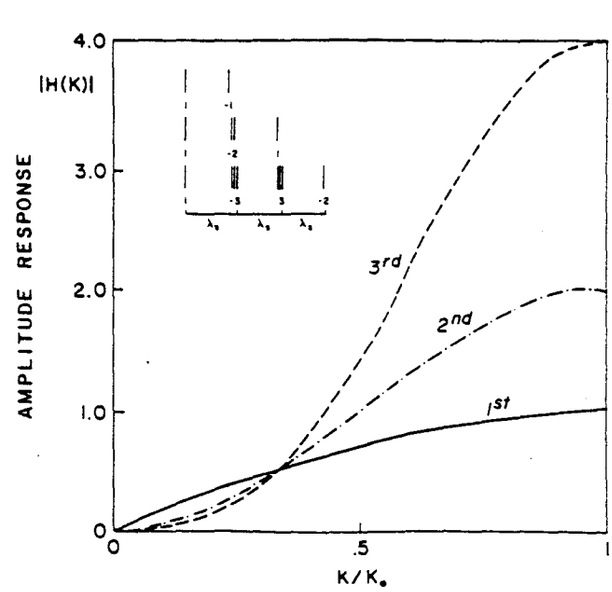

FIG. 2. Amplitude response of first-, second-, and third-order gradiometer in k space ($K_0 = \pi/\lambda_s$).

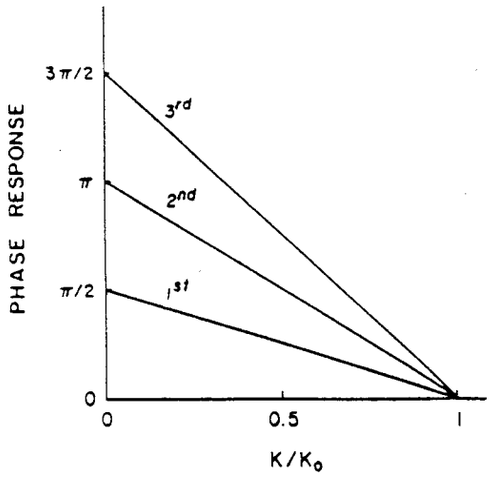

FIG. 3. Spatial phase response of first-, second-, and third-order gradiometers in k space ($K_0 = \pi/\lambda_s$).

shows the calculated phase characteristics for the first-, second-, and third-order gradiometers whose amplitude transfer functions are presented in Fig. 2. These graphs were obtained from the definition of the phase between input and output signals:

$$\phi = \tan^{-1}[\mathrm{Im}\, H(k)/\mathrm{Re}\, H(k)]. \tag{21}$$

Since we are dealing with a spatial frequency response of the system, the phase information leads to a spatial lag between the output signal and the input signal. Indeed, as can be seen in Fig. 3, a gradiometer is a linear phase spatial filter. Such characteristics are important for the evaluation of distortion produced by our filter. The largest phase lag occurs at the frequency where the gain of the system changes the most with respect to frequency. The spatial lag that will occur, especially at low frequencies, can be used to estimate the error introduced by the gradiometer in determining the depth of a current dipole.[6]

SPATIAL FOURIER TRANSFORM OF THE SIGNAL

The noise output of gradiometers of different orders has been discussed above, using the gradiometers' transfer functions and characterizing the noise by their dominant low-order terms in a Taylor expansion. It is important now to discuss the Fourier transform of a given signal from a near source, in order to understand more clearly the meaning of Fig. 2.

The handling of a continuous signal by a digital mathematical formalism is a twofold problem. First, a sampling frequency must be chosen, and second, the infinite sequence generated must be truncated in order to apply the DFT.

Since the sampling frequency must be larger than twice the highest frequency component of the signal (Nyquist theorem),[17,18] we have to estimate the highest frequency component. For the case of magnetic or current dipole, care has to be taken in making such estimates as both are spatially monotonic functions. Certainly, the highest frequency component will be related to the distance from the dipole to the first point of measurement, i.e., first coil position. The DFT is periodic with a period of $2\pi/\lambda_s$. If the sampling frequency chosen is smaller than the Nyquist limit, there will be an overlap between the periodic replicas of the spectrum (aliasing effect).[19]

As to the truncation problem, consider an extreme case where the truncated sequence, representing the spatial dependence of the signal, has only two terms. Assume that the field decreases by a factor Q from the first term to the second term, i.e.,

$$\phi_1 = 1, \phi_2 = (1/Q). \tag{22}$$

The DFT of such a sequence will be

$$\Phi(k) = 1 + (1/Q)e^{-jk\lambda}. \tag{23}$$

Its modulus is

$$|\Phi(k)| = [1 + (1/Q^2) + (1/Q)\cos k\lambda\,]^{1/2}. \tag{24}$$

For a spatially constant field $Q = 1$ (noise),

$$|\Phi(k)| = 2\cos k(\lambda/2), \tag{25}$$

while for a field which decays spatially very fast $Q = \infty$ (the signal),

$$|\Phi(k)| = 1. \tag{26}$$

Those two cases and intermediate ones are shown in Fig. 4.

Hence, if a constant sequence such as the one produced by the noise ($Q = 1$) is defined by only two terms, its DFT is not a delta function as in Eq. (14). Also, if the field decays very fast in space, as would be the case for a signal from a very near source that would be detected just by the pick-up coil ($Q = \infty$), a two-term truncation leads to a constant pattern in the frequency domain. Thus, the truncation can produce as well as the aliasing effect, spurious high frequency components in the spectrum making it difficult to interpret the plots of the filter transfer function (Fig. 2), and the signal and noise frequency spectrum (Fig. 4).

Fortunately the problems of choosing a sampling frequency and the number of terms of Eq. (6) can be avoided because one can have the analytical expression for the spatial dependence of the signal source. Therefore, one can use it to

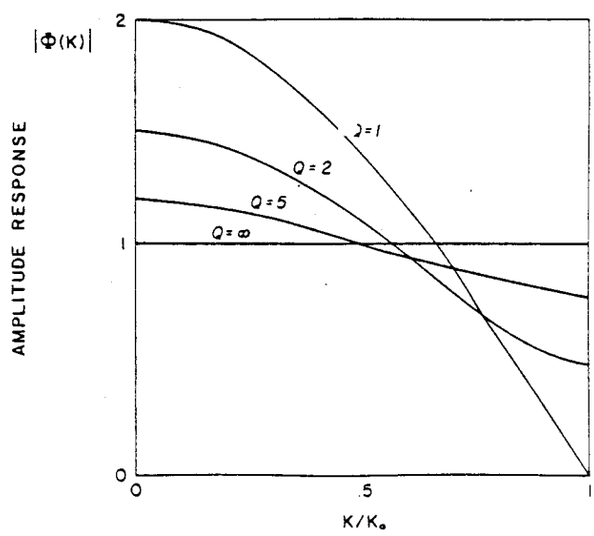

FIG. 4. Amplitude response for a truncated signal with only two terms differing by a factor of Q.

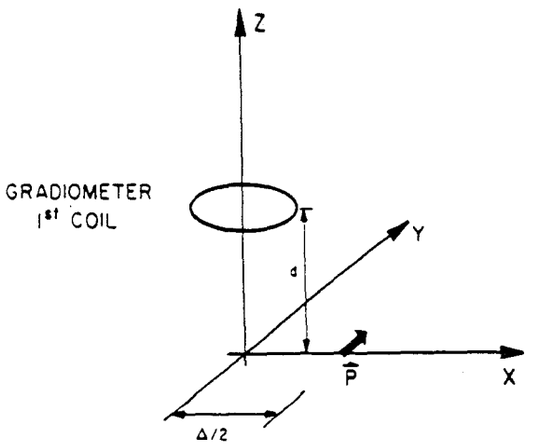

FIG. 5. Parameters used in the calculation of the field produced by a current dipole.

calculate the continuous Fourier transform of the signal. The continuous Fourier transform and the half-period of the DFT are identical for a sampling frequency and number of terms chosen in a proper way.[17]

The analytical spatial dependence of a near source signal, for instance a current dipole, can be obtained by applying the Biot–Savart law in the situation illustrated in Fig. 5. Let us assume that the field is initially measured at the point z_0 in a plane distant d from the current dipole. The current dipole $\mathbf{p}$ is located in the plane xy, oriented in the $+y$ direction,[20] at a distance $x = \Delta/2$ from the z axis, Δ being the distance between field extremes in the $z_0 = d$ plane.

Thus the field can be expressed as

$$B_z(z) = \frac{\mu_0 |\mathbf{p}| d}{4\pi\sqrt{2}} \frac{1}{(d^2/2 + z^2)^{3/2}}. \tag{27}$$

Consequently, one can have the Fourier transform by applying the definition for each spatial frequency k,

$$X(k) = \int_{-\infty}^{\infty} B_z(z) e^{-jkz}\, dk, \tag{28}$$

which can be evaluated numerically.

Now we may determine a maximum frequency of interest in the Fourier transform of the signal, in order to give a visual meaning to Fig. 2. In this case, we may choose k_{max}, so that most of the energy, say 95%, lies inside the frequency range $(0, k_{max})$. In the Fourier series, the sum of $|a_n|^2$ yields the average power.[18] In the Fourier transform, the integration of $|X(k)|^2$ yields the total energy of the signal.[18] We can choose k_{max} using the following criteria:

$$\int_0^{k_{max}} |X(k)|^2\, dk = 0.95 \int_0^{\infty} |X(k)|^2\, dk. \tag{29}$$

The values of the maximum frequency k_{max} determined by Eqs. (27)–(29) are depicted in Fig. 6 as a function of distance d from 3–10 cm. As can be seen one can use approximately π/d as k_{max}.

Finally, one can obtain the first design criteria using this new model. As was said before, the gradiometers' transfer function should be represented in k space up to π/λ_s, where λ_s is the minimum distance between two adjacent coils. Thus if one equals k_{max} to π/λ_s, one can obtain the distance between coils that the gradiometer should have so as to give the signal's maximum detectable energy. The minimum distance between coils as a function of distance d is shown in Fig. 7. It should be stressed that this result is in accordance with the Taylor approach. If a gradiometer is to act as a magnetometer for near sources, the base line should be of at least the order of the distance between the source and the gradiometer.[5,6] It must be remembered, nevertheless, that the final criteria used to choose the gradiometer's base line must also take into account the noise as well. The combination of amplitude response and phase response can be used to determine the amount of distortion introduced by the gradiometer; this distortion will, for example, affect the determination of the depth of the current dipole source and its strength.

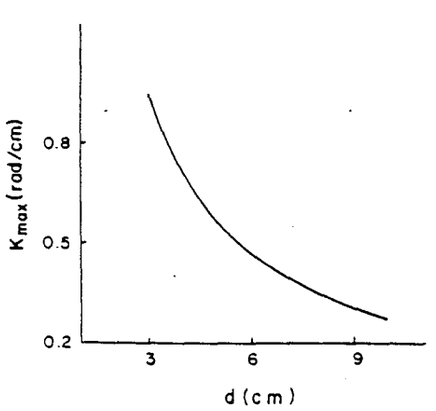

FIG. 6. Spatial frequency limit (K_{max}) as a function of the distance between the current dipole and the gradiometer first coil (d).

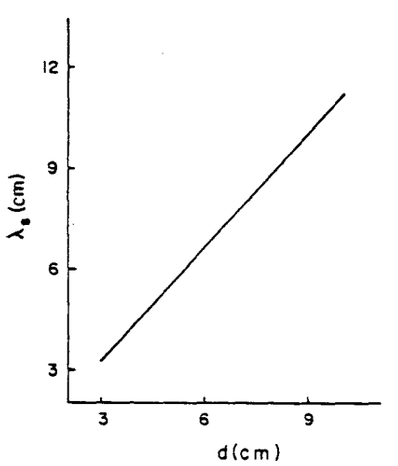

FIG. 7. Minimum distance between two adjacent coils of a gradiometer as a function of the distance between the dipole and the gradiometer first coil (d).

SERVIÇO DE BIBLIOTECA E INFORMAÇÃO - IFQSC
FÍSICA

CONCLUSIONS

This paper presents a novel approach to understanding and designing of gradiometer coils for the detection of weak biomagnetic signals in the presence of noise. The gradiometer is considered as a spatial filter whose characteristics are determined by its transfer function independent of the model used for the source. The transfer function yields the amplitude response and the phase response. The amplitude response gives results in agreement with the Taylor series approach but which are more general; it is a system analysis approach. As an example in the selection of gradiometer characteristics based on the amplitude response of various gradiometers, the spatial Fourier transform of a dipolar signal is presented. Using the approach described in this paper, it will be possible to design gradiometers making trade offs between signal and noise energies for a specific spatial situation of weak magnetic fields and their source localization. The dynamic error[21] introduced by the gradiometer can be estimated by inspection of the amplitude response (Fig. 2) and the phase response (Fig. 3).

ACKNOWLEDGMENTS

We gratefully acknowledge discussions with Professor A. Mesquita. This work was supported by CNPq, Brazil, and the National Science Foundation (International Division).

[1]D. Cohen, E. Edelsack, and J. E. Zimmerman, Appl. Phys. Lett. **16**, 278 (1970).
[2]J. E. Zimmerman and N. V. Frederick, Appl. Phys. Lett. **19**, 16 (1971).
[3]C. D. Tesche, C. C. Chi, C. C. Tsuei, and P. Chandhari, Appl. Phys. Lett. **43**, 384 (1983).
[4]G. B. Donaldson and R. J. P. Bain, Appl. Phys. Lett. **45**, 990 (1984).
[5]J. P. Wikswo, *AIP Conference Proceedings, Future Trends in Superconductor Electronics, Vol. 44* (Am. Inst. Phys., New York, 1978), p. 421.
[6]G. L. Romani, S. J. Williamson, and L. Kaufman, Rev. Sci. Instrum. **53**, 1815 (1982).
[7]D. E. Farrel, J. H. Tripp, R. Norgren, and T. J. Teyler, Electroenceph. Clin. Neurophysiol. **49**, 31 (1980).
[8]S. J. Williamson, D. Brenner, and L. Kaufman, in Ref. 5, p. 106.
[9]S. Barbanera, P. Carelli, R. Fenici, R. Leoni, I. Modena, and G. L. Romani, IEEE Trans. Magn. **MAG-17**, 849 (1981).
[10]J. Vrba, A. A. Fife, M. B. Burbank, H. Weinberg, and P. A. Brickett, Can. J. Phys. **60**, 1060 (1982).
[11]A. C. Bruno and P. Costa Ribeiro, Cryogenics **23**, 346 (1983).
[12]J. R. Storey, Il Nuovo Cimento **2**, 153 (1983).
[13]A. C. Bruno, P. Costa Ribeiro, J. P. von der Weid, and I. R. Eghrari, *Biomagnetism Theory and Applications*, edited by H. Weinberg, G. Stroink, and T. Katila (Pergamon, New York, 1984), p. 67.
[14]G. R. Fowles, *Introduction to Modern Optics* (Holt, Rinehart, and Winston, New York, 1968), p. 139.
[15]T. M. Peters, IEEE Trans. Biomed. Eng. BME-**21**, 214 (1974).
[16]P. Karp and D. Duret, J. Appl. Phys. **51**, 1267 (1980).
[17]M. Schwartz and L. Shaw, *Signal Processing* (McGraw-Hill, Tokyo, Japan, 1975).
[18]T. Chen, *One Dimensional Digital Signal Processing* (Marcel Dekker, New York, 1979).
[19]A. V. Oppenheim and A. S. Willsky, *Signal and Systems* (Prentice Hall, Englewood Cliffs, NJ, 1983).
[20]S. J. Williamson and L. Kaufman, *Biomagnetism*, edited by S. H. Erne, H.-D. Hahlbohm, and H. Lubbig (de Gruyter, Berlin, 1981), p. 335.
[21]J. P. Bentley, *Principles of Measurement Systems* (Longman, London, 1983), p. 61.

ANEXO 4

Spatial Fourier transform method for evaluating SQUID gradiometers

P. Costa Ribeiro, A. C. Bruno, and C. C. Paulsen

Departamento de Fisica, Pontificia Universidade Católica, Rio de Janeiro, RJ, CP 38071, Brazil

O. G. Symko

Department of Physics, University of Utah, Salt Lake City, Utah 84112

(Received 4 March 1987; accepted for publication 27 April 1987)

A simple method of measuring the spatial transfer function of a gradiometer, consisting of a flux transformer coupled to a SQUID, is presented and it is compared with theoretical predictions. Based, on this approach, a new method of reporting a gradiometer's performance is proposed; the rejection factor is expressed in decibels obtained directly from the transfer function plot.

INTRODUCTION

A major problem in the measurement and study of weak biomagnetic fields is the reduction of magnetic noise due to the environment. The most common solution to this is a filtering technique known as spatial discrimination. It essentially consists of connecting a set of coils, which are wound in a gradiometric configuration, to the SQUID input.[1] Usually the gradiometer consists of concentric coils connected in series and separated by distances called base lines.

In the region probed by the gradiometer the spatial distribution of the biomagnetic field and the noise magnetic fields vary monotonically with position. Thus, to study the influence of the gradiometer on the detected signals and its rejection of the noise it is natural to express the corresponding fields in terms of small variations around a given point, namely the position of the first coil of the gradiometer. This is usually done by means of a Taylor series expansion.[2]

A source located far from the gradiometer has a magnetic field spatial variation or distribution that does not vary significantly within the probed region, and hence only a few terms of the Taylor expansion are needed to represent it. However, for fields originating from sources close to the gradiometer, the spatial distribution varies rapidly from point to point within the gradiometer region, and more terms of the polynomial expansion need to be used in order to represent adequately the signal.

A gradiometer of Nth order cancels the first $N-1$ terms of a Taylor expansion.[3] Choosing N properly, the signal of distant sources detected by the SQUID will be drastically attenuated. However, detected signals of near sources should not be attenuated. Unfortunately there is some attenuation of the wanted signal as the net signal detected arises from higher-order terms of the expansion. Thus spatial discrimination is achieved at the price of distorting the signals of interest.

The extent of the distortion introduced in the measurement has been studied by using numerical means but only for a specific source, a single current dipole, and a given second-order gradiometer.[4]

For a general analytical method, a Taylor expansion formalism cannot be used. This is because the near-field sources which are usually located at a distance smaller than the gradiometer's total length would be represented, in this formalism, by a divergent series.[5]

A breakthrough to that problem emerges when it is realized that a monotonic signal can be modeled as well by a Fourier expansion in space.[6] In such an approach, the spatial distribution of a distant source will have only low spatial frequency terms while a near-field source will have both low and high frequency terms. Thus, a properly designed gradiometer will attenuate the low-frequency terms originating primarily from distant sources, and the gradiometer is then basically considered as a high-pass spatial filter.

More precisely, since the magnetic flux is coupled to it at discrete points in space, corresponding to positions of the detection coils, the gradiometer can be regarded as a digital spatial filter. In such an approach, the sampling period is the base line and the samples are weighted according to the number of turns of each coil and its polarity. The advantage of considering the gradiometer as a digital spatial filter comes from the fact that its transfer function can be easily calculated and measured, thus characterizing the gradiometer in a very formal way. With a knowledge of the transfer function of the system a quantitative analysis of the effects of the filter on the signal and noise sources can be made. Therefore, the object of this paper is to demonstrate how the transfer function can be measured and to compare it to the transfer function calculated theoretically. An alternative approach based on the plot of the transfer function will be proposed for evaluating the performance of the gradiometer.

I. EXPERIMENTAL DETERMINATION OF THE TRANSFER FUNCTION

To measure the transfer function of a filter, the gradiometer in the present case, a known signal ϕ is applied to the input of the system and the corresponding output $f(r)$ is recorded as a function of the space coordinate r. The Fourier transform of the output signal $F(k)$, where k is the spatial frequency, divided by the Fourier transform of the input signal $\phi(k)$ is then by definition equal to the measured transfer function of the system

$$H_m(k) = F(k)/\phi(k) . \quad (1)$$

 0034-6748/87/081510-04$01.30 © 1987 American Institute of Physics

The magnitude of $H_m(k)$ may then be compared to the magnitude of the theoretical transfer function $H_t(k)$ obtained by taking the discrete Fourier transform of the filter coefficients

$$H_t(k) = \sum_{i=0}^{N} n_i e^{-jkb_i}, \tag{2}$$

where n_i is the number of turns (with proper polarity) of each gradiometer coil at position i, b_i is the common distance between the coils, and $N+1$ is the total number of coils.

As in all systems an input and an output must be defined. The output of the gradiometer is clearly the sum of signals seen by the various coils. The input is considered to be the signal which couples to only one coil, as the aim is to measure the magnetic field at particular points in space.

When measuring the response of the more conventional temporal filter (as opposed to the present spatial filter), the input signals are usually at fixed frequencies or they can be pulses. Unfortunately it is not a straightforward task to create a spatially monochromatic signal and it is even more difficult to get a spatial magnetic pulse. However, any known signal (i.e., a signal whose Fourier transform is known and well behaved) will suffice as the input. Thus the known signal is simply the spatial distribution of the magnetic field generated by a single turn coil.

The dimensions of such a coil were chosen according to the following requirements and criteria. The coil radius should be large enough to allow it to slip over the Dewar and also to make the measurements less sensitive to its positioning, but the coil should be small enough to produce a spatial field distribution which is well behaved for a Fourier transform processing.[8] A computer simulation was done to find a suitable radius and a good compromise was reached for a radius of 15 cm.

An apparatus was constructed which held the coil fixed with respect to the x–y plane, but allowed the movement along the z axis. The Dewar containing the gradiometer was placed on a high stand concentric with respect to the signal coil axis. The coil could then be slipped over the stand and Dewar from a position approximately 1.2 m below the pickup coil (six times the gradiometer base line) to a comparable position above. A low-frequency current (17 Hz) was applied to the coil, and the resulting signal from the SQUID was detected by a lock-in amplifier. The coil was moved by increments of 5 cm when far from the gradiometer, and by 2.5 or 1.0 cm when near it. The gradiometer used in this test was a third-order design whose total length was 20.0 cm.[9]

II. EXPERIMENTAL RESULTS

The theoretical spatial distribution of the magnetic field of the test coil was used as the input. Its variation as a function of the axial distance can be seen in Fig. 1(a), where the origin is taken at the center of the gradiometer. The corresponding Fourier transform is shown in Fig. 1(b). The limiting frequency for the Fourier plot was chosen in such a way that most of the relevant spatial frequency components of a current dipole placed at 7 cm below the gradiometer are present up to this frequency.[10] The output of the third-order gradiometer due to a signal in the test coil at various points in space is presented in Fig. 2(a). A spline interpolation technique was used to generate a function appropriate for a Fourier transform process, which then leads to the Fourier transform shown in Fig. 2(b).

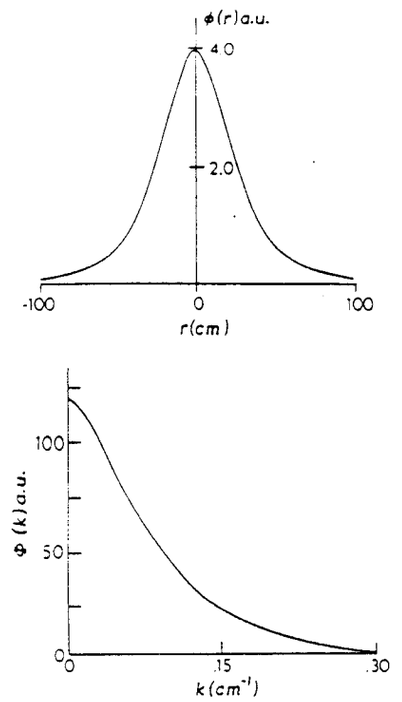

FIG. 1. (a) Magnetic field ϕ generated by the test coil as a function of the axial distance r. (b) Fourier transform of $\phi(r)$ in k space.

The gradiometer transfer function is obtained by dividing the Fourier transform of the output by the Fourier trans-

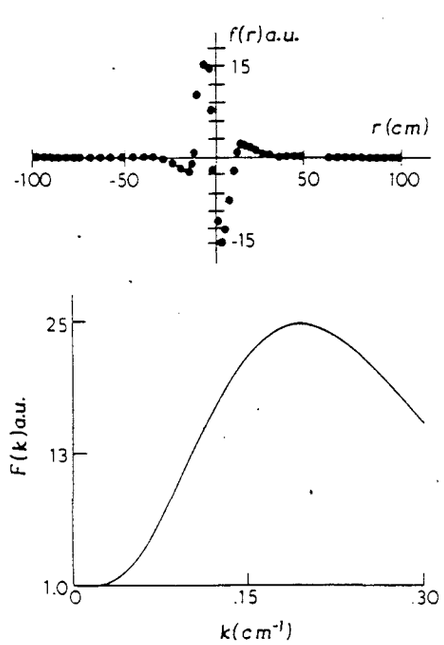

FIG. 2. (a) Measured output from the gradiometer $f(r)$ for various positions r of the test coil. (b) Fourier transform of $f(r)$ in k space.

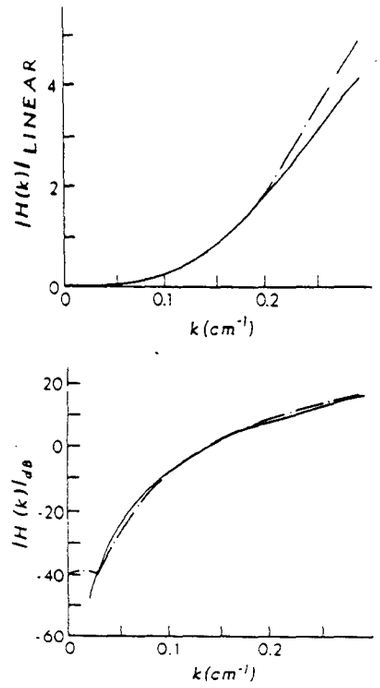

FIG. 3. (a) Theoretical (continuous line) transfer function for a third order gradiometer, and actual (dashed line) transfer function for third-order gradiometer on a linear scale. (b) Graph of (a) on a decibel scale.

form of the input as in Eq. (1). This is shown in Fig. 3(a) on a linear scale and in Fig. 3(b) on a decibel scale, where the dashed curve is the magnitude of the measured transfer function obtained by the experimental procedure described above, and the solid curve is the magnitude of the theoretical transfer function obtained by substituting in Eq. (2) the number of turns and the base line of the third-order gradiometer used. As is shown in the decibel scale plot, the real and theoretical curves are essentially the same for spatial frequencies from approximately 0.09 to 0.19 cm^{-1}. For frequencies higher than 0.19 cm^{-1} there are differences because of the integrating effect of the gradiometer loops which was not taken into account for the input calculation. It should be emphasized that, as expected, this effect appears only at high frequencies. For frequencies below 0.09 cm^{-1} the difference is due to the unbalance of the real gradiometer.

III. UNBALANCE AND TRANSFER FUNCTION

The design conditions for a Nth order gradiometer in the Taylor expansion approach,

$$\sum_{i=0}^{N} \frac{n_i b_i^{\alpha}}{\alpha!} = 0, \quad \alpha = 0,\ldots, N-1, \tag{3}$$

have been shown[10] to be equivalent, in the Fourier approach, to

$$\frac{d^{\alpha}}{dk^{\alpha}} H(k)\bigg|_{k=0} = 0, \quad \alpha = 0,\ldots, N-1, \tag{4}$$

where $H(k)$ is the transfer function of the gradiometer. However in practice conditions (3) or (4) cannot be really achieved. Hence we define a way to measure how perfect is the built gradiometer.[2,11] The so-called unbalance is a measure of how far from zero are the design conditions. Specifically, the uniform field rejection is according to the condition in Eq. (3)

$$\sum_{i=0}^{N} n_i = 0, \tag{5}$$

which is equivalent[10] in the Fourier approach to $H(0)$. The zeroth-order balance of the gradiometer may be then easily obtained from the magnitude of the measured transfer function curve at zero spatial frequency. Also the field gradient rejection according to Eq. (3) is

$$\sum_{i=0}^{N} n_i b_i = 0, \tag{6}$$

which is equivalent in the Fourier approach to making α equal to 1 in Eq. (4). By taking the first derivative of the measured transfer function at the same frequency, the first order unbalance can be found.

The transfer function value for the empirical plot at zero spatial frequency is 8.7×10^{-3}. As discussed earlier this value corresponds to the field balance of the gradiometer. To check this, a field balance measurement was done with a modified set of square coils,[12] based on the Rubens design with 80.0 cm for each side, where the measured uniformity was better than 5.0×10^{-5} over a cube of 20.0 cm^3. A value of 8.4×10^{-3} was obtained for the unbalance measurement, which is very near to the above value of 8.7×10^{-3}.

At this point, we would like to propose a new method of presenting the gradiometer's performance. The magnitude of the transfer function at zero spatial frequency is -41.2 on a decibel scale. Thus, instead of reporting the gradiometer's performance in terms of a percentage error in the loop areas, the performance could be described by its rejection in decibels for that spatial frequency. Concerning the gradient unbalance, the value obtained for it from a numerical calculation was 0.19. This aspect of the performance could be referred to simply as a rejection of -14.4 dB at constant gradients for a third order gradiometer. This method of specifying the performance makes it easier to compare gradiometers between various groups; it also clearly shows that a gradiometer is truly a spatial high-pass filter. This formalism makes the problem, of measuring biomagnetic signals in the presence of noise, a question of system analysis dealing with noise, filters, and bandwidth.

ACKNOWLEDGMENTS

This work was supported jointly by CNPq, FINEP, Brazil, and the National Science Foundation (International Division), USA.

[1] J. E. Zimmerman and N. V. Frederick, Appl. Phys. Lett. 18, 16 (1971).
[2] J. E. Opfer, Y. K. Yeo, J. M. Pierce, and L. H. Rorden, IEEE Trans. Magn. MAG-9, 536 (1974).
[3] P. Karp and D. Duret, J. Appl. Phys. 51, 1267 (1980).
[4] G. L. Romani, S. J. Williamson, and L. Kaufman, Rev. Sci. Instrum. 53, 1815 (1982).
[5] A. C. Bruno and P. Costa Ribeiro, Rev. Bras. Eng. 2, 21 (1984).
[6] A. C. Bruno, P. Costa Ribeiro, J. P. von der Weid, and I. R. Eghrari,

Biomagnetism: Applications and Theory, edited by H. Weinberg, G. Stroink, and T. Katila (Pergamon, New York, 1984), p. 67.
[7]M. Schwartz and L. Shaw, *Signal Processing* (McGraw-Hill, Tokyo, 1975).
[8]T. Chen, *One Dimensional Digital Signal Processing* (Dekker, New York, 1979).
[9]A. C. Bruno and P. Costa Ribeiro, Cryogenics **23**, 324 (1983).
[10]A. C. Bruno, P. Costa Ribeiro, J. P. von der Weid, and O. G. Symko, J. Appl. Phys. **59**, 2584 (1986).
[11]J. Vrba, A. A. Fife, M. B. Burbank, H. Weinberg, and P. A. Brickett, Can. J. Phys. **60**, 1060 (1982).
[12]R. Merrit, C. Purcell, and G. Stroink, Rev. Sci. Instrum. **54**, 879 (1983).

ANEXO 5

Digital filter design approach for SQUID gradiometers

A. C. Bruno and P. Costa Ribeiro
Departamento de Fisica, Pontificia Universidade Católica do Rio de Janeiro, C.P. 38071, 22453 Rio de Janeiro RJ, Brasil

(Received 17 April 1987; accepted for publication 16 November 1987)

A review of the traditional method for designing gradiometers is made. A nonrecursive digital filter model for the gradiometer is presented, giving a new set of parameters for the gradiometer identification. Some designs are analyzed using the proposed set. As an example, a true differentiator is designed to be used as the SQUID input coil. It is shown that the differentiator has the same noise rejection as the conventional gradiometer but provides more signal sensitivity.

I. INTRODUCTION

In the late sixties, the appearance of the SQUID was the most important fact for the development of biomagnetic measurements, which are being made in several research institutes and hospitals. The SQUID is usually coupled to a superconducting circuit called a flux transformer. It consists of a set of coils for field sensing, connected in series with a solenoid placed inside the SQUID body. When a magnetic field is applied to the coils, a persistent current appears in the circuit, producing a magnetic flux inside the SQUID.

Usually the measurements are made in environments that have magnetic interference from power lines, motors, elevators, etc. These fields have magnitudes that surpass biomagnetic fields by a factor of at least 10 000. Some filtering procedure must be used in order to remove the unwanted noise. A possible solution is to place the patient and instrument of measurement inside a magnetically shielded chamber. Another technique is to use the set of coils coupled to the SQUID, in a gradiometric configuration,[1] to make a spatial discrimination between signal and noise. This occurs because the noise source is very far from the gradiometer and the weak source is placed close to it. The monotonic spatial decay of the noise can be modeled by low-order terms of a Taylor series expansion. As the gradiometer cancels the first derivatives the far source field will not be detected.

This paper makes a review of the gradiometer analysis and design process. It is a more formal and general approach of a formalism than introduced previously,[2] showing that the gradiometer is a digital spatial filter. The gradiometer design is discussed using conventional filter analysis parameters. These parameters can be used to describe the gradiometer design instead of its geometrical description. Finally, using this formalism, first- and second-order differentiators are designed to be used as the SQUID input coil. The differentiators will theoretically have the same noise rejection but a better signal sensitivity.

II. REVIEW ON THE DESIGN OF GRADIOMETERS

The equation that describes the total flux $\phi(z_0,t)$ through a set of coils axially positioned along the z axis, the first coil being at z_0, can be stated as

$$\phi(z_0,t) = A\left(\sum_{i=0}^{N} n_i B_z(z_i)\right) f(t), \tag{1}$$

where A is the area of coils, n_i is the number of turns of each coil, $B_z(i)$ is the normal component of the magnetic field at the coil i, $N+1$ is the number of coils, and $f(t)$ is the time dependence of the field. Expanding $B_z(z)$ in Taylor series around the origin (z_0) yields

$$B_z(z) = \sum_{\alpha=0}^{\infty} \frac{B_z^{(\alpha)}(z_0)}{\alpha!}(z-z_0)^{\alpha}, \tag{2}$$

where $B_z^{(\alpha)}(z_0)$ is the derivative of order α of the field $B_z(z)$ at z_0. Substituting (2) in (1), considering only spatial dependence, the flux through the set of coils can be expressed in terms of the field and its derivatives at the first coil:

$$\phi(z_0) = A\left(\sum_{i=0}^{N}\sum_{\alpha=0}^{\infty} n_i \frac{B_z^{(\alpha)}(z_0)}{\alpha!}(z_i-z_0)^{\alpha}\right). \tag{3}$$

To design an Nth-order gradiometer, the first N terms of (3) must be made equal to zero to reject the noise. Then, the following system of equations is obtained[3]:

$$\sum_{i=0}^{N} n_i \frac{b_i^{\alpha}}{\alpha!} = 0, \quad \alpha = 0,1,\ldots,N-1, \tag{4}$$

where $b_i = z_i - z_0$ is the distance between the ith coil and the lower one. The gradiometer parameters are obtained by solving system (4). From visual inspection one can see that (4) is a system that has N equations and $2N+1$ unknowns. In order to solve it, $N+1$ unknowns must be transformed in parameters of the system. According to the unknowns transformed, two kinds of solutions will arise. For instance, suppose that the Nb_i's $(b_1, b_2 = 2b_1, \ldots, b_N = Nb_1)$ and one $n_i(n_0)$ are chosen. In this case the solution for the system will be given by the Newton binomial formula[4]:

$$n_i = n_0(-1)^{i-1}C_{i-1}^{N}, \quad i = 1,\ldots,N-1. \tag{5}$$

This solution leads to the conventional gradiometer design. However, if the $N+1$ n_i's are chosen, one will have the first equation solved, so one more unknown must be chosen. Suppose that the one chosen is the total length of the gradiometer b_N. As was shown,[5] this is the most general choice for solving system (4), and will lead to solutions where the b_i's are not multiples of the smaller ones.

The gradiometer output signal will be proportional to the field derivative only for distant signal sources. Only if the source is at a distance much larger than the gradiometer total length will series (3) converge.[6]

 0021-8979/88/082820-04$02.40 © 1988 American Institute of Physics

III. DIGITAL FILTER MODELING

As was said elsewhere,[2] the gradiometer is a device that samples the signal and noise at discrete points in space, that correspond to the coil positions; thus, it is a spatial digital sampler. The sampling period λ_s is given by the minimum distance between the coils. Moreover, the gradiometer makes a weighted sum of the input field sampled sequence. The weighting factors depend on the area of each coil. The gradiometer is a nonrecursive digital spatial filter. This can be illustrated with the following arguments: the basic digital filter elements are the unit delay, the adder, and the multiplier.[7] Therefore, digital filters are collections of interconnected unit delays, adders, and multipliers. A gradiometer has in its hardware the elements that correspond to those three basic elements of the digital filter theory. The sampling period λ_s corresponds to the unit delay. The fact that all the coils are wound in series corresponds to the adder. Finally, the area of each coil corresponds to the multiplier. All the formalism already developed for digital filters can then be used to analyze and design gradiometers. Assuming a symmetric design (all coils with the same area), the gradiometer spatial transfer function $H(k)$ can be obtained by taking the discrete Fourier transform of the sequence that represents the number of turns of each coil[2]:

$$H(k) = A \sum_{i=0}^{N} n_i e^{-jk\lambda_i}, \tag{6}$$

k being the spatial frequency.

In that approach signal and noise will be described by the spatial Fourier spectra. In doing so, the noise will have a spectrum with low frequencies and the signal will be represented by a much wider spectrum.[8] Using the digital filter modeling, a gradiometer spatial transfer function could be designed for each noise and signal specification.

IV. GRADIOMETER DESIGN WITH A FILTERING TECHNIQUE

It can be seen below how the traditional gradiometer configuration arises when a digital filter design procedure is used for a high-pass transfer function. One condition that guarantees the effectiveness of a smooth high-pass filter is

$$\left.\frac{d^\alpha H(k)}{dk^\alpha}\right|_{k=0} = 0, \quad \alpha = 0,1,\ldots,N-1, \tag{7}$$

where N is the order of the filter. Equation (7) shows that the stop-band flatness of a high-pass transfer function increases when the order of the filter increases.

A method for synthesizing a digital filter is to find the proper transfer function, $H(s)$, in Laplace space using the classical filter theory. The analog design is then transformed on a digital realization. A possible design having *pass*-band flat is known as Butterworth.[9] However, condition (7) requires that the *stop*-band be flat. Nevertheless, the Butterworth polynomial $H_b(s)$ can be used to make the desired transfer function $H_g(s)$ in the following way:

$$H_g(s) = 1 - 1/H_b(s). \tag{8}$$

If denormalized, $H_b(s)$ can be written as

$$H_b(s) = 1/(1 - s^N). \tag{9}$$

Substitution of (9) in (8) will lead to

$$H_g(s) = s^N. \tag{10}$$

This will ensure a maximally flat stop-band transfer function fulfilling condition (7).

The gradiometer realization of (10) can be made by using one of the transforms from the Laplace space to the digital space. It consists in replacing the differential equation related to $H_g(s)$ with a difference equation.[10] This can be done by making the following substitution of variables:

$$s = 1 - z^{-1}, \tag{11}$$

where z is the variable in the digital domain ($z = e^{jk\lambda_s}$).

Then, $H(z)$ can be written as

$$H(z) = (1 - z^{-1})^N. \tag{12}$$

For $N = 1$,

$$H(z) = 1 - z^{-1}; \tag{13}$$

for $N = 2$,

$$H(z) = 1 - 2z^{-1} + z^{-2}; \tag{14}$$

for $N = 3$,

$$H(z) = 1 - 3z^{-1} + 3z^{-2} - z^{-3}; \tag{15}$$

for $N = 4$,

$$H(z) = 1 - 4z^{-1} + 6z^{-2} - 4z^{-3} + z^{-4}; \tag{16}$$

and so on.

The gradiometer corresponds to a direct canonic realization of the above transfer function,[7] where the canonic means number of base lines equal to the transfer function order. For instance, transfer function (15) shows that "1" stands for the first coil with one turn, "$-3z^{-1}$" means that after one λ_s there is a coil with three turns in the opposite direction, "$3z^{-2}$" means that after two λ_s there is a coil with three turns in the same direction as the first one, and finally "$-z^{-3}$" means that after three λ_s from the beginning of the gradiometer there is a coil with one turn in the opposite direction. The magnitude of the transfer function (12) expressed in decibels is

$$|H(z)| = 20 \log[2^N \sin^N(k\lambda_s/2)]. \tag{17}$$

Usually, the magnitude of the filter transfer function plot is divided in three parts: stop band, transition band, and pass band. The stop band is usually evaluated by the maximum rejection given by the filter. In our case, this is equivalent to the gradiometer balance reached.[11] The transition band is measured in terms of rolloff per decade of frequency and the pass band by the cutoff frequency and maximum gain. If the gradiometer is balanced up to 10^{-4}, the maximum rejection achieved will be -80 dB at $K = 0$. Assuming $k\lambda_s/2 \ll 1$ in the transition band, one can have

$$\text{rolloff} = -20\ N \text{ dB/decade}. \tag{18}$$

The cutoff frequency can be expressed as

$$k_c = (2/\lambda_s)\sin^{-1}[(0.707)^{1/N}]. \tag{19}$$

Finally, the maximum gain is

$$H(k_m) = 20 \log(2^N), \tag{20}$$

where $k_m = \pi/\lambda_s$,[7] as the gradiometer is a digital spatial filter.

TABLE I. Filter parameters to first- (see Ref. 12), second- (a) (see Ref. 13), second- (b) (see Ref. 14), and third- (see Ref. 15) order gradiometers.

Gradiometer designs	Rolloff (dB/decade)	k_c (cm^{-1})	k_m (cm^{-1})	$H(k_m)$ (dB)
first	−20	0.15	0.31	6
second (a)	−40	0.4	0.62	12
second (b)	−40	0.62	0.98	12
third	−60	0.4	0.57	18

Table I shows the set of parameters of first-, second-, and third-order gradiometers. The gradiometer maximum rejection does not depend on the design, so it is not listed in the table. The maximum gain of the pass band and the rolloff per decade of frequency depends only on the order of the gradiometer. As the order increases both parameters will increase. In doing so, the transfer function will become sharper because the rolloff will increase. The maximum gain will be at different spatial frequencies for gradiometers of the same order with different baselines. The frequency for maximum gain depends only on the baseline, i.e., a large baseline will lead to a small k_m. Finally, the cutoff frequency depends on the order and baseline. If the order increases k_c will increase; however, if the baseline increases k_c will decrease.

The shape of the spatial frequency spectrum depends on the source position. For instance, a superficial brain source will have a spectrum wider than a heart source.[8] Hence, a large k_c (short baseline) shall be used to detect a brain source. However, the gradiometer design will always be a tradeoff between its $H(k_m)$, rolloff, and k_c.

V. DESIGN OF A DIGITAL SPATIAL DIFFERENTIATOR

Another method for designing a digital filter is to obtain the filter coefficients from the Fourier series representation, as shown below. The transfer function of a nonrecursive digital weighted sampler is:[16]

$$H(k) = \sum_{n=-\infty}^{\infty} h_n e^{-jkn\lambda_s}. \tag{21}$$

The filter coefficient h_n should in general be considered the gradiometer loop areas and can be obtained by taking the inverse Fourier transform of $H(k)$:

$$h_n = \frac{\lambda_s}{2\pi}\int_{-\pi/\lambda_s}^{\pi/\lambda_s} H(k)e^{jkn\lambda_s}\,dk. \tag{22}$$

As an example, we describe the design of a digital differentiator. The differentiation corresponds, in the frequency domain, to the multiplication of the Fourier transform of the input by the factor jk. The characteristic of an ideal digital differentiator is given by

$$H(k) = jk, \quad \text{for} \quad -\pi/\lambda_s < k < \pi/\lambda_s. \tag{23}$$

The filter coefficients h_n can be obtained substituting (23) in (22), and truncating the resulting series:

$$h_n = \frac{\lambda_s}{2\pi}\int_{-\pi/\lambda_s}^{\pi/\lambda_s} (jk)e^{jkn\lambda_s}\,dk, \tag{24a}$$

$$= \frac{(-1)^n}{n\lambda_s}, \quad \text{for} \quad n = -N \text{ to } N, \tag{24b}$$

and $h_n = 0$ for $n = 0$.

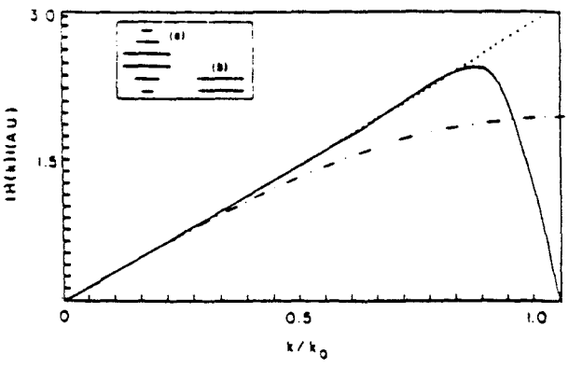

FIG. 1. Transfer functions in K space ($k_0 = \pi/\lambda_s$) of an ideal differentiator (dotted line), a digital realization of it (continuous line) with $N = 3$ (six coils), and a conventional first-order gradiometer (dash-dotted line) with the same sampling period. (a) The differentiator and (b) the gradiometer are represented in the inset.

The direct truncation of this antisymmetric sequence will result in a spatial filter with a quite oscillatory transfer function. The ripples can be virtually eliminated by using a windowing technique to truncate the sequence of the spatial filter coefficients (coil area). For instance, the Hamming window is given by the following expression[17]:

$$w_n = 0.54 + 0.46\cos(n\pi/N), \quad \text{for} \quad n = 0 \text{ to } N. \tag{25}$$

Windowing consists of multiplying the window factors w_n with the coefficients h_n. The new filter coefficients will be a smoothly decreasing series. Such a differentiator would have a nearly conical shape, since successive coils would have less area.

As shown in Fig. 1, the transfer function for a digital differentiator (continuous line), using $N = 3$ (six coils) and a Hamming window, is quite satisfactory when compared to the one of an ideal differentiator (dotted line). It can also be noticed in Fig. 1 that the first-order gradiometer (dash-dotted line) acts for low frequencies as a differentiator. As noise sources have only low-frequency Fourier components, a differentiator has the same rejection for them as a first-order gradiometer with the same sampling period. Moreover, it is important to stress that with the differentiator, not only the noise but the near source field will be differentiated.

If more noise rejection is required, a second-order differentiator can be designed in the same way. In doing so, the filter coefficients (coils' areas) will be the following:

$$h_0 = -\pi^2/(3\lambda_s^2) \tag{26}$$

and

$$h_n = -2[(-1)^n/(n\lambda_s)^2], \quad \text{for} \quad n = -N \text{ to } N. \tag{27}$$

The transfer function of this second-order spatial differentiator using the same Hamming window with $N = 10$ (20 coils) and a conventional second-order gradiometer with the same sampling period, as shown in Fig. 2. Also shown in Fig. 2 is the normalized magnitude of the Fourier transforms $|B(k)|$ of a current and magnetic dipole placed, respectively, at λ_s and $50\lambda_s$ from the position of the first coil. As can be seen, the differentiator will provide a better signal-to-noise ratio, since it has more sensitivity for high-frequency terms of the Fourier spectrum which constitutes the main signal of interest.

SERVIÇO DE BIBLIOTECA E INFORMAÇÃO - IFQSC
FÍSICA

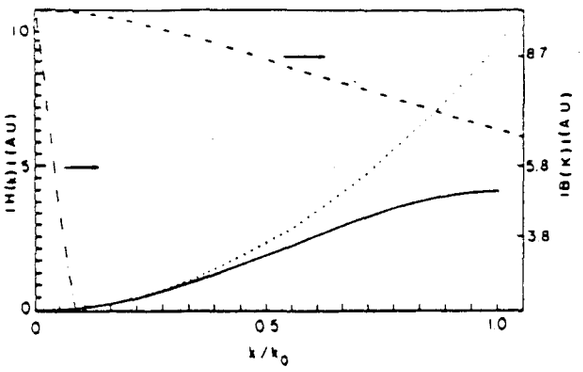

FIG. 2. Transfer functions in K space ($k_0 = \pi/\lambda_s$) of a second-order gradiometer (continuous line) and a second-order differentiator (dotted line), with the same sampling period. Normalized magnitudes of the Fourier transforms of a near current dipole (dashed line) and far magnetic dipole (dash-dotted line) sources.

VI. CONCLUSION

A review on the traditional gradiometer design process was made. A complete equivalence of a gradiometer and a nonrecursive digital spatial filter was shown, providing a new method for synthesizing the conventional gradiometer configurations. In addition to that, instead of a simple geometric description, a set of parameters based on the filter theory was proposed as a new way of reporting the gradiometer design. Finally, using digital design techniques, digital spatial differentiators are designed and the transfer function is compared to the one of conventional gradiometers.

ACKNOWLEDGMENTS

This work was partially supported by FINEP, CAPES, and CNPq.

[1] J. E. Zimmerman and N. V. Frederick, Appl. Phys. Lett. 19, 16 (1971).
[2] A. C. Bruno, P. Costa Ribeiro, J. P. von der Weid, and I. R. Eghrari, in *Biomagnetism: Applications and Theory*, edited by H. Weinberg, G. Stroink, and T. Katila (Pergamon, New York, 1984), p. 67.
[3] P. Karp and D. Duret, J. Appl. Phys. 51, 1267 (1980).
[4] G. L. Romani, S. J. Williamson, and L. Kaufman, Rev. Sci. Instrum. 53, 1815 (1982).
[5] A. C. Bruno and P. Costa Ribeiro, Cryogenics 23, 346 (1983).
[6] A. C. Bruno and P. Costa Ribeiro, Rev. Bras. Eng. 2, 21 (1984).
[7] A. Antoniou, *Digital Filters: Analysis and Design* (McGraw-Hill, New York, 1979).
[8] A. C. Bruno, P. Costa Ribeiro, J. P. von der Weid, and O. G. Symko, J. Appl. Phys. 59, 2584 (1986).
[9] J. K. Skwirzynski, *Design Theory and Data for Electronic Filters* (Van Nostrand, London, 1965).
[10] A. V. Oppenheim and R. W. Schafer, *Digital Signal Processing* (Prentice-Hall, New Jersey, 1975).
[11] P. Costa Ribeiro, A. C. Bruno, C. C. Paulsen, and O. G. Symko, in Rev. Sci. Instrum. 58, 1510 (1987).
[12] M. Saarinen, P. Siltanen, P. J. Karp, and T. E. Katila, Ann. Clin. Res. 10, 1 (1978).
[13] S. Barbanera, P. Careli, R. Fenici, R. Leoni, I. Modena, and G. L. Romani, IEEE Trans. Magn. MAG-7, 849 (1981).
[14] S. I. Williamson, D. Brenner, and L. Kaufman, AIP Conf. Proc. 44, 106 (1978).
[15] J. Vrba, A. A. Fife, M. B. Burbak, H. Weinberg, and P. A. Brickett, Can. J. Phys. 60, 1060 (1982).
[16] M. Schwartz and L. Shaw, *Signal Processing* (McGraw-Hill, Tokyo, 1975).
[17] C. T. Chen, *One Dimensional Digital Signal Processing* (Marcel Dekker, New York, 1979).

ANEXO 6

Discrete spatial filtering with SQUID gradiometers in biomagnetism

A. C. Bruno, P. Costa Ribeiro, and J. P. von der Weid
Department of Physics, Pontificia Universidade Catolica, Rio de Janeiro, Brazil

O. G. Symko
Department of Physics, University of Utah, Salt Lake City, Utah 84112

(Received 4 April 1985; accepted for publication 6 December 1985)

First-, second-, and third-order gradiometers used in detecting biomagnetic signals are analyzed as spatial filters. Their transfer functions independent of the source to be measured are presented and both the magnitude and phase characteristics of the transfer functions are analyzed. The distortion introduced by the gradiometer can be estimated from these characteristics. In order to treat the signal in that approach, the spatial Fourier transform of a magnetic signal produced by a current dipole at a given distance is discussed.

INTRODUCTION

For a number of years SQUID magnetic sensors[1] have been used in biomagnetism research and have been instrumental in significant achievements in the field. Usually the signal is coupled to the sensor by a flux transformer which has the detection coil in a gradiometer configuration for spatial discrimination between signal and noise.[2] This technique is also used in other fields of research involved in the detection of relatively weak magnetic fields, the monopole search being one of them.[3,4]

A gradiometer can be basically described as an array of coils, the lowest one, called the "pick-up" coil or "face loop,"[5] being primarily sensitive to the near source of signal and the others acting as "compensating coils" to eliminate the far sources of noise. Such a simplification has to be abandoned when a quantitative result is needed, as in the case for the localization of brain sources; the influence of the "compensating coils" on the signal should then be taken into account.[6]

Usually each laboratory working on biomagnetism has its own gradiometer, described as being of first,[7] second,[8,9] or third order[10,11] with given distances between coils, number of turns, and area of each coil. The choice for the actual values of these parameters has been rather qualitatively dictated by the kind of local background noise and signal to be measured. Usually in a comparison of coils, the assessment is based on noise level achieved by these different systems and is presented as a value in $\mathrm{fT}/\sqrt{\mathrm{Hz}}$ for the equivalent field spectral density or power spectrum of the noise in the pick-up coil.

With such an approach it is difficult to know the exact noise rejection of each system (the actual background noise is not known), thus making it difficult to compare them. Also, if the source is not just a current dipole (as is the case of the heart), the signal spatial dependence is not known. Such shortcomings have been partially overcome by the approach of Wikswo[5] and Storey.[12] They used the reciprocity principle to make a comparison between different gradiometer designs for noise rejection in the presence of magnetic dipole sources only. The sensitivity of various gradiometer configurations to only current dipole sources has also been calculated.[5]

We present a more general approach[13] to this problem by describing analytically the gradiometer in terms of its transfer function irrespective of the kinds of signal or noise. Our approach is such that gradiometers are high-pass discrete spatial filters whose transfer function enables a comparison to be made between the different gradiometer configurations. Such transfer functions will help to select the best design for a given signal and noise, as well as to determine the effect of the "compensating coils" on the signal.

The fundamental idea in the use of gradiometers to discriminate the signal from the noise is that in a given region of space, the spatial magnetic field dependence can be fitted by a polynomial (Taylor series). Far sources (noise in our applications) are fitted to only one to three terms of the polynomial, since just the field and its first derivatives are predominant, while near sources (the signal in our case) will require a larger number of terms. A gradiometer makes the spatial discrimination by canceling the first terms of the polynomial.

Although it is not customary procedure, the monotonic magnetic field spatial dependence can be fitted just as well by a Fourier expansion. In such an approach, spatial discrimination is reached by using the fact that a distant source will have low frequency components of its *spatial* frequency spectrum, while near sources will have low and high frequency components. The spatial discrimination is then achieved by using a spatial high-pass filter.

The use of spatial filters is well known in other fields, such as optics[14] or tomography,[15] and can be instructive and useful to apply to magnetic field studies in biophysics. This is the goal of this paper. The gradiometer is presented as a nonrecursive spatial filter with its own transfer function; then this approach is compared to the conventional Taylor series approach. Finally, the spatial Fourier transform of the signal is considered, to show how the various gradiometers (i.e., filters) will respond to it.

THE GRADIOMETER SENSOR: A TAYLOR SERIES APPROACH

The general configuration of an Nth order gradiometer is shown in Fig. 1. It consists of an array of $N+1$ coils connected in series, each with n_i turns, and separated by the

 0021-8979/86/072584-06$02.40 © 1986 American Institute of Physics

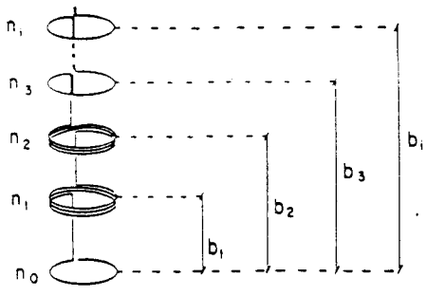

FIG. 1. Gradiometer of Nth order.

distance b_i from the lowest coil. For simplicity, we consider the case where they all have the same area A. The equations that characterize such a gradiometer are derived by considering the total flux $\phi(z_0,t)$ applied to the array, with the lowest coil at z_0 from the source,

$$\phi(z_0,t) = f(z_0)g(t) = A\left(\sum_{i=0}^{N} n_i B(z_i)\right)g(t), \tag{1}$$

where $B(z_i)$ is the magnetic field component normal to the plane of the coil, z_i is the distance from the ith coil to the origin, and $g(t)$ is the time dependence of the flux, expressed separately since biomagnetic fields are quasistatic.

Expanding $B(z)$ in a Taylor series about the position z_0 of the lowest coil and letting $b_i = z_i - z_0$, Eq. (1) can be written as

$$\phi_{\text{total}}(z_0,t) = A\{n_0 B(z_0) + n_1[B(z_0) + B^{(1)}(z_0)b_1 + B^{(2)}(z_0)(b_1^2/2) + \cdots] + n_2[B(z_0) + B^{(1)}(z_0)b_2 + B^{(2)}(z_0)(b_2^2/2) + \cdots] + \cdots\}g(t). \tag{2}$$

This can be arranged in matrix form as

$$\phi_{\text{total}}(z_0,t) = A\,[111\ldots]\begin{bmatrix} n_0 + n_1 + n_2 + \cdots & & & 0 \\ & n_1 b_1 + n_2 b_2 + \cdots & & \\ & & n_1\frac{b_1^2}{2} + n_2\frac{b_2^2}{2} + \cdots & \\ 0 & & & \end{bmatrix}\begin{bmatrix} B(z_0) \\ B^{(1)}(z_0) \\ B^{(2)}(z_0) \\ \vdots \end{bmatrix} g(t). \tag{3}$$

The above diagonal matrix expresses the effects of the array of coils on the field and its derivatives $B^{(1)}, B^{(2)}, \ldots$ at z_0, the pick-up coil position. A gradiometer of Nth order will result when the *first N diagonal terms* are canceled, that is imposing the condition,[16]

$$\sum_{i=0}^{N} n_i \frac{b_i^{\alpha}}{\alpha!} = 0, \quad \alpha = 0,\ldots,N-1. \tag{4}$$

Such conditions are fulfilled by all existent gradiometers, even by the so-called asymmetric ones that use different areas for the sets of coils, and where n_i is not limited to be an integer.

THE GRADIOMETER SENSOR: A NONRECURSIVE SPATIAL FILTER APPROACH

A gradiometer detects a continuous time signal, sampling it at discrete points in space b_i which correspond to the coils' positions. The net detected signal, at each instant of time, is a weighted sum of all those sampled values. Thus it seems appropriate to use a digital mathematics formalism for describing the gradiometer sensor.

In such an approach, the output of a so-called moving average or nonrecursive filter is generally expressed as[17]

$$y_m = \sum_{i=-\infty}^{\infty} h_i x_{m-i}. \tag{5}$$

This procedure defines a new set of numbers y_m from the set of numbers x_m which correspond to the sampled values at constant intervals. The weighting factors h_i depend on the filter.

The discrete Fourier transform (DFT) of the signal (see for example Ref. 17) at some instant of time can then be expressed as

$$X(k) = \sum_{m=-\infty}^{\infty} x_m e^{-jm\lambda_s k}, \tag{6}$$

where k is the wave number and λ_s is the distance between two successive sampling points.

For our case of the gradiometer, assume that the distances b_i can be expressed as multiples of λ_s,

$$b_i = \beta_i \lambda_s, \tag{7}$$

where β_i has integer values and λ_s are the maximum common divisors of all the b_i. The signal detected by the gradiometer at position z_m over all its space will be

$$f(z_m) = \sum_{i=0}^{N} n_i \phi(z_m + b_i),$$

or considering the digital nature of the detection scheme,

$$f_m = \sum_{i=0}^{N} n_i \phi_{m+i}, \tag{8}$$

where $N+1$ is the number of coils, and $\phi(z_m + b_i) = \phi_{m+i}$ is the magnetic flux at the ith coil at some instant of

PLANAR GRADIOMETER INPUT SIGNAL RECOVERY USING A FOURIER TECHNIQUE

A.C. Bruno, A.V. Guida and P. Costa Ribeiro
Departamento de Física, Pontifícia Universidade Católica do Rio de Janeiro
C.P. 38071, 22453 Rio de Janeiro RJ, Brasil

1. INTRODUCTION

A great technical improvement in gradiometer construction has been obtained with thin film deposition techniques (1, 2). These techniques usually lead to planar designs. However, the output signal for this kind of gradiometer would be more difficult to interpret than the output of the common axial ones (3). The spatial dependence in the z direction, perpendicular to the coil plane, of a biomagnetic source is monotonic, but the spatial dependence in the coil's plane, x and y directions are usually not monotonic. This means that the signal in each planar gradiometer coil could be equally large. In other words, in a planar gradiometer there is not a pick-up coil that senses most of the signal and the compensating coils reject noise. This, would make it impossible to find a solution to the inverse problem by simple inspection of the output measurements even for such a simple source as the current dipole. However, it is always possible to use a fitting routine with variable parameters once a known source is expected (4).

The object of this paper is to apply to planar configurations a digital spatial filter model previously developed for axial gradiometers (5). This model will provide tools to overcome the problem of planar gradiometer output signal interpretation, without making any previous assumption about the kind of field source.

2. RECOVERY METHOD

The three main elements in a system approach are the input, the output and the transfer function of the system. According to this approach the gradiometer can be seen as a nonrecursive digital spatial filter having its own transfer function. More specifically it can be seen as a moving average filter. This kind of digital filter samples the signal to be measured with a sampling period λ_s and then makes a weighted sum of the sampled sequence according to weighting factors $h's$. The general expression for the transfer function $H_g(k)$ of this filter is (6):

$$H_g(k) = \sum_{i=-\infty}^{\infty} h_i e^{-jki\lambda_s}, \tag{1}$$

The equivalence between a moving average filter in space and an axial gradiometer is possible (5) because the gradiometer also "samples" the magnetic field intensities at different coil positions, making a weighted sum according to the number of turns in each coil (if a symmetric design is considered). Thus, according to (1) the gradiometer spatial transfer function $H(k)$ can be expressed as:

$$H(k) = A \sum_{i=0}^{N-1} n_i e^{-jkil}, \tag{2}$$

where k is the spatial frequency, A is the area of the coils, N is the number of coils, n_i is the number of turns of each coil and l is the base line. It is assumed that gradiometer coil's surface is so small that the field has a uniform distribution over it. Also $H(k)$ can be measured experimentally with a procedure already developed (7). Substituting the usual values for the n_i's and l, $H(k)$ will have a high pass shape. To complete the system approach, the gradiometer input can be defined as the field seen by the first gradiometer coil $b(z)$ and the output is defined as the flux seen by the whole gradiometer $\phi(z)$.

In the case of planar gradiometers it is straightfoward to apply the digital filter modeling as far as linear gradiometers are concerned (3). The sampling now occurs in one direction of the gradiometer plane, for instance the x direction. The same expression for $H(k)$ can be used to show the effect of the gradiometer over the signal to be measured.

As in any system, the relation between the input $b(x)$ and the output $\phi(x)$ in the frequency domain can be expressed as:

$$\Phi(k) = H(k)\,B(k) \tag{3}$$

where $\Phi(k)$ is the Fourier transform of the output flux $\phi(x)$ and $B(k)$ is the Fourier transform of the input field $b(x)$. Thus the Fourier transform of $b(x)$ can be obtained by:

$$B(k) = \Phi(k)/H(k). \tag{4}$$

Since the output flux of the gradiometer $\phi(x)$ can be measured, its Fourier transform $\Phi(k)$ can be calculated. $H(k)$ can be calculated from Eq. 2, thus the input field $b(x)$ can be found by taking the inverse Fourier transform of $B(k)$ as follows:

$$b(x) = \frac{1}{2\pi}\int_{-\infty}^{\infty} B(k)\, e^{jkx}\, dk. \tag{5}$$

3. SIMULATION

As an example, simulations of the recovery of the z component of the magnetic fields generated by a current and a magnetic dipole are done. The signals are detected by planar first and second order gradiometers along the x direction (see Fig. 1).

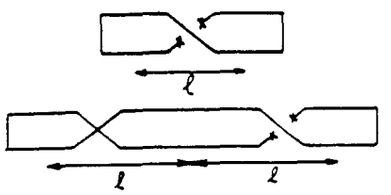

Fig. 1 - Schematic drawing of first and second order linear gradiometers.

They have loops of small area A separated by a distance l. To calculate the transfer function of the first order gradiometer, the summation in Eq. 2 will have only two terms:

$$H(k) = A\left[1 - e^{-jkl}\right], \tag{6}$$

and for the second order three terms:

$$H(k) = A\left[1 - 2e^{-jkl} + e^{-jk2l}\right]. \tag{7}$$

To produce the output $\phi(x)$, the dipoles are positioned in the following way: the current dipole is placed at the z axis z_0 cm below the gradiometer plane and is oriented in the y direction; while the magnetic dipole is placed at the same position but oriented in the z direction. Then, the gradiometer is displaced along the x axis from $-\infty$ to $+\infty$ giving an output as a function of x. The output of a first order gradiometer for a current dipole source placed at $z_0 = 3\,cm$, can be seen at Fig. 2 (dotted line) and is given by:

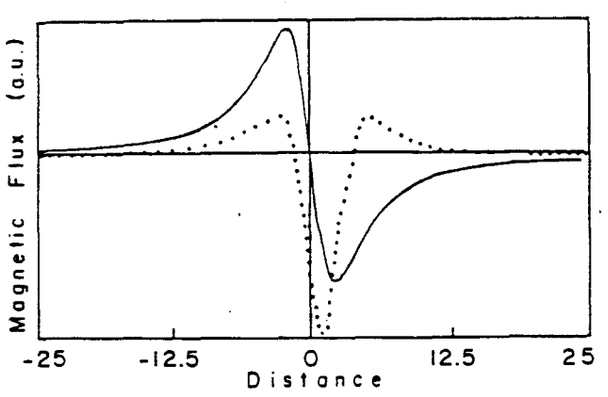

Fig. 2 - Output signal (dotted line) of a first order linear gradiometer as a function of distance for a current dipole source placed at a distance z_0 below the gradiometer. Recovered dipole field (continuous line) using the Fourier method.

$$\phi(x) = A\Big[b(x) - b(x-1)\Big], \tag{8}$$

where $A = 1$, $b(x)$ is given by the Biot-Savart law and $l = 2\,cm$. The output is not symmetric in relation to the origin due to the choice of taking the $x = 0$ position when the gradiometer's first coil is at the origin.

A Fourier transform is applied to the output $\phi(x)$ and the result divided by $H(k)$. The inverse Fourier transform of the division can also be seen at Fig. 2 (continuous line) which is the well known current dipole pattern. The difference between the recovered values and the actual current dipole field can be made as small as we want, depending only on the numerical precision used for the Fourier calculation.

Fig. 3a and 3b respectively shows the isovalue contour maps of the output of a first and second order planar gradiometers over a grid of 6×6 points, each one separated by the gradiometer baseline (l), for a current dipole source. The values of z_0 and l were the same as before. To recover the dipole field values in each position of the grid, the Fourier procedure explained above should be used for each grid line. At Fig. 3c is displayed the isofield lines of the recovered field.

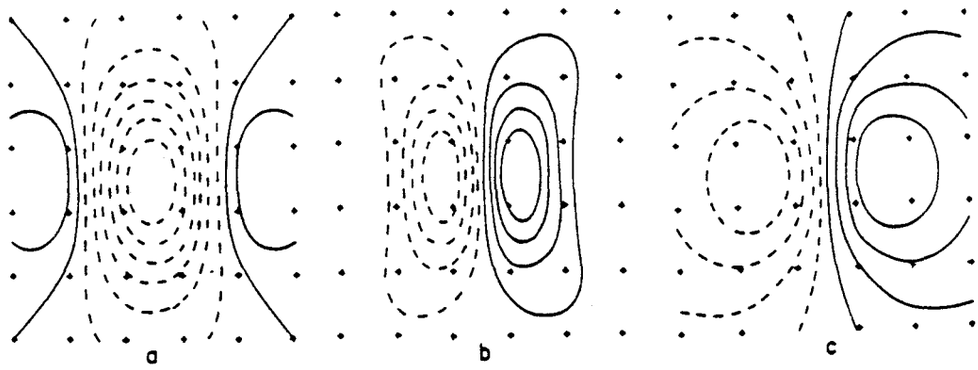

Fig. 3 – Isovalue contour map of the output of a first (a) and second (b) order linear gradiometer for a current dipole source placed at a distance z_0 below the measuring plane and oriented in the y direction. Recovered isofield contours using the Fourier technique (c).

Same as in Fig. 3, but using a magnetic dipole as source, isovalue contour maps of the output of the first and second order planar gradiometers are shown in Fig. 4a and Fig. 4b respectively. The output of the algorithm is displayed in Fig. 4c.

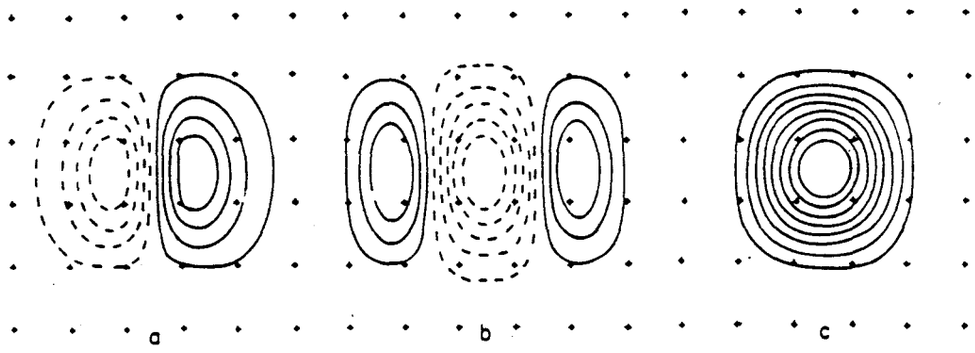

Fig. 4 – Isovalue contour map of the output of a first (a) and second (b) order linear gradiometer for a magnetic dipole source placed at a distance z_0 below the measuring plane and oriented in the z direction. Recovered isofield contours using the Fourier technique (c).

4. CONCLUSION

In order to implement the algorithm, some precautions must be taken to assure from a numerical point of view, a well behaved calculation. Theoretically $H(0) = 0$, the gradiometer's areas were made slightly different to avoid division by zero in Eq. 4, with $H(0)$ having the value of 0.001. The integral limits of the Fourier integrals in space (direct) and in frequency (inverse) were carefully chosen to cover a finite area over the integration axis (8). The values used in the examples were -30 to $+30\,cm$ in space and -3 to $3\,cm^{-1}$ in frequency. Concerning practical measurements, when the output analytical expression is not available as in Eq. 8, the algorithm precision would be a function of the number of output measurements taken, the distances between them and, of course, the experimental errors. In previous calculations, a negligeably small area has been assumed; thus the two sampling points located at 0 and 1, correspond to the center of the gradiometer coils. A possible way to take into account a finite area effect, is to consider the rectangular shape at Fig. 1. This can be done by using many more sampling points, assuming a new λ_s much smaller than l. This will be equivalent to subdividing the area into a large number of small adjacent "loops". Decreasing 20 times the sampling period, the transfer function of the first order gradiometer $H_s(k)$ is given by:

$$H_s(k) = \frac{A}{20} \sum_{i=-5}^{15} n_i \, e^{-jkil/20}, \tag{9}$$

where $n_i = 1$, for i from -5 to 4, $n_5 = 0$ and $n_i = -1$, for i from 6 to 15. The magnitude of the transfer function given by Eq. 9 differs less than six percent from Eqs. 6 and 7 for frequencies up to $1\,cm^{-1}$. Thus, the correction for a gradiometer with a finite area would be small.

In conclusion, the magnetic field spatial distribution of a magnetic and a current dipole sources were recovered from the gradiometers. The algorithm used does not depend on the kind of field source and enables the study of fields originated by non simple sources, as cardiomagnetic and more complex neuromagnetic sources. It can be noticed that the isovalue contour lines obtained by displacing the gradiometer over the points of a grid could be obtained by an array of planar gradiometers, thus the described algorithm seems to be very suitable to handle a gradiometer array output.

ACKNOWLEDGEMENT

Helpful discutions were made with Dr. O. Symko, Department of Physics, University of Utah and with Dr. A. Fonseca Costa, Instituto de Biofísica UFRJ, who reviewed the manuscript and made numerous valuable suggestions.

REFERENCES

(1) Ketchen M. B., Goubau M. and Clarke J. 1978 *J. Appl. Phys.* **49** 4111–6.

(2) Careli P. and Foglietti V. 1983 *J. Appl. Phys.* **54** 6065–7.

(3) Romani G. L. 1987 *Phys. Med. Biol.* **32** 23–32.

(4) Careli P. and Leoni R. 1986 *J. Appl. Phys.* **59** 645–50.

(5) Bruno A. C., Costa Ribeiro P., von der Weid J. P. and Symko O. G. 1986 *J. Appl. Phys.* **59** 2584–9.

(6) Schwartz M. and Shaw L. 1975 *Signal Processing* (McGraw Hill, Tokyo) Wall V. J., Nieuwenhuyzen G. L. and Klapwijk T. M. 1983 *IEEE Trans. on Mags.* **MAG-19** 648–51.

(7) Costa Ribeiro P., Bruno A. C., Paulsen C. C. and Symko O. G. 1987 *Rev. Sci. Instrum.* **58**, 1510.

(8) Chen C. T. 1979 *One Dimension Digital Signal Processing* (Marcel Dekker, New York).

ANEXO 7

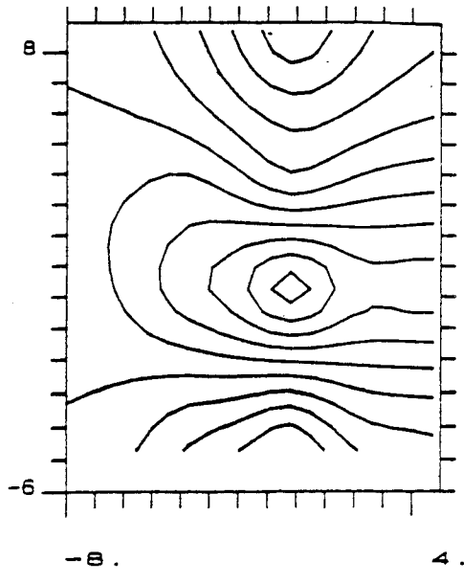

Figure 2. Experimental contour map illustrating the distribution of the magnetic signal generated by a current dipole located at a distance of 3 cm from the wound-wire planar gradiometer, and inside a glass sphere filled with a saline solution. Shaded areas represent negative polarity. Units are in centimeters.

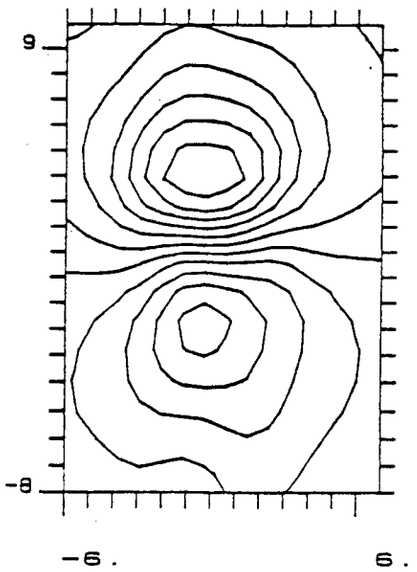

Figure 3. Experimental contour map illustrating the distribution of the magnetic field generated by the same source as in the previous figure, as measured by a four-channel system using vertical gradiometers with a baseline of 7 cm. Shaded area represents negative polarity. Units are in centimeters.

Fig.2 shows the experimental pattern obtained from the model source with the wound-wire planar gradiometer described above, whereas fig.3 shows the pattern as measured from the same source by the four vertical gradiometers system. The latter is clearly very similar to the well known theoretical pattern generated by a current dipole in a homogeneous conducting sphere.[2] The localization algorithm carried out on the measured distribution provided a quite good agreement in the location of the source (less than 1 mm for each orthogonal direction). Slighthly larger error (few millimeters) was obtained in source localization from the experimental map of fig.2. This may be due to two reasons: i) a larger sensitivity of planar gradiometers to errors in positioning the sensor;[12] ii) a too large spatial sampling rate, which was kept identical to that used for the vertical gradiometer system. These sources of error are more critical when using planar gradiometers, since they exibit a strong dependence on the angle between the sensor axis and the source, and because of the enhanced sensitivity of planar devices to higher spatial frequencies.[6]

Results on human subjects

The wound-wire planar gradiometer was used to measure and map the magnetic field associated with heart and brain activity.

Fig.4 shows an averaged magnetocardiogram as measured from a normal subject in a recording bandwith 0.1-250 Hz. Similar traces were recorded at 48 positions of the subject's chest, according to the conventional grid for cardiomagnetic measurements[13] enlarged by 2 columns. The quality of the traces permits to calculate spatial mapping of the measured signals at successive time instants. An example is reported in fig.5, where the maps refer to that portion of the heart cycle commonly defined as QRS complex. The maps are separated by 10 ms, according to the time scale of fig.4. A localization algorithm carried out for the maps at 200 and 250 ms gave a source localizaton well in agreement with the known location of the equivalent current dipole for that portion of the heart cycle.[14]

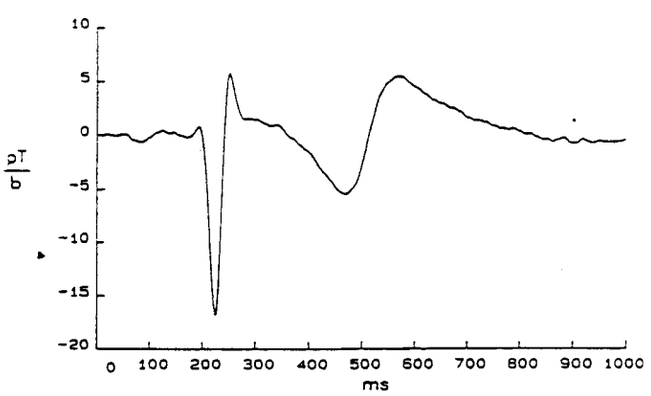

Figure 4. Magnetocardiogram recorded over the chest of a normal subject using the wound-wire gradiometer system. The trace is obtained by averaging 64 heart beats. The vertical scale represents the field strength expressed in picotesla, divided by the baseline b of the gradiometer (2 cm).

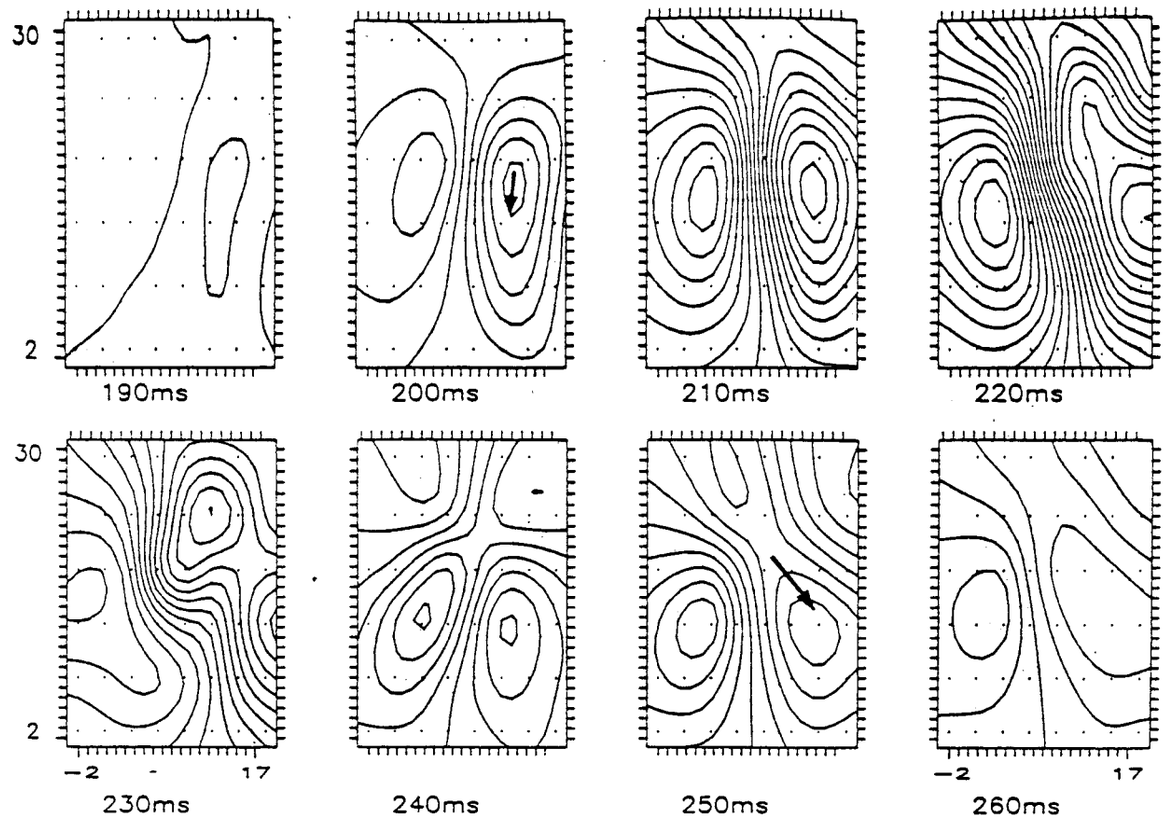

Figure 5. Sequence of contour maps illustrating the [illegible]tion of the measured magnetocardiogram at successive time instants of the heart cycle, indicated below [illegible], and referring to the time scale in Fig. 4. The maps were obtained from the magnetic signals measured at 4[illegible] of the subject's chest according to the procedure described in the text. Units are expressed in centi[illegible]. The shaded areas represent negative polarity.

The same system has been also used to rec[illegible] neuromagnetic activity evoked by the stimulation of the median nerve at the wrist of a normal subject. The stimulation consisted of a short current pulse (100 us duration, slightly above the thumb movement threshold). Fig.6 shows an example of the measured evoked activity in a recording bandwith 1-200 Hz. Adequate mapping of somatosensory signals in order to achieve source localizatio[illegible] is being carried on in our laboratory.

Conclusions

The feasibility of using planar gradiometers to detect biomagnetic fields was experimentally checked, both on a model source and on human subjects. The use of a wound-wire planar gradiometer coupled to a RF SQUID represents only a preliminary approach, since a much better signal to noise ratio might presumably be obtained using microfabricated planar gradiometers directly integrated with DC SQUIDs in a single chip. Intentionally, the dimensions of the wound-wire planar gradiometer were chosen not too different from those achievable by microfabrication. A much larger signal to noise ratio should then be ensured by the better performances of DC SQUIDs. In spite of the limitations of the presently used device the results were in good [illegible]reement with those obtained with conventional [illegible]rtical gradiometers, thus supporting the idea that planar gradiometers are the best candidates for integration in large biomagnetic systems.

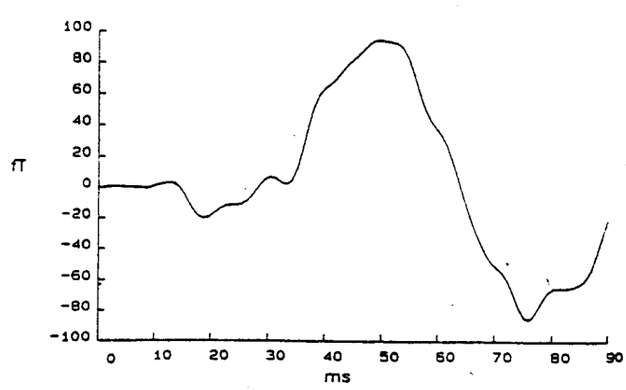

Figure 6. Neuromagnetic evoked response elicited by electric stimulation of the median nerve at the left wrist of a normal subject, as measured over the right somatosensory cortex. Deviations from the zero line represent various components in the cerebral response occurring at increasing delays, or latencies, from the stimulus onset (at t=0 s).

Acknowledgments

The authors thank G.M.Ernè for kindly providing the software to achieve source localization with planar devices.

References and notes

* Permanent address: Departamento de Fisica, Pontificia Universidade Catolica, Caixa Postal 38071, Rio de Janeiro, BRASIL.

** and Istituto di Fisica Medica, Università "G. D'Annunzio", Via dei Vestini, Chieti, ITALY.

[1] R. Ilmoniemi, R. Hari, and K. Reinikainen, "A four-channel SQUID magnetometer for brain research", Electroencephalogr. clin. Neurophysiol., vol. 58, pp. 467-473, 1984.

[2] G.L. Romani, "Biomagnetism: an application of SQUIDs sensors to medicine and physiology", Physica, vol. 126B, pp. 76-81, 1984.

[3] S.J. Williamson, M. Pelizzone, Y. Okada, L. Kaufman, D.D. Crum, and J.R. Marsden, "Magnetoencephalography with an array of SQUID sensors", Proceedings of the 10th ICEC, (H. Collan, P. Berglund and M. Krusius Eds.), Butterworth, Westbury House, pp. 339-348, 1984.

[4] J.E. Zimmerman and N.V. Frederick, "Miniature ultra-sensitive magnetic gradiometer and its use in cardiography and other applications", Appl. Phys. Lett., vol. 1, pp. 16-19, 1971.

[5] G.L. Romani, S.J. Williamson, and L. Kaufman, "Biomagnetic Instrumentation", Rev. Sci. Instrum., vol. 53, pp. 1815-1845, 1982.

[6] G.M. Ernè and G.L. Romani, "Performances of high order planar gradiometers for biomagnetic source localization", SQUID 85: Superconducting Quantum Interference Devices and their applications, (H.D. Hahlbohm, H. Lübbig Eds.), Walter De Gruyter, Berlin-New York, pp. 951-961, 1985.

[7] P. Carelli and R. Leoni, "Localization of biological sources with arrays of superconducting gradiometers", J. Appl. Phys., vol. 59, pp. 645-650, 1986.

[8] G.L. Romani, "The inverse probleme in MEG studies: an instrumental and analytical perspective", Phys. Med. Biol., vol. 32, pp. 23-31, 1987.

[9] W.J. de Wall and T.M. Klapwijk, "Compact integrated DC SQUID gradiometer", Appl. Phys. Lett., vol. 41, pp. 669-671, 1982.

[10] R.P. Bain, A.E. Jones, and C.E. Tenelooe, "Design of high-order superconducting planar gradiometers with shaped asymmetric near-source response", IEEE Trans. Mag., vol. MAG-23, pp. 1146-1149, 1987.

[11] G.L. Romani, R. Leoni, C. Salustri, "Multichannel instrumentation for biomagnetism", SQUID 85: Superconducting Quantum Interference Devices and their applications, (H.D. Hahlbohm, H. Lübbig Eds.), Walter De Gruyter, Berlin-New York, pp. 910-932, 1985.

[12] G.L. Romani and R. Leoni, "Localization of cerebral sources with neuromagnetic measurements", Biomagnetism: applications and theory, (H. Weinberg, G. Stroink and T. Katila Eds.), Pergamon Press, New York-Toronto, pp. 205-220, 1985.

[13] M. Saarinen, P. Siltanen, P.J. Karp, and T.E. Katila, "The normal magnetocardiogram I: Morphology", Ann. Clin. Res., vol. 10 (S21), pp. 1-43, 1978.

[14] G.M. Ernè, M.R. Fenici, "The present state of magnetocardiography", Proceedings of the 10th ICEC, (H. Collan, P. Berglund and M. Krusius Eds.), Butterworth, Westbury House, pp. 329-338, 1984.

ANEXO 8

Neuromagnetic localization performed by using planar gradiometer configurations

A. C. Bruno[a)]
Departamento de Fisica, Pontificia Universidade Católica, Caixa Postal 38071, Rio de Janeiro, RJ, Brazil

G. L. Romani
Istituto di Fisica Medica, Università, "G. D'Annunzio" Via dei Vestini, 66100, Chieti, Italy and Istituto di Elettronica dello Stato Solido-CNR, Via Cineto Romano 42, 00156, Roma, Italy

(Received 15 March 1988; accepted for publication 7 October 1988)

The spatial discrimination of planar and axial gradiometers is compared by using a spatial filtering model. By measuring somatosensory evoked fields, equivalent current dipoles were localized with the use of planar gradiometer outputs. The planar configurations were obtained by combining, in a proper way, the outputs of a four-channel biomagnetic system. It was observed that with a proper signal-to-noise ratio, the use of the planar configurations did not significantly affect the localization precision.

INTRODUCTION

The impressive results achieved in the investigation of brain and heart physiology and pathology by the biomagnetic method have given an extraordinary impulse to the development of multichannel SQUID systems.[1-3] Although the present state of the art is constrained to instrumentation with a limited number of adjacent magnetic sensors, it is commonly agreed that the final goal of a real time functional localization will be achieved with instruments able to detect biomagnetic signals at approximately 100 adjacent sites of the scalp or of the chest and to perform this detection simultaneously.

Several studies performed recently[4-6] have proposed an alternative solution with respect to the traditional detecting configuration that couples axial gradiometers to the SQUID. Indeed, the use of an axial geometry for wound wire gradiometers, besides the fact that has been widely adopted in almost all the biomagnetic systems operating in the world, presents several drawbacks when integration in large arrays is required.[7] Although the performances of arrays of axial and planar gradiometers have been compared,[7,8] all comparisons were based, so far, on computer simulations. The time when practical devices will become available for experimental checks is not far away, nevertheless some preliminary approaches can be done with existing devices, certainly in not optimized conditions, to verify at least some of the predicted performances. In this work a comparison between the current dipole sensitivities of axial and planar gradiometers is made. In addition, an experimental study about the localization performance of planar gradiometers is reported when measuring neuromagnetic sources. The planar gradiometer configurations were obtained by using an appropriate combination of the outputs of the four-channel biomagnetic system operating at the Istituto di Elettronica dello Stato Solido in Rome.[9]

THEORETICAL ANALYSIS

The spatial discrimination of planar and axial gradiometers can be evaluated by using a spatial filtering model previously developed[10] for analysis and design of gradiometers. This model consists of a gradiometer as a nonrecursive digital spatial filter. According to it, the gradiometer *samples* in space, the magnetic field intensities, at the different coils positions, where the sampling period is the gradiometer baseline. Also, a weighted sum of the sampled sequence is made with the weighting factors being the area of each coil. The gradiometer spatial transfer function $H(k)$ can be measured,[11] or can be obtained theoretically[12] by taking the discrete Fourier transform of the sequence of number of turns of the gradiometer coils n_i

$$H(k) = \sum_{i=0}^{N} n_i e^{-jki\lambda_s}, \tag{1}$$

where N is the gradiometer order, k is the spatial frequency, and λ_s is the baseline. If the usual values for n_i and λ_s are used in (1) the transfer function has a high-pass shape.[12] The spatial discrimination is accomplished because distant sources have only low-frequency components and near sources low- and high-frequency components in the spatial frequency spectrum.

Evaluating the gradiometer input and output energies in the frequency domain, and for certain ranges of source and sensor parameters, we can see a higher degree of spatial discrimination of a planar gradiometer when compared with an axial one. As planar gradiometers do not have the *pickup* coil,[8] the term *first* coil will be used in general, meaning the pickup coil in the axial case and one reference coil in the planar case. In the space domain, the gradiometer input is defined as the flux seen by just the first coil and the output as the flux seen by the whole gradiometer. In the frequency domain the spatial Fourier transform $\Phi_0(k)$ of the gradiometer output flux is the product of the transfer function $H(k)$ by the spatial Fourier transform $\Phi_i(k)$ of the input flux

$$\Phi_0(k) = H(k)\Phi_i(k). \tag{2}$$

The input and output energies, respectively, E_i and E_0, can be calculated by integrating the square of the magnitude of the spatial Fourier transform of the input and output signals[13]:

$$E_i = \int_{-\infty}^{\infty} |\Phi_i(k)|^2 dk \tag{3}$$

[a)] Present address: Istituto di Elettronica dello Stato Solido-CNR, Rome, Italy.

 0021-8979/89/052098-04$02.40 © 1989 American Institute of Physics

and

$$E_0 = \int_{-\infty}^{\infty} |\Phi_0(k)|^2 dk. \quad (4)$$

Let us assume that signal and noise are detected by an axial first-order gradiometer and by a linear gradiometer[8] with the same baseline and unity coil areas. The spatial transfer functions are the same since the difference between the two designs is only in the direction of the spatial sampling, z for the axial and x for the linear design. The rejection of distant sources (noise) is the same, because they have uniform spatial distribution in all directions. However, there is a significant difference for a biomagnetic source due to the different spatial distribution of the near dipolar field in different directions. Thus, the input field of the linear gradiometer is different from the one of the axial gradiometer for near sources. In Figs. 1(a) and 1(b) it is shown that the spatial Fourier transforms of the input flux (continuous line) generated by a near source and its correspondent output flux (dashed line) of, respectively, axial first-order and linear gradiometers. The input field is generated by a current dipole pointing in the y direction and placed below the gradiometers plane at a distance equal to one baseline. Notice that the Fourier spectrum is monotonic in the z direction, with the higher-intensity components laying near frequency zero. However, it is not monotonic in the x direction, with the peak frequency depending on the dipole depth. As the gradiometer acts as a high-pass spatial filter, it will reject low portions of the frequency spectrum and, therefore, the input signal in the x direction is less affected by it.

For example, suppose that the current dipole depth and the gradiometer baseline are equal to 3 cm. By using the spatial dependence of the dipolar field, given by the Biot–Savart law, and evaluating integrals (3) and (4), the output of the first-order gradiometer has 35% energy less than the energy coupled to the first coil. However, for the linear gradiometer, the energy loss is about 25%, so there is a gain in the output energy. If the dipole depth is increased to 6 cm, the axial and linear output energies have losses of, respectively, 80% and 65%, which is still in favor of the linear geometry. With this higher sensitivity to near sources, planar gradiometers should discriminate a better signal against noise. On the other hand, the pattern detected when sensing this typical biomagnetic model source is more complex, since in the planar design there is no pickup coil and also is lacking a rotational symmetry.

EXPERIMENTAL MEASUREMENTS

In order to study the localization performance of planar gradiometers, planar configurations were obtained by combining the individual outputs of a four-channel system. Two kinds of planar configurations were obtained: the linear design, by making the difference between two channels, and the quadratic design,[8] by making channel 1 − channel 2 + channel 3 − channel 4. There are some critical problems with this planar simulation. The V/T calibration ratio of each channel has errors that can be estimated as about 10%. Also, the noise in the system channels is uncorrelated. As the measurement bandwidth is about 2 kHz, additions and subtractions between channels will result in a planar gradiometer noise higher than the noise of each channel.

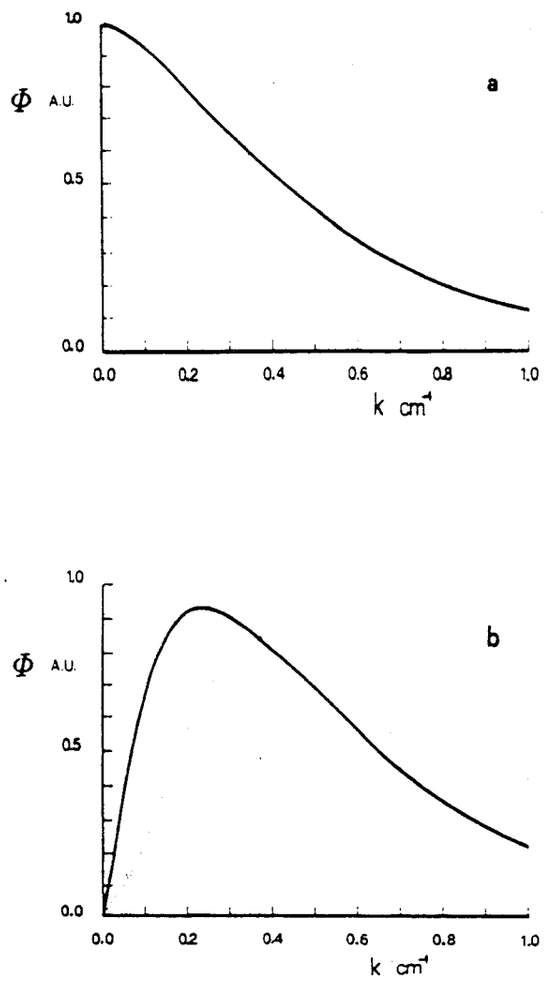

FIG. 1. Spatial Fourier spectra of the input flux (continuous line) and output flux (dashed line) of an (a) axial first order and (b) a linear gradiometer. The input flux is generated from a current dipole placed 3 cm below the gradiometers plane. Both gradiometers have a 3-cm baseline.

The four-channel system is composed of four axial second-order gradiometers, having coils with a 1.5 cm diam and a 7 cm baseline. The distances between the axis of the gradiometers are 2 cm. Each channel of the system has different sensitivities, channels 1 and channel 2 have 45 fT/$\sqrt{}$Hz, channel 3 has 55 fT/$\sqrt{}$Hz, and channel 4 has 40 fT/$\sqrt{}$Hz. As we will see later these different sensitivities of each channel will play a very important role on the planar configurations performances. We have detected somatosensory evoked fields (under median nerve stimulation) produced by shallow sources, 2 cm in the average. With the scalp-to-pickup coil distance being about 2 cm, the baseline is almost twice the distance from the first coil to the dipole. This will entail an average localization error[14] of about 8% if the axial gradiometer of each channel, for the planar simulations, is treated as a magnetometer.

RESULTS AND DISCUSSION

The results in source localization obtained by using the four channels are compared with the ones obtained by using the planar configurations output. After data acquisition, fil-

tering, and averaging, a localization program currently in use in this laboratory[7] finds the intensity, direction, and position in the brain of an equivalent current dipole responsible for the measured field. The localization program was modified to accept the new data and to account for the planar designs. Four different measurements were performed in two different subjects. The equivalent current dipole depths of the evoked stimulation found with the original system ranged between 1.2 and 2.5 cm from the scalp in the four measurements. The original dipolar patterns of these measurements were checked by looking at the output isofield contour maps at a certain instant of time. One of them can be seen in Fig. 2(a) (polarity not shown), as well as the 48 measuring positions. The isofield contour map obtained combines the outputs of the axial gradiometers in order to simulate a linear planar gradiometer, as described above, in correspondence of the same measurement and instant of time can be seen in Fig. 2(b) (polarity not shown). The 12 straight lines in the figure represent the sensors whose outputs were subtracted. This contour map of course does not have the same graphic significance of the preceding one, since it has the same number of contour lines of Fig. 2(a) but four times fewer measuring points. Also, it would not be equal to a contour map detected by a linear gradiometer, since the equivalent linear configurations are rotated from position to position, as can be seen in the figure. The measuring positions could not have the proper spatial distribution, concerning gradient measurements, because of the measuring procedure (the dewar could not be rotated).

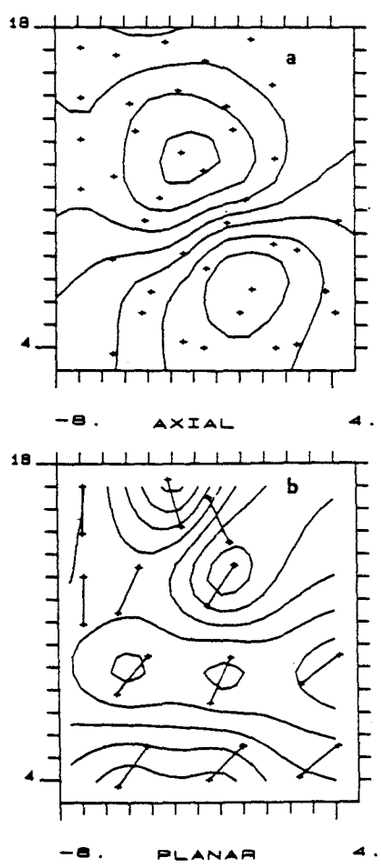

FIG. 2. Isofield contour maps of somatosensory evoked responses by using (1) the four-channel system in 48 measuring positions, and (b) a linear configuration in 12 positions for the same measurement and instant of time (1 ms). The straight lines in (b) join the sensors whose outputs were subtracted.

Comparisons with the original results are done by checking the errors in the position (P), strength (Q), and orientation (Ψ) of the equivalent current dipole, found by using the planar geometries. The dipole localization is done in terms of spherical coordinates θ, ϕ, and r, referred to the best sphere that fits the subject head. Hence, the total rms localization error, E_P, is defined as

$$E_P = \sqrt{\left(\frac{\Delta\theta}{\theta}\right)^2 + \left(\frac{\Delta\phi}{\phi}\right)^2 + \left(\frac{\Delta r}{r}\right)^2}, \tag{5}$$

where $\Delta\theta/\theta$, $\Delta\phi/\phi$, and $\Delta r/r$ are the relative percentage errors for the position coordinates obtained by using the original output and the relative percentage errors obtained with the planar outputs. The values of θ and ϕ provided by the fit were in all cases about 1 and 6 rad, respectively. The comparison between the original and new results can be completed considering the strength error $E_Q = \Delta Q/Q$ and the orientation error, $E_\Psi = \Delta\Psi/\Psi$.

Table I shows minimum and maximum errors obtained in the four measurements with the linear and the quadratic configurations. The planar configuration obtained by making the difference between channels 1 and 4 had the minimum errors. The localization error was 10%, the strength error 2%, and the orientation error 0.5%, which are indeed very small figures. This was intuitively expected since this linear configuration was obtained by using the two channels with the best sensitivities, respectively, 45 and 40 fT/$\sqrt{\text{Hz}}$. The maximum errors were obtained in another measurement with the linear configuration being the difference between channels 3 and 4. The errors were 18% for position, 14% for orientation, and 35% for strength. The difference between these two results is due to the different intensities of noise in each linear configuration. Also, the depths in the two measurements were different, 1.2 cm from the scalp in the former and twice deeper in the latter, which can explain the big difference between the minimum and maximum strength errors. Concerning the quadratic design, the differences between minimum and maximum errors were much smaller than in the linear case. This is due to the stronger effect of uncorrelated noise in the four channels. The average

TABLE I. Maximum and minimum relative percentual errors obtained for localization, strength, and orientation, in four measurements by using the outputs of linear and quadratic gradiometers when compared with the results obtained with the original four-channel system.

Planar gradiometers	E_P(%) min–max	E_Q(%) min–max	E_Ψ(%) min–max
linear	10–18	2–35	0.5–14
quadratic	15–17	27–44	4–9

TABLE II. Maximum and minimum relative percentual errors obtained for localization, strength, and orientation, in four measurements by using the outputs of channel 3 only and channel 4 only, when compared with the results with the original four-channel system.

Axial gradiometers	$E_P(\%)$ min–max	$E_Q(\%)$ min–max	$E_\psi(\%)$ min–max
channel 3	16–38	15–57	8–17
channel 4	6–11	3–6	2–8

errors were 16% for position, 35% for strength, and 7% for orientation. These errors are in the same range of the ones obtained by using channel 3 as one of the elements in the linear configuration. The maximum orientation error found with all the planar configurations was 14%.

The original system has provided 48 measuring positions for the localization program and the planar configurations of only 12. In order to see the influence of the spatial sampling in the localization accuracy and, most importantly, the influence of each channel sensitivity, let us use just one channel of the system giving for the localization program the same number of measurements as in the planar case. In Table II are the errors due to using just one channel to perform the localization. As it is a question of sensitivity, we have used the channels with best and worst sensitivity, respectively, channel 4 (40 $fT/\sqrt{Hz}$) and channel 3 (55 $fT/\sqrt{Hz}$). The minimum errors were found, as was expected, by using channel 4. They were 6% for position, 3% for strength, and 2% for orientation. In an overall view, these errors are very similar to the minimum errors obtained with the linear configuration. Performing the localization by using channel 3 only, the minimum errors obtained were 16% for position, 15% for strength, and 8% for orientation. However, the maximum errors have reached 38% for position, 57% for strength, and 17% for orientation. These errors are bigger than the maximum errors obtained in all planar configurations. Thus, it seems clear that the use of channel 3 has placed a limit on the sensitivity of all the planar configurations obtained by using it.

CONCLUSION

It was experimentally checked that the use of the complex planar configuration outputs did not significantly affect the localization accuracy, provided that the signal-to-noise ratio was sufficiently good. Hence, as an extension to a recent work[15] concerning only axial gradiometers, the localization performance is still a problem of signal-to-noise ratio even if a planar gradiometer is used. The number of measurements and the spatial sampling are also important factors to consider. However, in a multichannel context, as we saw above in a limited scope, all gradiometers must have almost the same sensitivity, otherwise, increasing the number of channels and consequently the spatial sampling, will not significantly enhance the localization precision.

ACKNOWLEDGMENTS

One of the authors, A. C. Bruno, has carried out this work under support of the International Center for Theoretical Physics Program for Training and Research in Italian Laboratories, Trieste, Italy. The authors are grateful to V. Pizzella for help and suggestions during the preparation of the manuscript.

[1] R. Ilmoniemi, R. Hari, and K. Reinikainen, Electroencephalogr. Clin. Neurophys. **58**, 467 (1984).
[2] G. L. Romani, Physica **126B**, 70 (1984).
[3] S. J. Williamson, M. Pelizzone, Y. Okada, L. Kaufman, D. B. Crum, and J. R. Madsen, in *Biomagnetism: Theory and Applications*, edited by H. Weinberg, G. Stroink, and T. Katila (Pergamon, New York, 1984), p. 46.
[4] V. J. de Wall and T. M. Klapwijk, Appl. Phys. Lett. **41**, 669 (1982).
[5] P. Carelli and V. Foglietti, J. Appl. Phys. **54**, 6065 (1983).
[6] M. B. Ketchen, J. Appl. Phys. **58**, 4322 (1985).
[7] P. Carelli and R. Leoni, J. Appl. Phys. **59**, 645 (1986).
[8] S. N. Erne and G. L. Romani, in *SQUID 85: Superconducting Quantum Interference Devices and their Applications*, edited by H. D. Hahlbohm and H. Lubbig (de Gruyter, Berlin, 1985), p. 951.
[9] G. L. Romani, R. Leoni, and C. Salustri, in *SQUID 85: Superconducting Quantum Interference Devices and their Applications*, edited by H. D. Hahlbohm and H. Lubbig (de Gruyter, Berlin, 1985), p. 919.
[10] A. C. Bruno, P. Costa Ribeiro, J. P. von der Weid, and I. R. Eghrari, in *Biomagnetism: Theory and Applications*, edited by H. Weinberg, G. Stroink, and T. Katila (Pergamon, New York, 1984) p. 67.
[11] P. Costa Ribeiro, A. C. Bruno, C. C. Paulsen, and O. G. Symko, Rev. Sci. Instrum. **58**, 1510 (1987).
[12] A. C. Bruno, P. Costa Ribeiro, J. P. von der Weid, and O. G. Symko, J Appl. Phys. **59**, 2584 (1986).
[13] C. T. Chen, *One Dimensional Digital Signal Processing* (Dekker, New York, 1979).
[14] G. L. Romani, S. J. Williamsom, and L. Kaufman, Rev. Sci. Instrum. **53**, 1815 (1982).
[15] B. N. Cuffin, Phys. Med. Bio. **32**, 33 (1987).

ANEXO 9

SERVIÇO DE BIBLIOTECA E INFORMAÇÃO - IFQSC
FÍSICA

SPATIAL DECONVOLUTION ALGORITHM FOR SUPERCONDUCTING PLANAR GRADIOMETER ARRAYS

A.C. Bruno and P. Costa Ribeiro
Departamento de Fisica, Pontificia Universidade Catolica
Caixa Postal 38071, Rio de Janeiro, 22453, Brazil.

Abstract

A digital filter model used previously to describe axial gradiometers is used here to study arrays of planar first order gradiometers. As an application of this technique a spatial deconvolution algorithm is developed to recover from the output measurements the input field. The influence of parameters like source depth and the gradiometer array density is also discussed by means of computer simulations.

Introduction

Nowadays biomagnetic field measurements[1] are made in several research institutes and hospitals. Usually in these environments, magnetic noise intensities surpass biomagnetic fields by various orders of magnitudes. One of the methods used to overcome this problem is known as spatial discrimination. It consists of coupling a set of coils in a gradiometric[2] configuration to a *rf* or a *dc* SQUID[3]. The gradiometer attenuates drastically fields originated from distant sources (noise), but it is sensible to fields from near biomagnetic sources. Generally the measurements are taken by displacing the gradiometer over a great number of positions in the vicinity of the biomagnetic source, which is time consuming and allows changes on the subject conditions from one measurement to another. The need for multi-channel systems has given recently, an extraordinary impulse to their development although at present contrained to a limited number of adjacent channels[4-6].

The gradiometer configuration can be axial[2] or planar[7]. Usually axial gradiometers are made by winding superconducting wire round a low thermal expantion support.. Due to mechanical limitations of this process, some compensating adjustments[8,9] must be added to increase the gradiometer performance. Recently a great technical improvement in gradiometer and SQUID construction has been obtained with thin film deposition techniques[10-12] which will allow fabrication of arrays with a large number of detecting sensors. Usually providing planar geometries, this technique leads to gradiometers with an intrinsic balance[11,12] better than the axial gradiometer made of wire. However, the planar design has a difficult output signal interpretation[12], because planar gradiometers do not have a *pick-up* coil that senses most of the signal and compensating coils for noise rejection as in the case of the axial one. This happens because the spatial decay in the x and y directions are usually not monotonic as in the case of the z direction.

The objective of this paper is to apply a digital spatial filter model previously developed to analyse and design axial gradiometers[13-15] to arrays consisting of planar gradiometers. This model will provide a characterization for the array, in terms of its spatial transfer function. Using this model, it will be possible to recover the original spatial dependence of the field source, overcoming the problem of the planar output signal interpretation. As a consequence, it will also give tools to study the optimal number of sensors, distances between them and array shape.

Digital Spatial Filtering Model

The gradiometer can be regarded as a nonrecursive digital spatial filter having its own transfer function. More specifically it can be seen as a moving average filter in space. A *time* digital moving average filter samples the signal to be measured with a sampling period T and then makes a weighted sum of the sampled sequence according to weighting factors h_i's. The general expression for the transfer function $H_t(w)$ of this filter is[16]:

$$H_t(w) = \sum_{i=-\infty}^{\infty} h_i e^{-jwT}, \qquad (1)$$

where w is the temporal frequency. Notice that Eq. 1 is the discrete Fourier transform of the sequence h_i.

It is possible to make the equivalence between a moving average filter in time and an axial gradiometer because the gradiometer also samples the magnetic field intensities at the different coils' positions along the z direction, making a weighted sum of them according to the number of turns of each coil. Hence, according to Eq. 1 the gradiometer spatial transfer function H(k) could be expressed as :

$$H(k) = \sum_{i=0}^{N-1} n_i e^{-jk\lambda_i}, \qquad (2)$$

where k is the spatial frequency, N is the number of coils, n_i is the number of turns of each coil and λ_i is the baseline. It is assumed that gradiometers'coils surface are small enough so that the field has a uniform distribution over them. Also H(k) can be measured experimentally with a procedure already developed[17]. Substituting the n_i's and λ_i by the values usually used for gradiometers, H(k) will have a high-pass shape[14]. The spatial discrimination is accomplished because far sources have only low frequency components of its Fourier spectrum, which are attenuated. On the contrary, near sources have low and high frequency components.

In the case of planar gradiometers it is straightforward to apply the digital filter model developed for the axial gradiometer as far as linear[7] gradiometers are concerned. The sampling now occurs in one direction of the gradiometer plane, for instance the x direction. Thus, the same expression for H(k) can be used to characterize the transfer function of the linear gradiometer. For other types of planar designs which sample in more than one direction[12], the transfer function could be calculated by taking the two dimentional discrete Fourier transform[18] of the matrix that would represent the areas of each coil.

Recovery Method and Simulations

As a system approach, an input and an output must be defined. The spatial filter input will be defined as the flux seen by the first gradiometer coil $\phi_i(x)$ and the output will be defined as the flux seen by the whole gradiometer $\phi_o(x)$. The relation between the input and output in the frequency domain can be expressed as:

$$\Phi_o(k) = H(k)\,\Phi_i(k) \qquad (3)$$

where $\Phi_o(k)$ is the Fourier transform of the output flux $\phi_o(x)$ and $\Phi_i(k)$ is the Fourier transform of the input flux $\phi_i(x)$. Since $\phi_o(x)$ can be measured, its Fourier transform $\Phi_o(k)$ can be calculated. Also $H(k)$ can be calculated from Eq. 3 thus, the

Manuscript received August 22, 1988

0018-9464/89/0300-1219$01.00©1989 IEEE

input flux $\phi_i(x)$ can be recovered by taking the inverse Fourier transform of $\Phi_i(k)$ as follows:

$$\phi_i(x) = \frac{1}{2\pi}\int_{-\infty}^{\infty} \frac{\Phi_o(k)}{H(k)} e^{jkx} \cdot dk. \qquad (4)$$

The concept of the linear gradiometer transfer function can be extended to the entire array because each gradiometer samples in the same plane of the array grid. It is the same as if one gradiometer would be displaced over the grid. It should be stressed that this is not the case of an array of axial gradiometers since they sample along the z direction and not over the plane of measurement.

Some recovery simulations are made of the z component of the magnetic field generated by the most common model source in biomagnetism, the current dipole. The signals are detected by arrays consisting of first order linear gradiometers along the x direction. The arrays are squared and have an uniform gradiometer density. They are characterized by the array parameter a which is the distance among the array elements. The gradiometers have loops of negligible small area separated by the baseline λ_i. To generate the output flux $\phi_o(x)$, a dipole is placed in the center and below the array plane pointing in the y direction. The recovery can be made with virtualy no errors[19], if the array is composed of an infinite number of gradiometers. However discretization and truncation of the infinite array can produce large recovery errors if the array is not designed properly.

The digital sampling of a continuous signal is a twofold problem: first the sampling frequency must be chosen and then the number of samples. An error in choosing the sampling frequency will lead to an overlap of the periods of the digital Fourier spectrum, this is called *aliasing*[16]. An abrupt truncation of the digital sequence will lead to a spectrum with ripples. As the recovery is made by taking the inverse Fourier transform of the output spatial frequency spectrum, an error in its calculation due to the discrete nature of the array, will lead to a wrong recovered value for the input field.

Let us assume that the model source is at a depth $d = 2\lambda_i$ and is detected by an squared 7x7 linear gradiometer array with an array parameter $a = \lambda_i$. The countour plot obtained by using the array output is shown in Fig. 1.

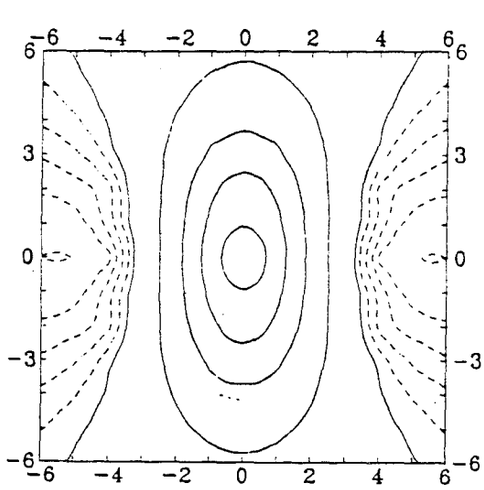

Fig.1 - Isovalue contour plot produced by the output of a 7x7 array of linear first order gradiometers with baseline λ_i and with an array parameter $a = \lambda_i$. The source is a current dipole at a depth of $d = 2\lambda_i$ ($\lambda_i = 2\,cm$).

Using the procedure described above, the recovered isofield plot can be seen in Fig. 2, which is quite similar to the well known current dipole pattern.

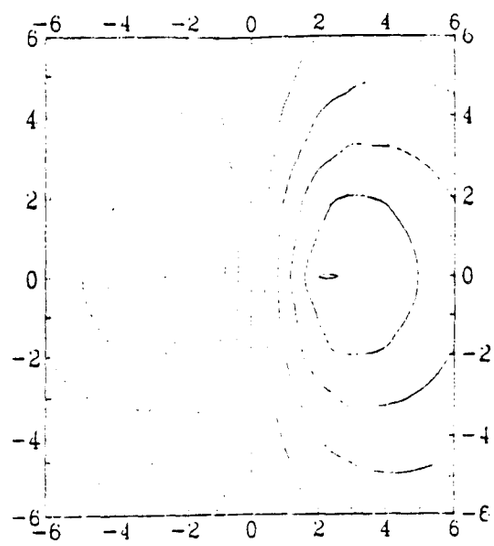

Fig.2 - Recovered isofield contour plot of a current dipole source at a depth of $d = 2\lambda_i$, detected by a 7x7 array of linear first order gradiometers with baseline λ_i with an array parameter $a = \lambda_i$ ($\lambda_i = 2\,cm$).

If the dipole source is at a smaller depth $d = \lambda_i$ and is detected by an array with a larger array parameter $a = 1.5\lambda_i$, the recovered isofield plot is shown in Fig. 3. Notice that the plot is largely distorted.

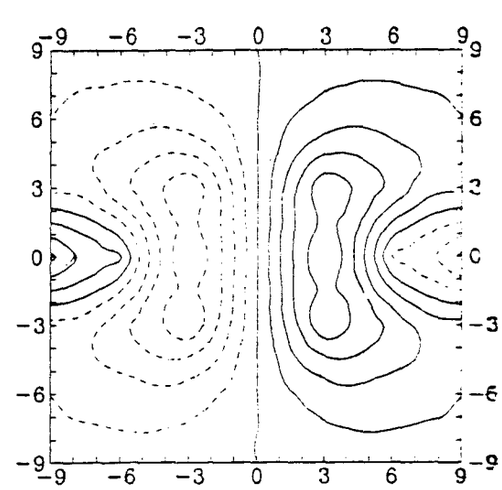

Fig.3 - Recovered isofield contour plot of a current dipole source at a depth $d = \lambda_i$, detected by a 7x7 array of linear first order gradiometers with baseline λ_i and with array parameter $a = 1.5\lambda_i$ ($\lambda_i = 2\,cm$).

More quantitative information can be obtained by inspecting the matrix whose elements are the percentage errors between the recovered input values and the ones that would be obtained if just single loop coils were used. Matrix (5) represents the errors at the 49 detecting positions of the first case, i.e. $d = 2\lambda_i$ and $a = \lambda_i$.

$$\begin{matrix} -12 & -9 & -6 & 0 & 6 & 9 & 12 \\ -11 & -9 & -5 & 0 & 5 & 9 & 11 \\ -11 & -8 & -4 & 0 & 4 & 8 & 11 \\ -11 & -7 & -3 & 0 & 3 & 7 & 10 \\ -11 & -8 & -4 & 0 & 4 & 8 & 11 \\ -11 & -9 & -5 & 0 & 5 & 9 & 11 \\ -12 & -9 & -6 & 0 & 6 & 9 & 12 \end{matrix} \quad (5)$$

As it can be seen, the error is larger for the sensors positioned more distant from the source. This is due to the truncation effect. If the line of sensors is far from the source the output flux between them will vary slowly in space. Thus, truncation will produce strong ripples in the frequency spectrum, since the signal will not be *finite* in that region of space. The zero line is because the gradiometer input and output for the symmetry axis of the dipole field is zero.

Matrix (6) represents the percentage errors at the 49 detecting positions of the second case, when the array parameter is larger than the source depth ($d = \lambda_s$ and $a = 1.5\,\lambda_s$).

$$\begin{matrix} -18 & -13 & -8 & 0 & 8 & 13 & 18 \\ -18 & -12 & -5 & 0 & 5 & 12 & 18 \\ -25 & -12 & -7 & 0 & 7 & 12 & 25 \\ -256 & -127 & -57 & 0 & 57 & 127 & 256 \\ -25 & -12 & -7 & 0 & 7 & 12 & 25 \\ -18 & -12 & -5 & 0 & 5 & 12 & 18 \\ -18 & -13 & -8 & 0 & 8 & 13 & 18 \end{matrix} \quad (6)$$

Notice the strong effect of aliasing in the center line of the array. Since the source is too close to that line of gradiometers, the spatial dependence will vary rapidly in space and the array parameter will be over the Nyquist period. A previous study of the spatial sampling of a current dipole field gave an upperbound for the sampling period of about 70% of the source depth[20]. As it was expected, the overlap of the periods in the digital spectrum produces bigger errors in the recovery than the ripples on it. The following line of sensors is more distant to the source, so the array parameter should be more close to the Nyquist period. However, comparing the errors with the ones in matrix (5) it can be seen that there is still some aliasing. The small intensity of the aliasing produces small errors in the recovery although bigger than in matrix (5) where there are errors due only to truncation.

The last example shows how truncation effect can be decreased. The source is at a depth $d = 2\,\lambda_s$ and it will be detected by an squared array of 11x11 gradiometers with the same array parameter of the first case $a = \lambda_s$. The percentage errors can be seen in matrix (7).

$$\begin{matrix} -21 & -17 & -12 & -11 & -9 & 0 & 9 & 10 & 12 & 17 & 21 \\ -20 & -17 & -11 & -9 & -7 & 0 & 7 & 9 & 10 & 16 & 20 \\ -20 & -16 & -9 & -7 & -5 & 0 & 5 & 7 & 9 & 16 & 20 \\ -20 & -16 & -7 & -5 & -3 & 0 & 3 & 5 & 7 & 16 & 20 \\ -20 & -15 & -6 & -4 & -2 & 0 & 3 & 3 & 6 & 15 & 20 \\ -20 & -14 & -6 & -3 & -2 & 0 & 2 & 3 & 6 & 14 & 20 \\ -20 & -15 & -6 & -4 & -3 & 0 & 3 & 3 & 6 & 15 & 20 \\ -20 & -16 & -7 & -5 & -3 & 0 & 3 & 5 & 7 & 16 & 20 \\ -20 & -16 & -9 & -7 & -5 & 0 & 5 & 7 & 9 & 16 & 20 \\ -20 & -17 & -11 & -9 & -7 & 0 & 7 & 9 & 10 & 16 & 20 \\ -21 & -17 & -12 & -11 & -9 & 0 & 9 & 10 & 12 & 17 & 21 \end{matrix} \quad (7)$$

The border positions have errors which are bigger than the ones in matrix (5), because the gradiometers at the borders of the 11x11 array are farther from the source than in the 7x7 array. Consequently, the signal will vary slower in space producing a stronger truncation effect. However by observing the errors at the positions corresponding to the borders of the first array, it can be seen that the worst error in matrix (5) was about 12% and at the same position in matrix (7) it has dropped to 9%.

In conclusion, by using a digital spatial filter model for the gradiometer it was possible to develop an algorithm to recover the input flux from the output measurements of a planar gradiometer array. With a properly designed array as in the first case the input flux was recovered with errors between 3% and 12%. This was enough to provide a contour plot quite similar to the one that would be obtained if the source was detected with a single loop coil array. Finally, by studing the correctness of the recovered values, it will be possible to design an array for an specific kind of measurement.

Acknowledgement

This work was partially supported by CNPq, FINEP and FAPERJ.

References

[1] S.J.Williamsom and L. Kaufman, "Biomagnetism," *J. Magn. Magn. Mat.*, vol. 22, pp. 129-201, 1981.

[2] J.E. Zimmerman and N.V. Frederick, "Miniature ultrasensitive magnetic gradiometer and its use in cardiography and other applications," *Appl. Phys. Lett.*, vol. 19, pp. 16-19, 1971.

[3] J.C. Gallop and B.W. Petley, "SQUIDs and their applications," *J. Phys. E: Sci. Instrum.*, vol. 9, pp.417-429, 1976.

[4] R. Ilmoniemi, R. Hari, K. Reinikainen, "A four-channel SQUID magnetometer for brain research," *Eletroencephalogr. Clin. Neurophysiol.*, vol. 58, pp. 467-473, 1984.

[5] G.L. Romani, R. Leoni and C. Salustri, "Multichannel instrumentation for biomagnetism," *H.D. Hahlbohn and H. Lubbig (eds) SQUID 85: Superconducting Quantum Interference Devices and their Applications*, Berlin-New York: Walter De Gruyter, 1985, pp.918-932.

[6] S.J. Williamson, M. Pelizzone, Y. Okada, L. Kaufman, D.B. Crum and J.R. Madsen, "Five channel SQUID installation for unshielded neuromagnetic measurements," *H. Wienberg, G. Stroink and T. Katila (eds) Biomagnetism: Theory and Applications*, New York: Pergammon Press, 1984, pp. 46-51.

[7] M.B. Ketchen, M. Goubau and J. Clarke, "Superconducting thin- film gradiometer," *J. Appl. Phys.*, vol. 49, pp. 4111-4116, 1978.

[8] J.A. Overweg and M.J. Peters, "The design of a system of adjustable superconducting plates for balancing a gradiometer," *Cryogenics*, vol. 18, pp.529-534, 1978.

[9] J. Vrba and J. McCubbin, "First-gradient Balancing of higher- order gradiometers," *Il Nuovo Cimento*, vol. 2, pp. 142-151, 1983.

[10] V.J. de Wall and T.M. Klapwijk, "Compact integrated dc SQUID gradiometer," *Appl. Phys. Lett.*, vol. 41, pp. 669-671, 1982.

[11] M.B. Ketchen, "Design of improved integradted thin-film planar dc SQUID gradiometers," *J. Appl. Phys.*, vol. 58, pp. 4322-4325, 1985.

[12] P. Carelli and R. Leoni, "Localization of biological sources with arrays of superconducting gradiometers," *J. Appl. Phys.*, vol. 59, pp. 645-650, 1986.

[13] A.C. Bruno, P. Costa Ribeiro, J.P. von der Weid and I.R. Eghrari, "Spatial Discrimination: an alternative approach," *H. Wienberg, G. Stroink and T. Katila (eds) Biomagnetism: Theory and Applications*, New York: Pergammon Press, 1984, pp. 67-72.

[14] A.C. Bruno, P. Costa Ribeiro, J.P. von der Weid and O.G. Symko, "Discrete spatial filtering with SQUID gradiometers in biomagnetism," *J. Appl. Phys.*, vol. 59, pp. 2584-2589, 1986.

[15] A.C. Bruno and P. Costa Ribeiro, "Digital filter design approach for SQUID gradiometers" *J. Appl. Phys.* vol. 63, pp. 2820-2823, 1988.

[16] M. Schwartz and L. Shaw, *Signal Processing*, Tokyo: McGraw-Hill, 1975, p. 68.

[17] P. Costa Ribeiro, A.C. Bruno, C.C. Paulsen and O.G. Symko, "Spatial Fourier transform method for evaluating SQUID gradiometers," *Rev. Sci. Instrum.*, vol. 58, pp. 1510-1513, 1987.

[18] William K. Pratt, *Digital Image Processing*, New York: John Willey, 1978.

[19] A.C. Bruno, A.V. Guida and P. Costa Ribeiro, "Planar gradiometer input signal recovery using a Fourier technique," *Procedings of the 6th International Conference on Biomagnetism*, Tokyo, 1987.

[20] G.L. Romani and R. Leoni, "Localization of cerebral sources by neuromagnetic measurements," *H. Wienberg, G. Stroink and T. Katila (eds) Biomagnetism: Theory and Applications*, New York: Pergammon Press, 1984, pp. 205-220.

ANEXO 10

SPATIAL FOURIER TECHNIQUE FOR CALIBRATING GRADIOMETERS

A.C. Bruno, C.S. Dolce, S.D. Soares and P. Costa Ribeiro
Departamento de Fisica, Pontificia Universidade Catolica
Caixa Postal 38071, Rio de Janeiro, 22453, RJ, Brasil

INTRODUCTION

One of the main features of the biomagnetic technique is the possibility to identify and locate sources of bioelectric activity with an uncertainty of a few millimeters. The use of multichannel systems not only eases this procedure shortening the time of the measurement session but also enables simultaneous measurement at different points in space, making possible the observation of non periodic phenomena. However, a multichannel system can introduce an important source of error in the localization result, if the calibration factor (field/voltage) of each channel is not measured with an extreme accuracy (Costa Ribeiro et al, 1988). The perspective of using planar gradiometers in Biomagnetism imposes further difficulties to adapt the calibration procedures normaly used for axial gradiometers. In this work we propose a very general calibration method valid for all kinds of gradiometers and arrays. It is based on a spatial Fourier technique and in the digital nature of the gradiometer sensor.

THE GRADIOMETER AS A DIGITAL DEVICE

The gradiometer samples in space the magnetic field generated by both signal and noise sources at the discrete locations corresponding to the position of each coil. The sampled field is weighted by the value of the respective coil area and the output is the addition and subtraction of the weighted fields. Being a digital device, the gradiometer has its spatial transfer function analogous to its time domain correspondent, the *moving average* filter. The transfer function $H(k)$ can be expressed as in the following equation:

$$H(k) = \sum_{i=1}^{N+1} A_i e^{-jki\lambda_s}, \tag{1}$$

where, N is the gradiometer order, A_i are the areas of the coils, k is the spatial frequency and λ_s the sampling period or baseline.

TRANSFER FUNCTION AND CALIBRATION

An experimental procedure has been designed to measure the spatial transfer function and this has been applied to different axial gradiometers (Bruno et al, 1988). It consists in moving a calibration coil along the gradiometer axis, calculating the

theoretical input and recording the measured output values for the successive coil positions. The gradiometer input is defined as the theoretical flux that is induced in the first gradiometer coil (*pick-up coil*) and the output is the mesured voltage values. Prior to taking the Fourier transforms of both series, the output voltages were converted into flux by using a conventional calibration procedure. The transfer function is the result of the division of the output by the input transforms.

However, we have realized that this procedure could be used to determine the calibration factor itself, since the output is a voltage readout v_{out} and the input is the theoretical flux ϕ_{in} calculated in Weber. The calibration factor can be withdrawn from the comparison between the experimental and theoretical transfer functions, by superposing them in the middle frequency range.

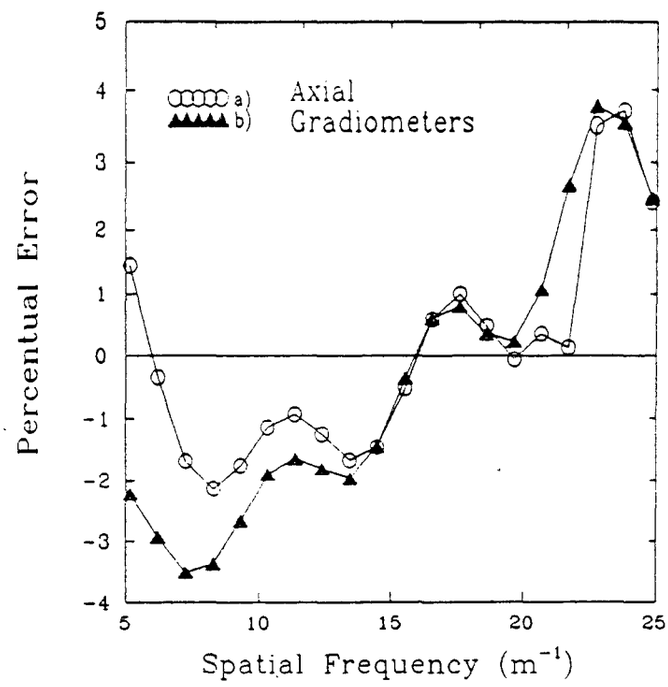

Fig. 1- Percentual error between theoretical and experimental transfer functions against the spatial frequency. Curves *a* and *b* correspond to axial 2nd order gradiometers with 1.5 *cm* diameter coils and 4 *cm* and 5 *cm* baselines respectively.

Curves *a* and *b* in Fig. 1 show the percentual difference between theoretical and experimental transfer functions for two axial 2nd order SQUID gradiometers in two different experiments and for calibration factors of $2.31 \cdot 10^{-8}$ and $2.32 \cdot 10^{-8}$ *Tesla/Volt* respectively. Gradiometer *a* has a 5 *cm* baseline and 1.5 *cm* diameter coils. Gradiometer *b* has a 4 *cm* baseline and 1.5 *cm* diameter coils. The calibration coil has a 32 *cm* diameter and was slipped axially over the dewar in steps of about 2 *cm* to an approximately equal distance of ~~10~~ baselines above and below the gradiometer. About 50 points were measured in both experiments and a spline routine was used before the Fourier process. The experimental transfer functions were evaluated in the frequency range between 0 and $30\,m^{-1}$ (Knuutila et al, 1987), and the fitting by the theoretical transfer function was made between 5 and $25\,m^{-1}$. As can be seen, the errors for different frequencies oscilate around zero having an average error of 0.1% and 0.4% respectively. Although the worst error of the two experiments reaches 3.7% the parameter that we should be concearned about is the average error. Standard

deviations of respectively 1.6% and 2.2% for curves a and b atest the reliability of the method.

Moreover, we have also realized that this procedure could be extremely useful for calibrating planar gradiometers, since this method does not depend on the gradiometer geometry. In this case it will be possible to have them calibrated in field units instead of the usual gradient units which do not seem to be adequate for clinical use.

For this purpose, a wound-wire first order planar gradiometer was built with a $2\,cm$ baseline and $1\,cm$ diameter coils. Fig. 2 displays the theoretical (dashed-line) and experimental (continuous-line) transfer functions. This transfer function was obtained by displacing the planar gradiometer along a line over a calibration coil of $80\,cm$ diameter at a distance of $15\,cm$ from its plane. It was taken about 100 measurements with a $1\,cm$ interval. The calibration coil was excited by a sinusoidal current. The gradiometer was wound with copper wire and its output was detected with a PAR 124-A lock-in amplifier.

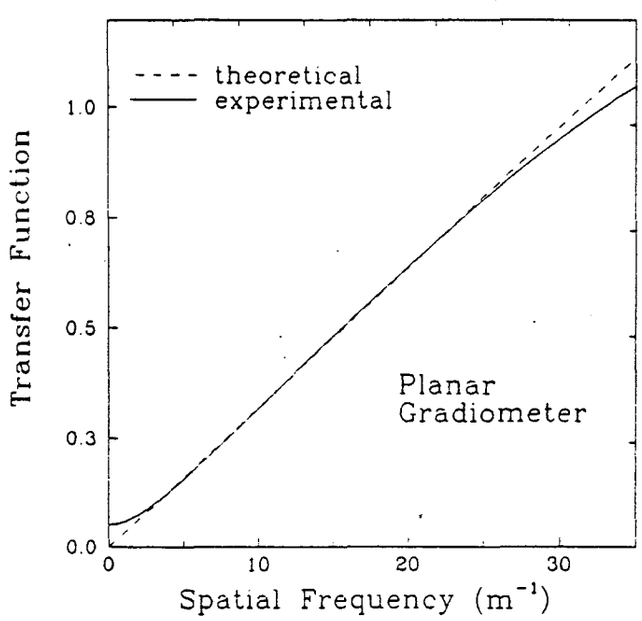

Fig. 2- Theoretical (dashed-line) and experimental (continuous-line) transfer functions of a planar first order gradiometer with $2\,cm$ baseline and $1\,cm$ diameter coils

Then, Fourier transforms of the input and output sequences were computed and the division of the output by the input transforms was performed. The calibration factor has been chosen by fitting, for the middle frequency range, the experimental transfer function by the theoretical one obtained by using eq. (1) and the gradiometer parameters. It was checked that for frequencies in the range of 5 to $25cm^{-1}$ the error oscilates around zero with a maximum amplitude of 2% . The average error was 0.5% and the standard deviation was 1%. Notice that for both planar and axial gradiometers we can have as much as 70% of the points in the experimental transfer functions coincident with the theoretical ones.

For planar gradiometer calibration or for array of axial gradiometers, where the gradiometers lie off the calibration coil axis, the theoretical input should be calculated by using the following expression :

$$B_z(x,y,z) = \frac{\mu_0}{4\pi} I \int_0^{2\pi} \frac{a\,(a - y\sin\theta - x\cos\theta)}{\left[x^2 + y^2 + z^2 + a^2 - 2a\,(x\,cos\theta + y\,sin\theta)\right]^{\frac{3}{2}}}\,d\theta$$

where I is the calibration coil current and a is the calibration coil radius.

It is worth noting that an advantage of this technique, besides its simplicity, is that in the frequency domain it is possible to graphically visualize, in the low frequency range, the unbalance effect, main source of errors when using large calibration coils. Also, imprecisions in positioning the calibration coil, major source of errors when using small calibration coils, appers only in the high frequency range. Due to this fact the fitting should be done in the middle frequency range. Finally it should be emphasized that when using a conventional method for calibrating gradiometer arrays with a large number of detecting sensors, the amount of work is the same as in the procedure above, since the calibration coil has to be displaced near each gradiometer.

ACKNOWLEDGEMENTS

We gratefully acknowledge P.J.E. Hübscher for his help in computing work.

REFERENCES

Costa Ribeiro P., Williamson S.J. and Kaufman L. (1988). SQUID arrays for simultaneous magnetic measuremnts: Calibration and source localizations performance. *IEEE Trans. Biomed. Eng.* **35** , 551-560.

Bruno A.C., Paulsen C.C., Symko O. and Costa Ribeiro P. (1988) Measurements of gradiometers' spatial Transfer Function. In: Atsumi,K., Kotani,M., Ueno,S., Katila,T. and Williamson,S.J., *Biomagnetism'87* Tokyo Denki University Press, 450-453.

Knuutila J., Ahlfors S., Ahonen A., Hallstron J. Kajola M., Lounasmaa O.V., Vilkman V. and Tesche C. (1987) A Large-Area Low Noise Seven-Channel DC SQUID Magnetometer for Brain Research. *Rev. Sci. Instrum.* **58** , 2145-2156.

ANEXO 11

FQSC

DESIGNING PLANAR GRADIOMETER ARRAYS : PRELIMINARY CONSIDERATIONS

A.C. Bruno and P. Costa Ribeiro
Departamento de Fisica, Pontificia Universidade Catolica,
Caixa Postal 38071, Rio de Janeiro, 22453, RJ, Brasil.

INTRODUCTION

A few years ago, when small scale multichannel systems (4 up to 7 channels) were built, a step forward was taken in biomagnetic measurements. The use of these systems shortened the time of measurement, allowing a more extensive source mapping and decreasing the risk of subject fatigue during the experiment. It is commonly said that the ultimate goal in this field is to build systems with a large number of detecting sensors, for instance 50 to 100 planar gradiometers. The purpose of this work is to begin a study on the design of these systems.

DESIGNING THE ARRAY

It will be discussed here some aspects of the array design: the array size and the number of gradiometers. The gradiometer coils' areas will be considered infinitely small because the analysis will be only on the sensor positioning. As the planar gradiometer is in linear shape, the study can be focused only on one array line, with the gradiometer orientation axis parallel to the array line. Finally it will be assumed that the source is under the center of the array.

The first thing to be done is to analyse the spatial properties of the most common model source used in Biomagnetism, the current dipole. Fig. 1 shows different gradiometers outputs $B_z(x)$ of the magnetic field generated by a current dipole, at a $3\,cm$ depth and immersed in a semi-infinite conducting media. The dipole is oriented in the y direction. Curves a), b) and c) are the outputs for a magnetometer, first order ($2\,cm$ total length) and second order ($2\,cm$ total length) planar gradiometers respectively.

The array size, that in this case corresponds to the length (L) of the line of gradiometers, can be obtained considering the total signal energy by using the Parseval's Theorem (Antoniou A., 1979 and Bruno A.C. et al., 1986). The total energy of the signal is proportional to:

$$E \propto \int_{-\infty}^{\infty} \mid B_z(x) \mid^2 \, dx. \tag{1}$$

To be able to maintain nearly the total energy when measuring the signal, the limits L of integral (2) should be chosen in a way that 99% of the total energy is still present,

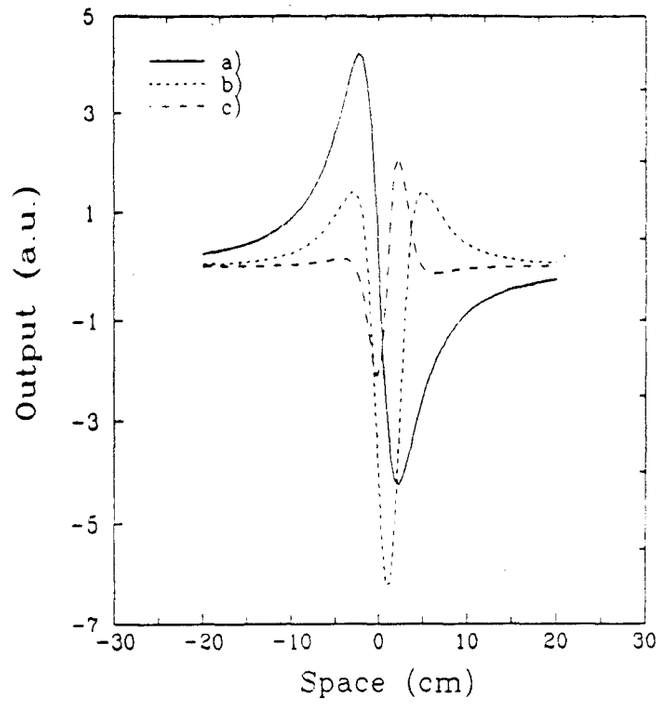

Fig. 1 - B_z versus x for a magnetometer a), first order b) and second order c) planar gradiometers with 2 cm total length, detecting a current dipole at a distance of 3 cm below the gradiometer.

$$99\% \int_{-\infty}^{\infty} \mid B_z(x) \mid^2 \, dx = \int_{-L/2}^{L/2} \mid B_z(x) \mid^2 \, dx. \tag{2}$$

For the signals depicted in Fig. 1 the line lengths L that correspond to 99% of the total energy are 32 cm, 16 cm and 12 cm for the magnetometer, first and second order gradiometers respectively. For signals due to a deeper source of 7 cm, the values for L are 52 cm, 30 cm and 20 cm respectively. When building such array, one should consider the largest length. As one can see, the size of a planar gradiometer array can be smaller than the size of a magnetometer array. It also can be noticed that as the gradiometer order increases, the array size decreases.

On a first approach, a simple way to determine the array sampling period is to estimate the highest frequency component of the signal, investigating the smallest distance P between nearby peaks and valleys of the signal. This distance is related to the highest frequency component. The distance between a peak and a valley represents half of the period. Hence, the highest frequency is $F = 1/2P$. One may choose the array sampling frequency, obeying the Nyquist theorem, as $2.5F$ or, equivalently, the sampling period as $0.8P$. Inspecting Fig.1 one can see that the smallest distances between peaks and valleys are 4.5 cm, 3.7 cm and 2.5 cm for the magnetometer, first order and second order gradiometers respectively. Thus, the array sampling period should be 3.6 cm, 3.0 cm and 2.0 cm.

Another way to estimate the higher frequency component of the signal is to calculate its spatial Fourier transform and this has already been done for magnetometers (Romani et al., 1985). Fig. 2 shows spatial Fourier transforms of the output of a magnetometer, first and second order planar gradiometers due to a current dipole at a 3 cm depth.

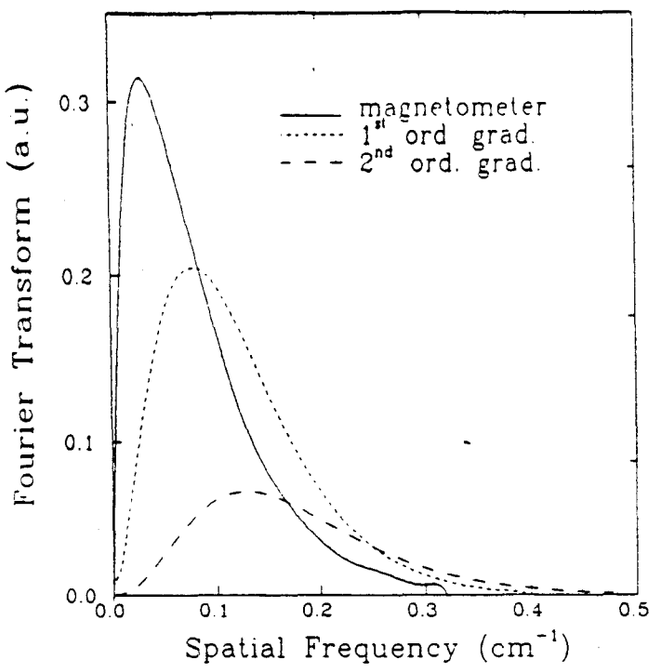

Fig. 2 - Fourier Transforms $\mathcal{B}(k)$ for a current dipole at a 3 cm depth detected by a magnetometer, first order and second order planar gradiometers.

By using the Parseval's theorem applied to the frequency domain:

$$E \propto \frac{1}{2\pi} \int_{-\infty}^{\infty} \mid \mathcal{B}(k) \mid^2 \, dk, \tag{3}$$

and calculating the following equation:

$$99\% \int_{-\infty}^{\infty} \mid \mathcal{B}(k) \mid^2 \, dk = \int_{-F}^{F} \mid \mathcal{B}(k) \mid^2 \, dk, \tag{4}$$

the magnetometer, first and second order planar gradiometers have the following values for the maximum frequency $F\,(cm^{-1})$: 0.16, 0.24 and 0.32 respectively. Applying the Nyquist theorem as $2.5F$, the sampling periods should be 2.5 cm, 1.7 cm and 1.2 cm for arrays of magnetometers, first and second order planar gradioemeters respectively. By comparing the values obtained in the first method, one should use these values since they are smaller. In this case a deeper source do not need to be considered since it will not generate higher frequency components.

Notice that since the gradiometer sensor has a 2 cm length it will be difficult to build an array with first or second order planar gradiometers for detecting a 3 cm depth source, since it will require a spacing less than 2 cm between gradiometers. However, if one take into account the inner-outer dewar distance of about 1 cm and the dewar-subject distance of about 0.5 cm, the minimum distance between gradiometer and source could increase to about 4.5 cm. In this case the distance between gradiometers should be 2.5 cm for first order and 1.7 cm for second order planar gradiometers. If the coil's area is taken into account, first order gradioemters could overlap again. However, taking into account the coil area leads to a spatial dependence varing more slowly in space and this will represent a smaller F and a larger distance between gradiometers. For first order planar gradiometers the array line should be 30 cm long

having 12 gradiometers with their centers separated by a 2.5 *cm* distance. It is worth noting that a deep source imposes a minimum limit to the array size and a shallow source imposes a maximum limit to the distance between gradiometers.

The correctness of this design is made, by using an algorithm to recover the gradiometer original input signal from the array output measurements (Bruno A.C. et al., 1989). In this test the dipole is at a 4.5 *cm* depth and it is detected by an array line of first order gradiometers as designed above. The result of the recovery algorithm at the gradiometer positions (circles) compared to the theoretical field values (continuous-line) can be seen in Fig. 3.

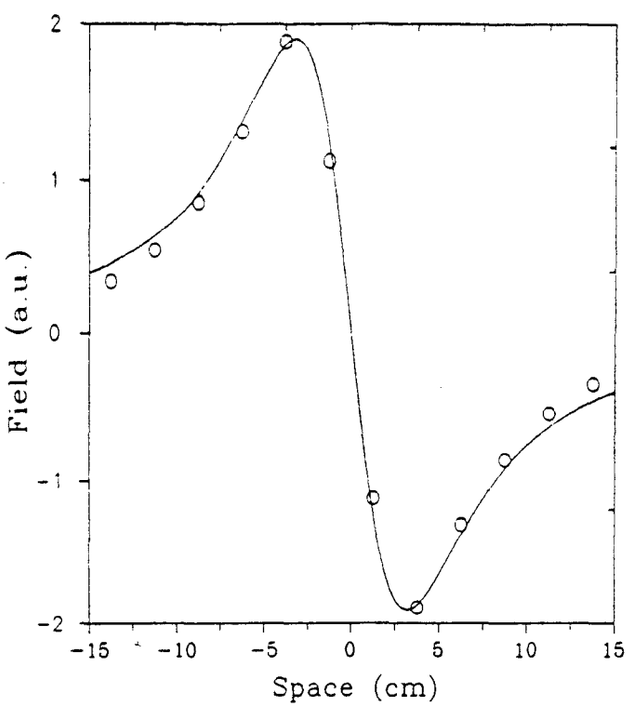

Fig. 3 - Input signal recovered (circles) from the array line output measurements compared to the theoretical (continuous-line) dipole field. The array line has a 30 *cm* length and 12 first order gradiometers with a 2 *cm* baseline separeted by 2.5 *cm*.

REFERENCES

Antoniou A. (1979) *Digital Filters: Analysis and Design* , McGraw-Hill, p.139.

Bruno A.C., Costa Ribeiro P., Weid J.P. and Symko O.G. (1986) Discrete spatial filtering with SQUID gradiometers in biomagnetism. *J. Appl. Phys* **59** pp. 2584-2589.

Romani G.L. and Leoni R. (1985) Localization of cerebral sources by neuromagnetic measurements. In: *Biomagnetism: Applicaton & Theory*, eds. Weinberg,H., Stroink,G., Katila, K., Pergamon Press, pp. 205-220.

Bruno A.C. and Costa Ribeiro P. (1989) Spatial Deconvolution Algorithm for Superconducting Planar Gradiometer Arrays. *IEEE Trans. Mags.* **25** pp. 1216-1220.

ANEXO 12

Spatial Fourier calibration method for multichannel SQUID magnetometers

A.C. Bruno and P. Costa Ribeiro

Departamento de Fisica, Pontificia Universidade Catolica do Rio de Janeiro

Rua Marques de São Vicente 225, Rio de Janeiro, 22453, RJ, Brasil

Abstract

When using multichannel SQUID magnetometers for biomagnetic applications, the correct measurement of the Tesla/Volt calibration factor of each channel is of extreme importance, in order to avoid gross errors when analysing the results. In this work we propose a general calibration method valid for all kinds of gradiometer arrays. When tested, this method provided calibration factors with accuracies ranging from 0.3 to 0.8 percent. It is based on a spatial Fourier technique and on the fact that the gradiometer acts as a discrete spatial filter.

I. Introduction

The measurement of biomagnetic fields can provide important information on the location of electrical activity in the human heart and brain. Biomagnetic measurements can be useful, for instance, in locating epileptic foci in the brain[1] and abnormal pathways in cardiac arrhythmias[2]. The measurement is made by displacing a SQUID magnetometer over the chest or scalp and recording the measured field for different positions. In the past few years multichannel magnetometers were introduced, consisting of up to 30 channels[3-5] . The use of multichannel systems allowing simultaneous measurements at different positions decreases the time of the measuring session, increasing its reliability, and also makes possible the observation of non periodic phenomena. However, when using these systems, the Tesla/Volt calibration factor of each channel must be measured with extreme accuracy in order to avoid errors in the localization result[6].

A fundamental part of a biomagnetic magnetometer system is the sensing coil that picks up the measuring field and couples it to the SQUID by means of a superconducting flux transformer. In order to reduce the magnetic noise due to the environment, the sensing coil is designed in a gradiometric configuration[7]. The so called axial gradiometer consists of a set of coils, wound in a proper polarity with a specific number of turns and having typically a 4-7 cm distance between adjacent coils[8] (baseline). This way, the spatially uniform signals of distant sources will be drastically attenuated and the near biomagnetic signal will not, because of its proximity to one of the gradiometer coils.

The SQUID provides an output voltage that varies linearly with the magnetic field in the gradiometer over several decades of frequency. There are several ways to obtain the Tesla/Volt calibration factor for one channel magnetometers. The two most reliable follow. The first is: slipping a calibration coil (about 6 cm diameter)

around the tail of the cryogenic dewar containing the SQUID system, and moving it until a maximum output voltage from the SQUID is obtained. From the geometry of the calibration coil and gradiometer, the mutual inductance can be calculated[9]. The product of the mutual inductance by the current in the calibration coil is the magnetic flux applied to the gradiometer. Dividing this flux by the gradiometer first coil area, the field that corresponds to the SQUID output voltage is obtained. The second is: using a small calibration coil (about 5 mm diameter) axialy placed at about 20 cm distance from the first gradiometer coil, in a way that we can approximate it by a magnetic dipole. Computing the flux in the gradiometer coils and dividing it by the gradiometer first coil area, the field that corresponds to the output voltage is obtained. Both methods, in practice, can give an accuracy of about 10 percent, and that is enough for one channel systems since they produce the same error in all the measuring positions, thereby not affecting the localization result. However, when using a multichannel system different calibration errors in different channels correspond to different errors in different positions, therefore spoiling the measurement[6].

Two calibration schemes for multichannel systems have been proposed recently. Both seem to produce good results, but with some drawbacks. The first[6] relies on a large coil assembly and can only be applied to second order gradiometers with a specific level of performance. The second[10] uses an array of small coils, requiring a great deal of hardware and software for processing.

In this paper we describe a calibration procedure based on a spatial Fourier technique that can be used to calibrate multichannel SQUID systems, due to the precision attained. The procedure is tested empirically by calibrating various one channel systems. The calibration of multichannel systems is also discussed in order to provide parameters to be used experimentally.

SERVIÇO DE BIBLIOTECA E INFORMAÇÃO - IFOSC
FÍSICA

II. Transfer function and calibration

In order to understand how the calibration procedure works the gradiometer must be regarded as a spatial filter[11-12] . A gradiometer samples in space the magnetic field produced by both signal and noise sources at the discrete coil positions. The sampled field is weighed by the respective number of turns of each coil, and the output is additions and subtractions of the weighed field. The gradiometer has its spatial transfer function analogous to its time domain correspondent, the *moving average* filter[13]. The transfer function $H(k)$ can be expressed as in the following equation:

$$H(k) = \sum_{i=1}^{N+1} n_i e^{-jki\lambda_s}, \tag{1}$$

where N is the gradiometer order, n_i is the number of turns of coil i, k is the spatial frequency and λ_s is the gradiometer baseline. It is assumed that the gradiometer has an unity area and the field is distributed uniformely all over it.

An experimental procedure has been designed to measure the spatial transfer function and this has been applied to axial gradiometers[14]. It consists in dividing the Fourier transform of an output signal by the Fourier transform of the corresponding input signal. The signals can be obtained by moving a calibration coil along the gradiometer axis, calculating the theoretical input for each position and recording the measured output values. The gradiometer input signal is defined as the field applied to the first gradiometer coil and its Fouier transform is given by:

$$\mathcal{B}(k) = \frac{\mu_0}{2} I \int_{z_b}^{z_a} \frac{a^2}{(a^2+z^2)^{\frac{3}{2}}} e^{-jkz}\, dz \tag{2}$$

where I is the calibration coil current, a is the calibration coil radius and z_b and z_a are respectively the distance limits below and above the gradiometer first coil.

The corresponding output signal is the measured SQUID voltage for each cali-

bration coil position and its Fourier transform is given by[15]:

$$\mathcal{V}(k) = \lambda \sum_{m=0}^{M} v_m \, e^{-jkm\lambda}, \tag{3}$$

where v_m is the SQUID output voltage corresponding to the discrete $m\lambda$ position and λ is the distance between each calibration coil position.

Since the spatial transfer function has no dimension, the output voltages are converted into field by multiplying them by the Tesla/Volt calibration factor. The experimental transfer function $H_{exp}(k)$ is then found by dividing Eq. (3) by Eq. (2):

$$H_{exp}(k) = \frac{C\,\mathcal{V}(k)}{\mathcal{B}(k)} \tag{4}$$

where C is the Tesla/Volt calibration factor.

Figure 1 shows the theoretical (squares) and experimental (continuous line) transfer functions of a balanced[8] second order gradiometer consisting of 4,-8, 4 turns with a 1.5 cm diameter having a 4 cm baseline. The transfer functions were evaluated in a bandwidth[4] of 0 and 30 m^{-1}. The calibration factor was obtained by using the procedure based on the mutual inductance explained in the introduction and is 24 pT/mV. Figure 2 shows the theoretical (squares) and experimental (continuous line) transfer functions of a highly unbalanced[8] second order gradiometer consisting of 1,-2, 1 turns with a 1.5 cm diameter having a 5 cm baseline. Using the same procedure, the calibration factor found was 64 pT/mV. The SQUID used is RF biased and it is a commercial one[16].

We have realized however, that this procedure of finding the transfer function could also be used to determine the calibration factor itself, omitting the voltage-to-field convertion and obtaining an experimental transfer function with a Volt/Tesla dimension. Fitting the amplitude of the experimental transfer function by the amplitude of the theoretical one, within a certain bandwidth, the calibration factor C

in Tesla/Volt can be found. The fitting procedure consists simply in finding C that minimizes the average error between the experimental and theoretical transfer functions:

$$C = \frac{k_{bw}}{\int_0^{k_{bw}} \frac{|H_{exp}(k)|}{|H(k)|} dk} \tag{5}$$

where k_{bw} is the fitting bandwidth.

The lack of precision found in the conventional calibration methods, resides basicaly in the fact that the exact position of the gradiometer inside the cryogenic dewar is not known but for an error of a few milimeters[6]. An intrinsic advantage of this Fourier method concerns this point precisely. A fundamental property of the Fourier formalism transforms any constant spatial shift in the space domain, into a phase shift in the frequency domain. As the fit is made by using the amplitude values only, the inaccuracy in determining the exact gradiometer position does not influence on the calibration precision.

III. Data acquisition

Since the data has to be measured in discrete points corresponding to different calibration coil positions, one has to be concerned about the sampling period λ and the number of points N to be recorded. It is shown in Fig. 3 the sharpest output among all gradiometers tested. A simple way to determine the sampling period is to estimate the highest frequency component of the signal, investigating the smallest distance P between nearby peak and valley. This distance may be due to the highest frequency component. The distance between the peak and valley represents half of the period. Hence, the highest frequency is $F = 1/2P$. One may choose the sampling frequency, obeying the Nyquist theorem, as $2.5F$ or, equivalently, the sampling period λ as $0.8P$. One can see that the smallest distance between the peak and valley in this

case is 14 cm. The sampling period λ chosen is 10 cm and it should be considered as a tentative one. The number of points is then chosen in a way that the amplitudes of positions far from the gradiometer correspond to less than 1 percent of the maximum amplitude.

In order to check if the sampling period chosen above is the correct one, we must compute the Fourier spectrum according to Eq. (3). We then decrease λ, increasing the number of recording positions and repeat the calculation. If the spectrum does not change the first estimate is correct. Otherwise the sampling period must be decreased until the new Fourier spectrum is equal to the preceeding one. It is shown in Fig. 4 the Fourier transforms of the SQUID output voltages for the gradiometer which transfer function is shown in Fig. 1. The big-dashed line corresponds to a λ = 10 cm and 11 measurements. The small-dashed line corresponds to λ = 5 cm and 23 measurements, which is equal to the continous line spectrum that was obtained when λ = 2.5 cm and 47 measurements were used. This shows that, λ = 5 cm and 21 recording positions are enough to represent accurately this output. As this is the gradiometer with the smallest baseline and hence providing the sharpest output, the same settings can be used for all others.

Another important issue that must be discussed, is the the precision of the calibration coil positioning system and its relationship with the number of measuring positions. Although the method is insensitive to any constant shift in the gradiometer position, care should be taken in the system that will hold and position the calibration coil, since it will affect the sampling period accuracy. Figure 5 shows the calibration results versus the fitting bandwidth percent of various simulated measurements with different accuracies in λ, where 100 percent corresponds to a fitting between 0 and 30 m^{-1}, 80 percent corresponds to a fitting between 3 and 27 m^{-1}, 60 percent corresponds to a fitting between 6 and 24 m^{-1} and so on. Since it is a simulation, the

calibration factor should be 1 for a positioning system with no errors. The curve with squares is the result of a simulated measurement with 25 measuring positions and λ = 5 cm $\pm$ 1 cm. It provides an average calibration error of about 2.5 percent. If by any reason, the experimental setup is constrained to such a low precision, the overall error performance could be improved by decreasing the sampling period to 2.5 cm and increasing the number of measuring positions to 50. The calibtarion error drops to less than 1 percent (curve with triangles). The curve with circles is the calibration obtained by using 25 measuring positions but having λ = 5 cm $\pm$ 1 mm. The average calibration error in this case is about 0.5 percent. Finally the curve with diamonds represents the calibration obtained by using the same number of positions used previously but having λ = 5 cm $\pm$ 0.5 mm. The calibration error drops to about 0.25 percent. Our positioning system was built so as to have an accuracy better than 1 mm.

IV. Experimental results

As it can be noticed in Fig. 2, the unbalance alters the low frequency portion of the transfer function spectrum[14]. Thus, one should be aware of this fact in order to choose properly the fitting bandwidth. We have used a calibration coil diameter (29 cm) just large enough to slip over the cryogenic dewar. As it was said in the end of the first paragraph in the last section, the spatial signal must be finite in order to avoid the aliasing effect. This is accomplished by sampling the output signal until the amplitude is less than, say 1 percent of the maximum output signal. For instance, in Fig. 3 v_0 = 1.4 mV corresponds to a distance of 48 cm below the first gradiometer coil, v_{23} = 1.4 mv corresponds to 62 cm above it and the maximum aplitude value v_{12} = 216 mV corresponds to a distance 7 cm above the first gradiometer coil. It should be stressed that this must also be applied to the input signal. Since the input signal

is the theoretical field applied to the first gradiometer coil, its amplitude decays less rapidly then the output signal. If we compute the input Fourier integral by using the same limits used to compute the output Fourier integral, in this case -48 and 62 cm, the result is shown in Fig. 6 curve *(b)* . It shows the calibration of the second order gradiometer which transfer fuction is shown in Fig. 1. Fitting in 65 percent of the bandwidth, i.e. between 5.5 and 24.5 m^{-1}, gives a calibration factor of 26.80 pT/mV. If the fitting is made between 12 and 18 m^{-1} (20 percent bandwidth) the calibration factor is 27.47 pT/mV, which is about 2.5 percent different. This problem can be solved simply extending the limits of the input Fourier integral. Curve *(a)* in Fig. 6 shows the calibration obtained by extending the theoretical input Fourier integral limits from -500 to 500 cm. The calibration factor can be chosen as 27.10 pT/mV with a 0.3 percent spread in their values, even if the fitting bandwidth varies from 75 percent to 20 percent.

If the gradiometer is highly unbalanced, the method can still be applied with no loss of precision as it is shown in Fig. 7. These are the calibration results for various fitting bandwidths for the gradiometer which transfer function is shown in Fig. 2. As the fitting percent is increased, the calibration result diverges. This is because of the high degree of unbalance of this gradiometer.. However fitting in less than 50 percent of the entire bandwidth the calibration factor converges to 64.75 pT/mV with a 0.3 percent error, because the fitting is made in a portion of the transfer function spectrum far from the disturbances caused by the unbalancing.

Figure 8 shows the calibration results of a second order gradiometer that consists of 1,-2, 1 turns with a 3.0 cm diameter having a 5 cm baseline. Fitting in 30 percent of the bandwidth gives a calibration factor of 23.09 pT/mV, fitting in 55 percent of the bandwidth gives 22.99 pT/mV and in 80 percent of the bandwidth gives 23.04 mV/pT. The largest difference is 0.4 percent. Figure 9 shows the calibration results

of a third order gradiometer consisting of 2,-3, 2, -1 turns with a 3.0 cm diameter having a 3.1, 11.5 and 5.6 cm baselines[17]. These measurements were made with an old positioning system that has a displacement accuracy of about 1 cm. Although balanced, the higher frequency errors caused by the displacement inacuracy force the calibration to diverge for fittings in a bandwidth higher than 50 percent of the total bandwidth. A sampling period of 2.5 cm was used and 50 measurements were made. However for fittings made in the central part of the spectrum, i.e. between 8 and 22 m^{-1} the calibration factor converges to 14.26 mV/pT with a 0.8 percent error.

V. Multichannel calibration

A multichannel system consists in placing together several SQUID magnetometers in order to measure the magnetic field simultaneously at various locations. Usually there is a rotational symmetry in such systems[4-5]. The calibration procedure remains the same, i.e. displaces axially the calibration coil and measures the SQUID voltages for several positions. The difference is only in the input field calculation, since now the gradiometers are placed off the calibration coil axis. The expression used to compute an off axis field of a circular coil is:

$$B_z(x,y,z) = \frac{\mu_0}{4\pi} I \int_0^{2\pi} \frac{a\,(a - y\,\sin\theta - x\,\cos\theta)}{[x^2 + y^2 + z^2 + a^2 - 2a\,(x\,cos\theta + y\,sin\theta)]^{\frac{3}{2}}}\,d\theta \qquad (6)$$

where I is the calibration coil current, a is the calibration coil radius and x and y are the coordinates of the gradiometer center.

Another important issue concerns the calibration coil diameter. Usually the cryogenic dewar that contains a multichannel system is larger than the one used for one channel systems. Since one has to slip the calibration coil over the system, the coil diameter must also be larger. If the calibration coil is too large, its field will decay less rapidly against the distance. So, one has to check if the output at

a reasonable distance from the gradiometer is small enough, if compared with the maximum output. This is necessary to avoid the aliasing effect. The factor between maximum and minimum values we used in the above mentioned experiments was about 150. Imagine a four channel system with second order gradiometers with 4, -8, 4 turns having a 4 cm baseline, positioned at the corners of a 2 cm square. The dewar usually used to hold this system has typically an external diameter of 33 cm. Assuming that we will use a calibration coil with a 35 cm diameter, if we measure from -60 to 53 cm below and above the gradiometer first coil, we will have a rate of about 150 between maximum and minimum outputs. In order to avoid the aliasing effect, it is shown in Fig. 10 up to which distance below the gradiometer first coil one has to measure, against the calibration coil size, for different off axis gradiometer positions $d = \sqrt{x^2 + y^2}$.

In the case of multichannel systems used for brain research, usually the gradiometers are tilted in order to describe approximatelly the head shape. Thus, prior to compute the Fourier transform, the input field given by Eq. (6) should be multiplied by the cosine of the tilting angle of each gradiometer.

VI. Conclusion

A Fourier method to calibrate multichannel SQUID systems was presented. One of the main properties of this method is that the gradiometer position inside the cryogenic dewar does not need to be known precisely. From the experimental measurements we can conclude that even being highly unbalanced or if the experiment is performed with a non accurate calibration coil positioning system, a good value for the fitting bandwidth is 50 percent. This corresponds to fit the experimental transfer function by the theoretical one between 8 and 22 m^{-1}. The assumption that the field is distributed uniformely over the gradiometer's area, did not seem to affect the

precision of the results, since the calibration errors obtained in the simulations are in the same range of the experimental ones. The best result attained in the experiments has a 0.3 percent accuracy, the worst, 0.8 percent. These figures entitle this method to be used to calibrate multichannel SQUID systems.

REFERENCES

[1] D.S. Barth, W. Sutherling, and J. Beatty, Science, **226**, 855 (1984).

[2] P. Costa Ribeiro, A.C. Bruno, E. Parente Ribeiro,J.S. do Carmo, E. Costa MOnteiro and A. Fonseca Costa, *Advances on Biomagnetism,* edited by S.J. Williamson (Pergamon, New York, 1990) in press.

[3] R. Ilmoniemi, R. Har, K. Reinikainen, Electroencephalogr. Clin. Neurophysiol. **58**, 467 (1984).

[4] J. Knuutila, S. Ahlfors, A. Ahonen, J. Hallstron, M. Kajola, O.V. Lounasmaa, V. Vilkman, and C. Tesche, Rev. Sci. Instrum. **58**, 2145 (1987).

[5] H.E. Hoenig, G. Daalmans, W. Folberth, H. Reichenberger, S. Schneider, and H. Seifert, Cryogenics **29**, 809 (1989).

[6] P. Costa Ribeiro, S.J. Williamson, and L. Kaufman, IEEE Trans. Biomed. Eng. **BME-35**, 551 (1988).

[7] J.E. Zimmerman and N.V. Frederick, Appl. Phys. Lett. **18**, 16 (1971).

[8] G.L. Romani, S.J. Williamson, and L. Kaufman, Rev. Sci. Instrum. **53**, 1815 (1982).

[9] F.W. Grover, *Inductance Calculations,* Dover, New York (1962).

[10] D.S. Buchanan and D.N. Paulson, *Advances on Biomagnetism,* edited by S.J. Williamson (Pergamon, New York, 1990) in press.

[11] A.C. Bruno, P. Costa Ribeiro, J.P. Weid, and O.G. Symko, J. Appl. Phys. **59**, 2584 (1986).

[12] A.C. Bruno and P. Costa Ribeiro, J. Appl. Phys. **63**, 2820 (1988).

SERVIÇO DE BIBLIOTECA E INFORMAÇÃO - IFQSC
FÍSICA

[13] M. Schwartz and L. Shaw, *Signal Processing,* (McGraw-Hill, Tokyo, 1975).

[14] P. Costa Ribeiro, A.C. Bruno, C.C. Paulsen, and O.G. Symko, Rev. Sci. Instrum. **58**, 1510 (1987).

[15] A. Antoniou, *Digital Filters Analysis and Design,* (McGraw-Hill, New York, 1979).

[16] Biomagnetic Technologies, Inc. 4174 Sorrento Valley Blvd., San Diego, CA 92121.

[17] A.C. Bruno and P. Costa Ribeiro, Cryogenics **23**, 346 (1983).

Figure captions

Fig. 1 - Theoretical (squares) and experimental (continuous line) transfer function amplitudes of a balanced second order gradiometer consisting of 4,-8, 4 turns with a 1.5 cm diameter having a 4 cm baseline. The calibration factor was obtained by using the procedure based on the mutual inductance it is 24 pT/mV.

Fig. 2 - Theoretical (squares) and experimental (continuous line) transfer function amplitudes of a unbalanced second order gradiometer consisting of 1,-2, 1·turns with a 1.5 cm diameter having a 5 cm baseline. The calibration factor was obtained by using the procedure based on the mutual inductance and it is 64 pT/mV.

Fig. 3 - Output voltages of the SQUID electronics of a second order gradiometer for various positions of the calibration coil. The current in the calibration coil is 8 mA.

Fig. 4 - Fourier transforms of the SQUID output for various sampling periods λ of the calibration coil. The gradiometer used is the same of Fig. 1.

Fig. 5 - Calibration simulation for different accuracies of the calibration coil sampling period λ. Curve with squares corresponds to 25 measuring positions and λ = 5 cm $\pm$ 1 cm. Curve with circles corresponds to 50 measuring positions and λ = 2.5 cm $\pm$ 1 cm. Curve with triangles corresponds to 25 measuring positions and λ = 5 cm $\pm$ 1 mm. Curve with diamonds corresponds to 25 measuring positions and λ = 5 cm $\pm$ 0.5 mm. The continuous line corresponds to a sampling period with no errors.

Fig. 6 - Calibration curves of a balanced second order gradiometer consisting of 4, -8, 4 turns, with 1.5 cm diameter having a 4 cm baseline. The dashed line was obtained by using the input Fourier transform limits between -48 to 62 cm, taking the position of the first coil as the origin. The continuous line was obtained by using the input Fourier transform limits between -500 to 500 cm.

Fig. 7 - Calibration curve of a unbalanced second order gradiometer consisting of 1,-2, 1 turns with a 1.5 cm diameter having a 5 cm baseline. The dashed lines corresponds to upper and lower limits respectively 64.65 mV/pT and 64.85 mV/pT.

Fig. 8 - Calibration curve of a balanced second order gradiometer consisting of 1, -2, 1 turns, with 3.0 cm diameter having a 5 cm baseline.

Fig. 9 - Calibration curve of a balanced third order gradiometer consisting of 2,-3, 2,-1 turns with a 3.0 cm diameter having baselines 3.1, 11.5, 5.4 cm. The dashed lines corresponds to upper and lower limits respectively 14.32 mV/pT and 14.20 mV/pT.

Fig. 10 - Distance limits from the gradiometer first coil against the calibration coil diameter, that must be observed in order to avoid the aliasing effect when computing the Fourier transform of the output of a second order gradiometer having a 4 cm baseline. $d = \sqrt{x^2 + y^2}$ corresponds to different off axis positions.

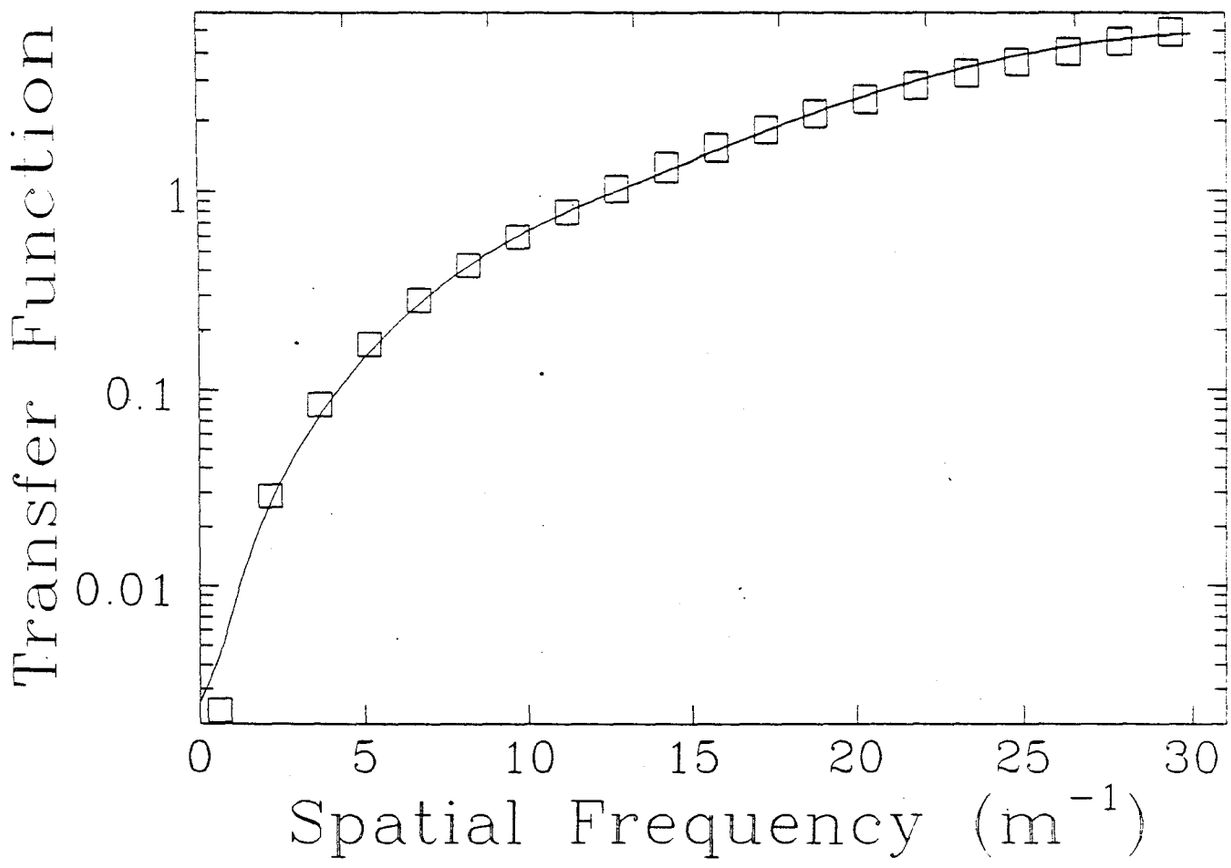
Transfer Function
1
0.1
0.01
0
5
10
15
20
25
30
Spatial Frequency (m^{-1})

FIG. 1

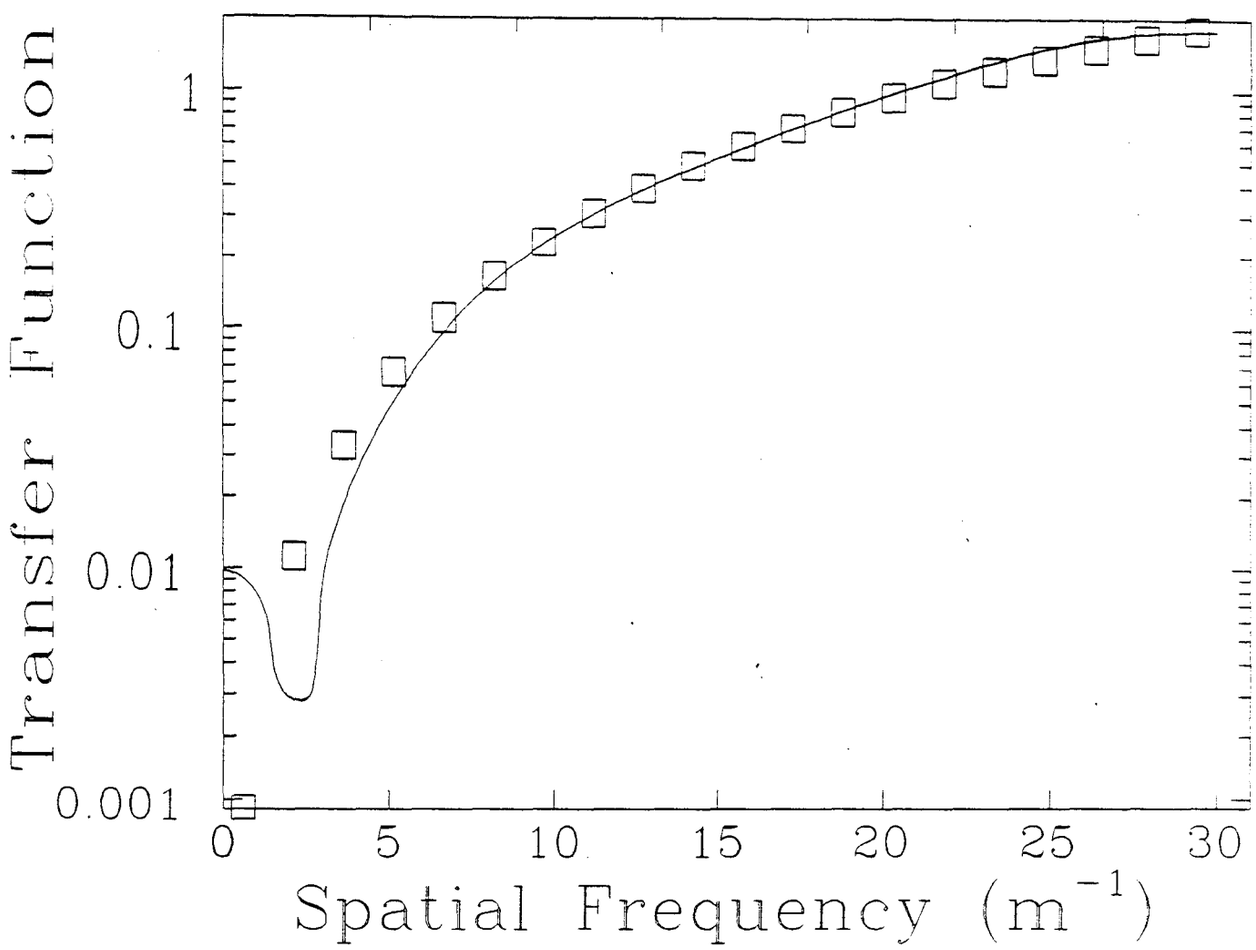
Transfer Function
1
0.1
0.01
0.001
0
5
10
15
20
25
30
Spatial Frequency (m^{-1})

FIG. 2

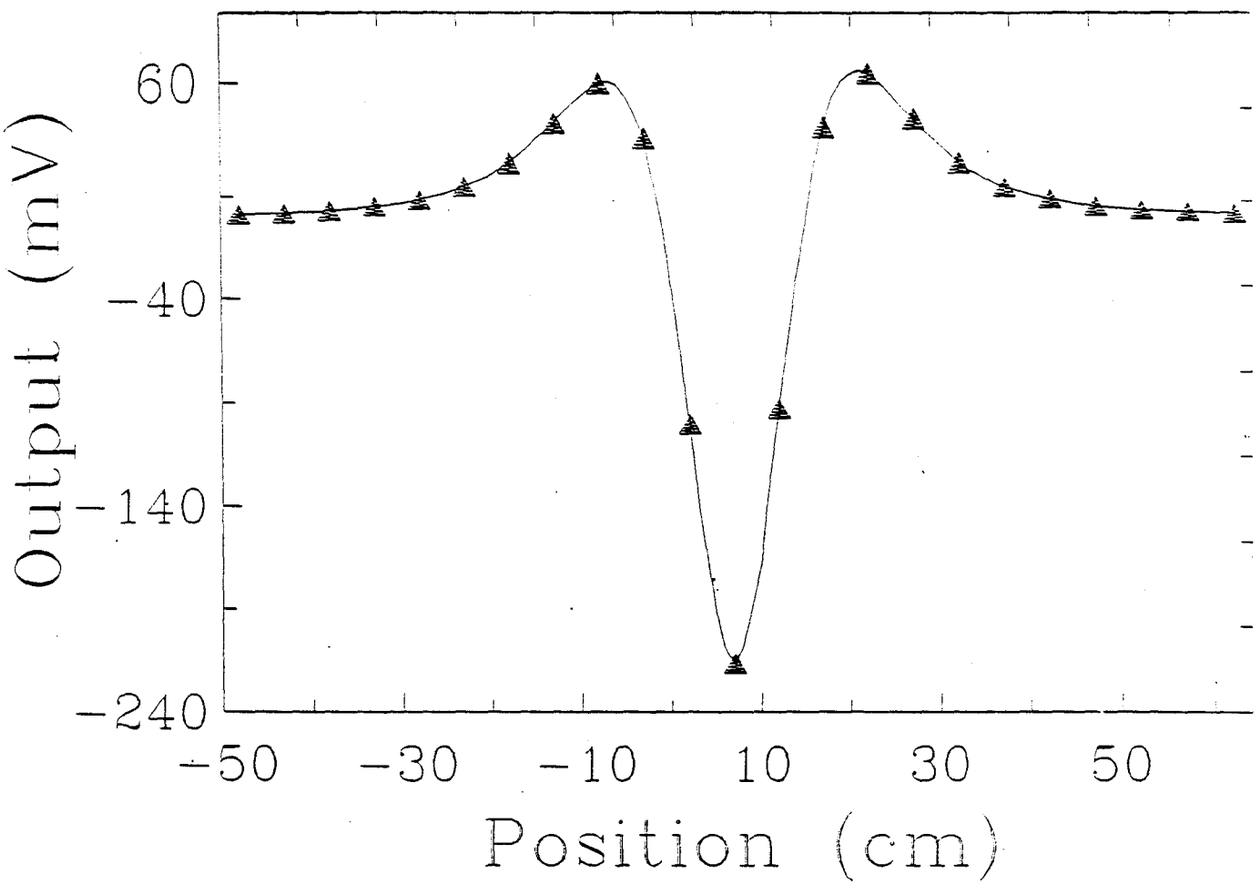

FIG. 3

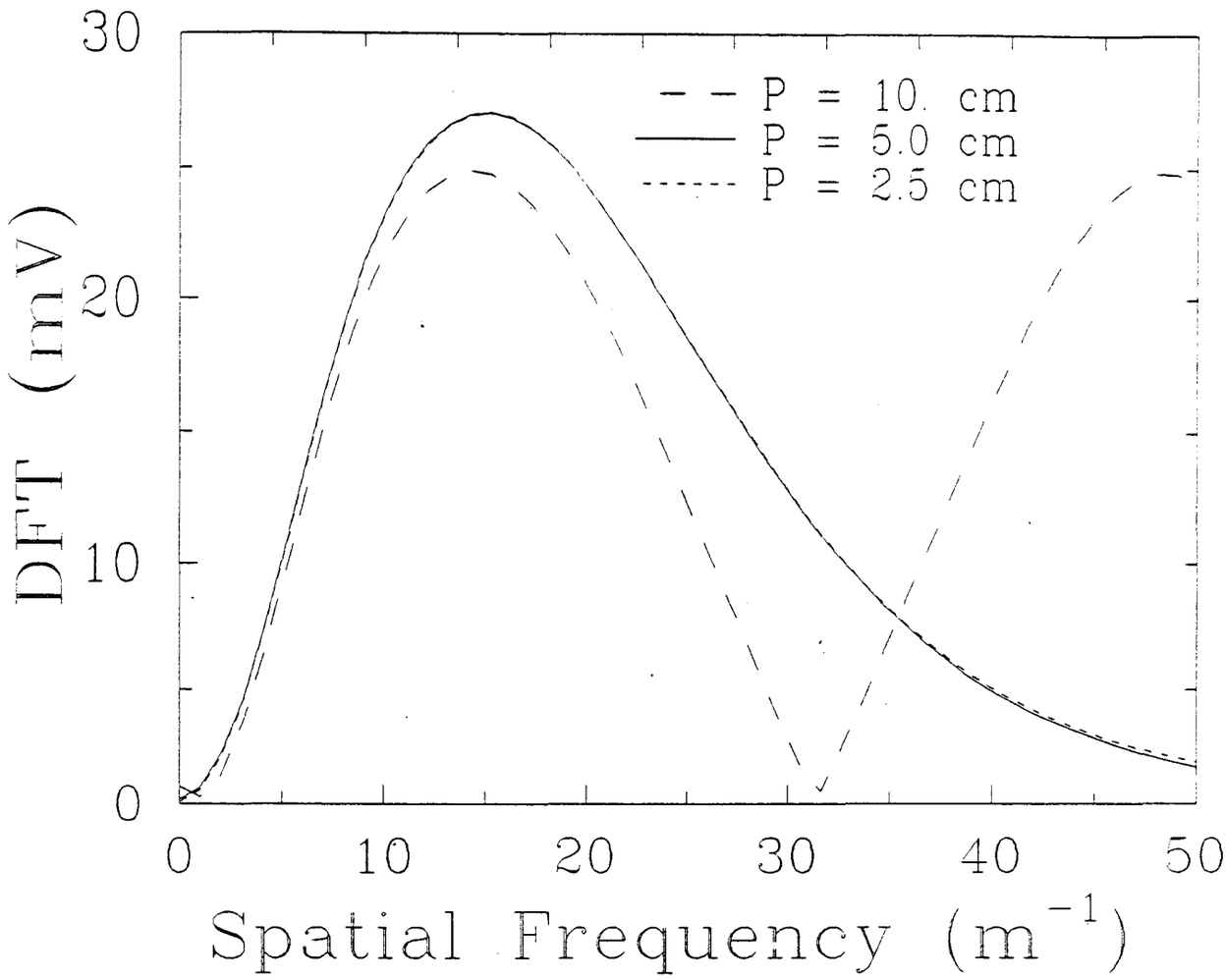
30
20
10
0
DFT (mV)
P = 10. cm
P = 5.0 cm
P = 2.5 cm
0
10
20
30
40
50
Spatial Frequency (m^{-1})

FIG. 4

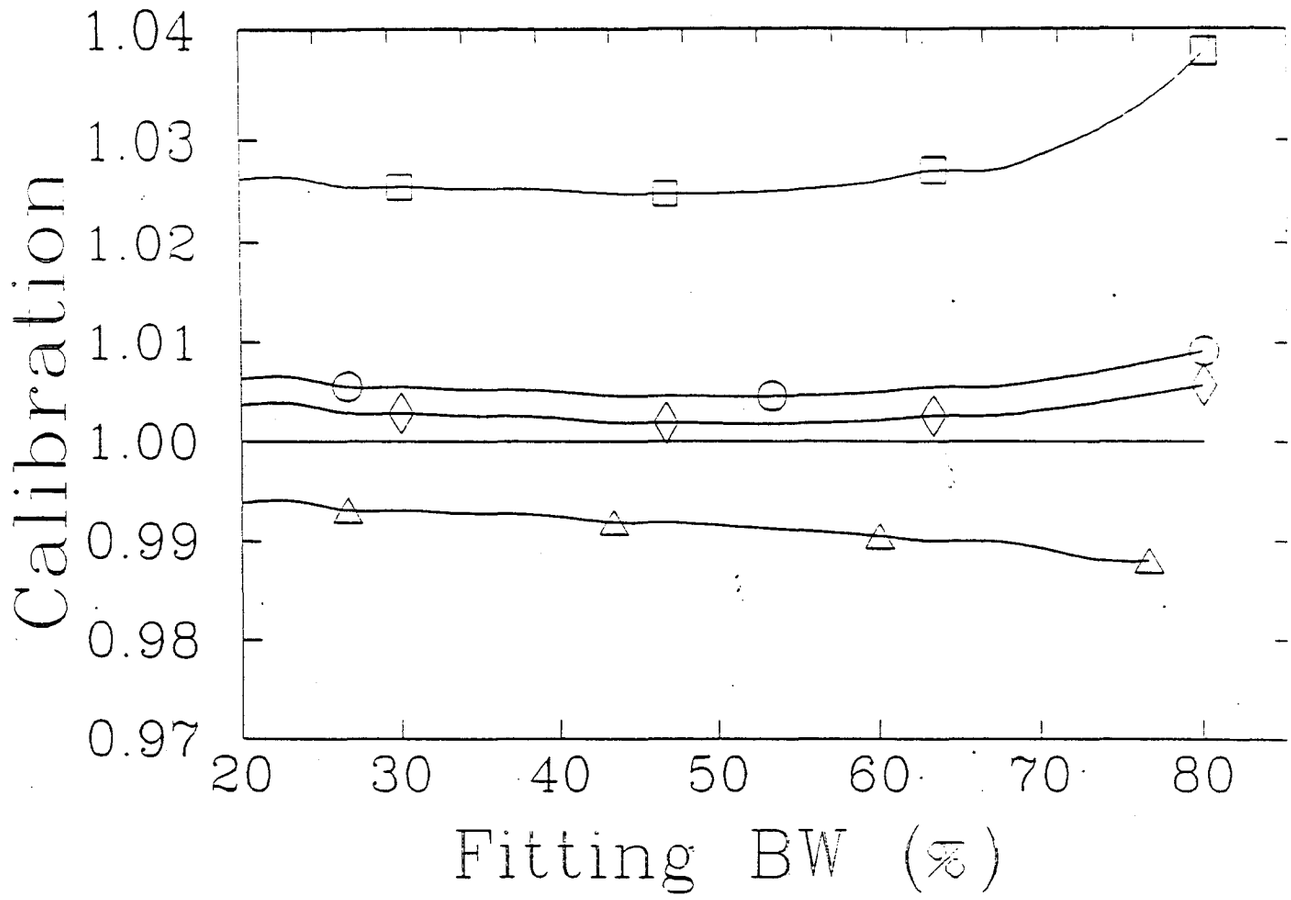
1.04
1.03
1.02
1.01
1.00
0.99
0.98
0.97
Calibration
20
30
40
50
60
70
80
Fitting BW (%)

FIG. 5

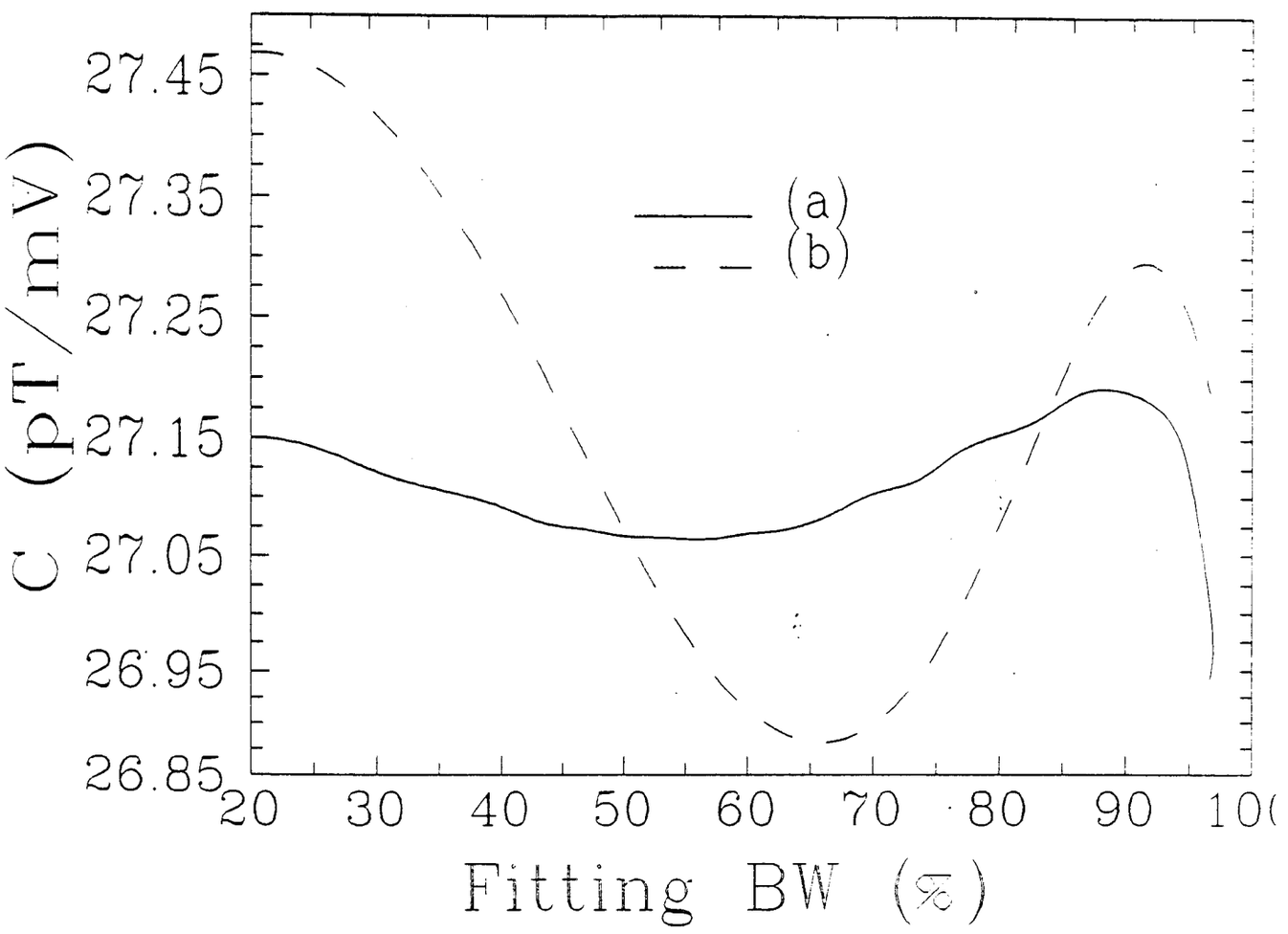
27.45
27.35
27.25
27.15
27.05
26.95
26.85
C (pT/mV)
(a)
(b)
20
30
40
50
60
70
80
90
100
Fitting BW (%)

FIG. 6

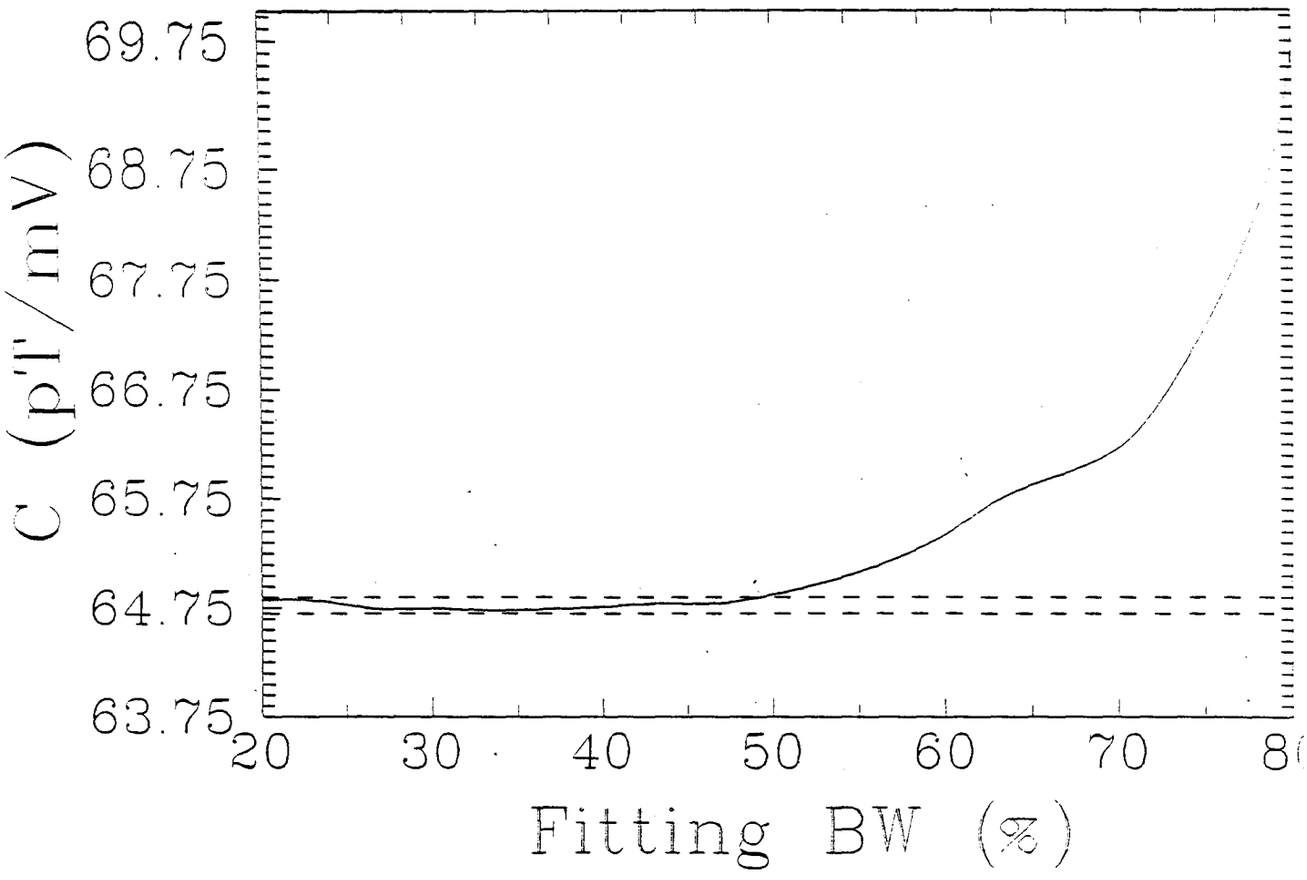

FIG. 7

SERVIÇO DE BIBLIOTECA E INFORMAÇÃO - IFQSC
FÍSICA

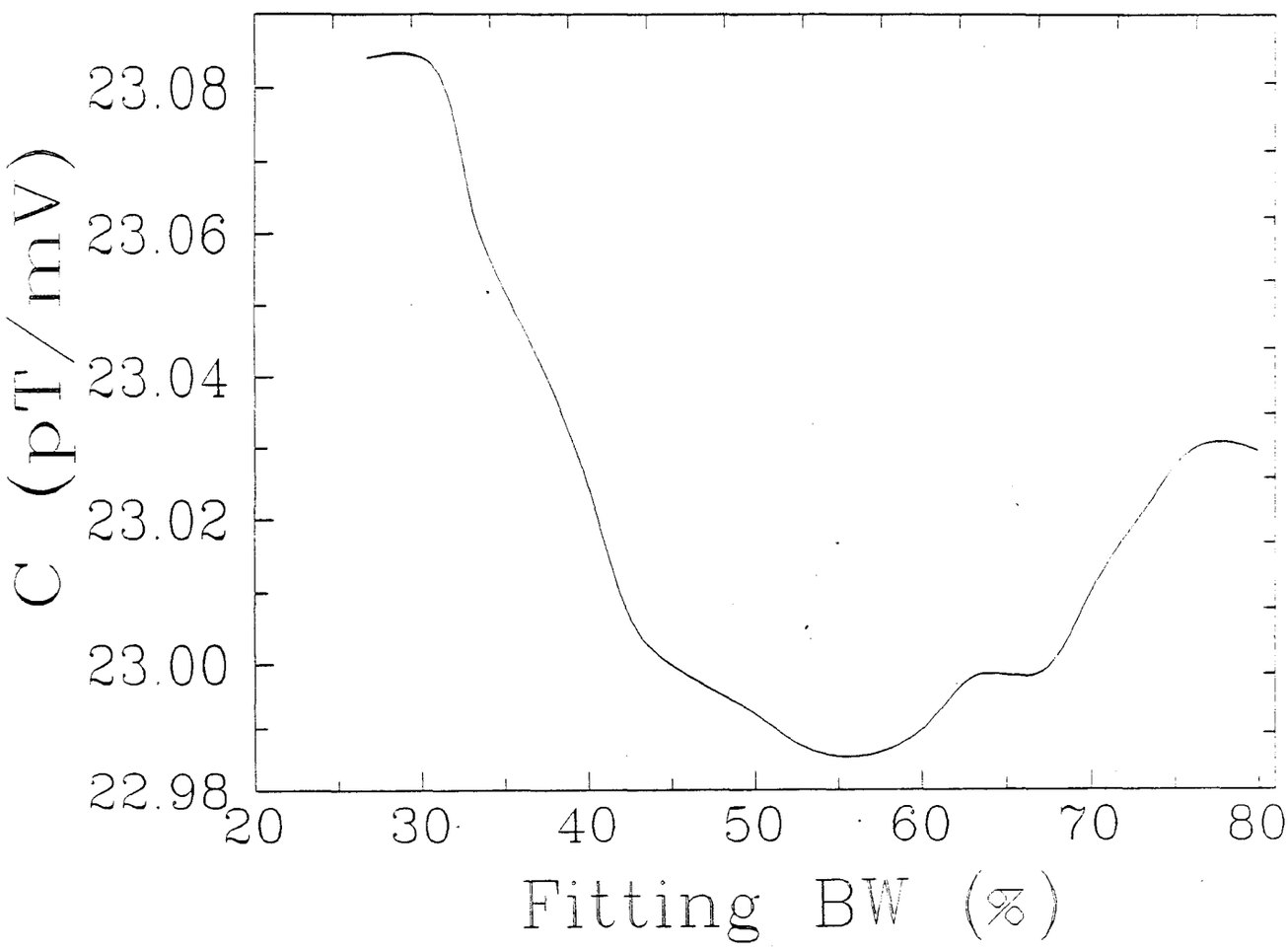
23.08
23.06
23.04
23.02
23.00
22.98
C (pT/mV)
20
30
40
50
60
70
80
Fitting BW (%)

FIG. 8

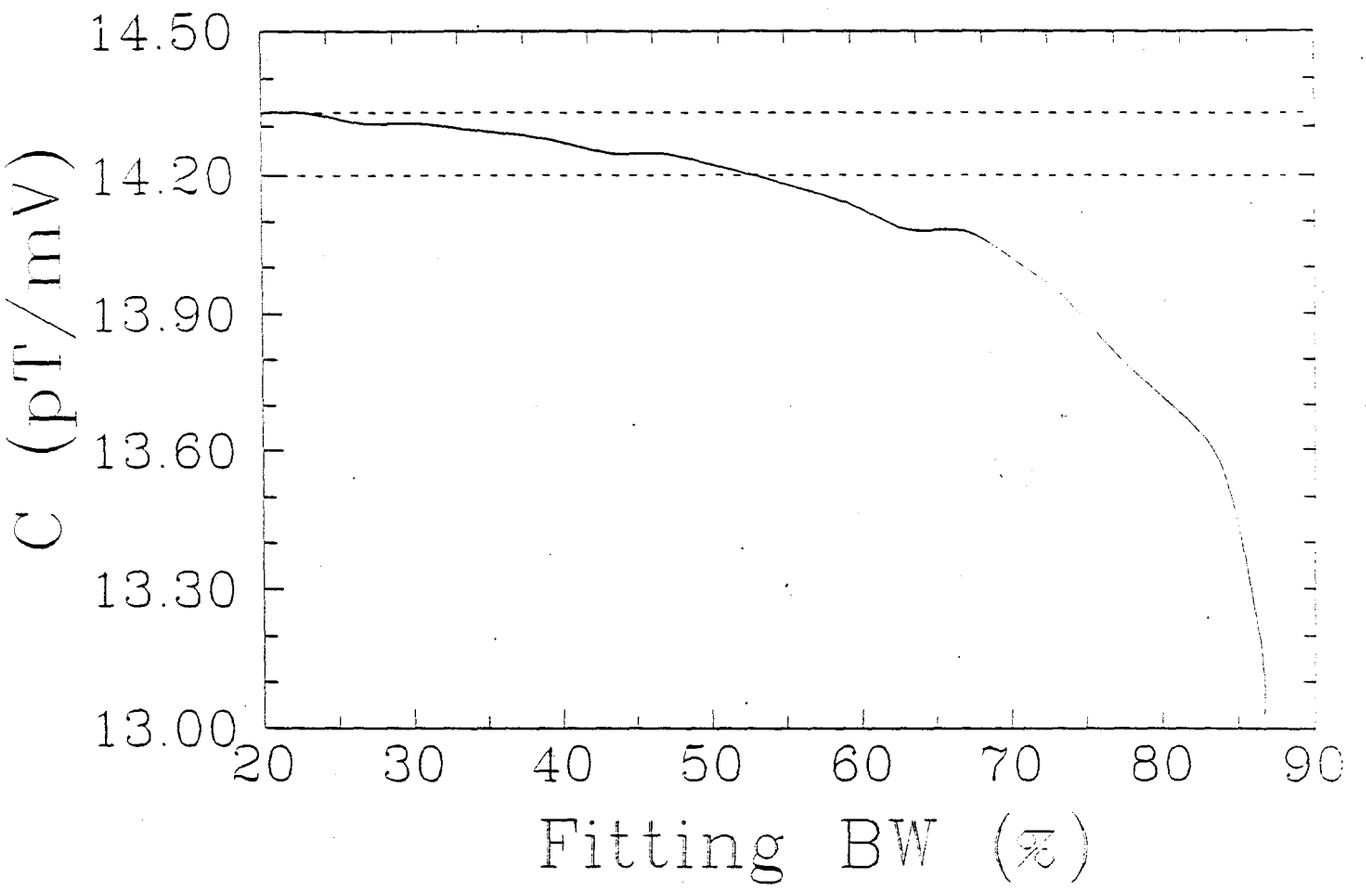
14.50
14.20
13.90
13.60
13.30
13.00
C (pT/mV)
20
30
40
50
60
70
80
90
Fitting BW (Hz)

FIG. 9

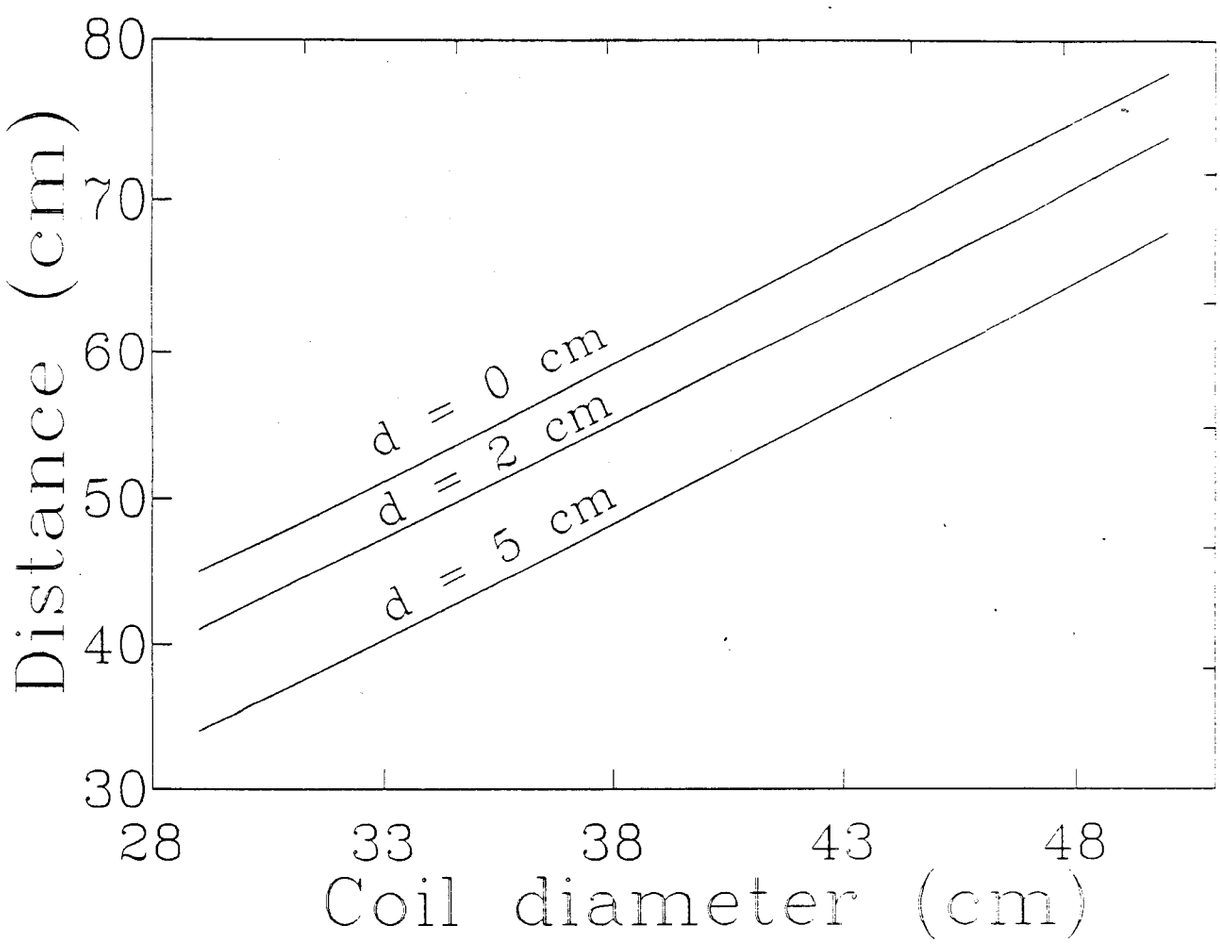
80
70
60
50
40
30
Distance (cm)
d = 0 cm
d = 2 cm
d = 5 cm
28
33
38
43
48
Coil diameter (cm)

FIG. 10